1 2 9 0

UNIVERSIDADE Đ
COIMBRA

Rute Rafaela de Almeida Vasconcelos

RESIDUAL STRESS MEASUREMENT IN FIBRE METAL LAMINATES (FML) USING THE INCREMENTAL HOLE-DRILLING TECHNIQUE

Dissertação no âmbito do Mestrado Integrado em Engenharia Mecânica, na área de Produção e Projeto orientada pelo Professor Doutor João Paulo da Silva Gil Nobre e apresentada ao Departamento de Engenharia Mecânica da Faculdade de Ciências e Tecnologia da Universidade de Coimbra

Dezembro de 2021

FACULDADE DE
CIÊNCIAS E TECNOLOGIA
UNIVERSIDADE DE
COIMBRA

Residual Stress Measurement in Fibre Metal Laminates (FML) using the Incremental Hole-Drilling Technique

Submitted in Partial Fulfilment of the Requirements for the Degree of Master in Mechanical Engineering in the Speciality of Production and Design

Determinação de Tensões Residuais em Compósitos Laminados Fibra-Metal (FML) pela Técnica do Furo Incremental

Author
Rute Rafaela de Almeida Vasconcelos
Advisor
João Paulo da Silva Gil Nobre

Jury

President	**Professor Doutor António Adriano Castanhola Batista** **Professor Auxiliar da Universidade de Coimbra**
Vowel	**Professor Doutor Ricardo Nuno Madeira Soares Branco** **Professor Auxiliar da Universidade de Coimbra**
Advisor	**Professor Doutor João Paulo da Silva Gil Nobre** **Professor Auxiliar da Universidade de Coimbra**

Coimbra, December, 2021

“Necessity is the mother of invention”

Plato

ACKNOWLEDGEMENTS

The work presented was only possible thanks to the collaboration and support of some people, to whom I must give my recognition:

To my advisor, Professor João Paulo Nobre, responsible for the initiative and guidance of this thesis, for his encouragement, patience, and total availability.

To my loved ones, my parents Ermelinda and Luís, my sisters Jéssica, Joana and Bruna and all my colleagues and friends, especially to Ana, Pedro, Carlos, Joana, João and Gabriel who helped me so much in these past years and made me the person I am today.

A special thanks to my friend Chelsy who always enhances the best side of me.

This work was supported by national funds through FCT – Fundação para a Ciência e a Tecnologia, I.P., within the projects UIDB/04564/2020 and UIDP/04564/2020.

COMPETE
PROGRAMA OPERACIONAL FACTORES DE COMPETITIVIDADE

QREN
QUADRO DE REFERÊNCIA ESTRATÉGICO NACIONAL
PORTUGAL 2007.2013

UNIÃO EUROPEIA
Fundo Europeu de Desenvolvimento Regional

FCT
Fundação para a Ciência e a Tecnologia
MINISTÉRIO DA CIÊNCIA, TECNOLOGIA E ENSINO SUPERIOR

Governo da República Portuguesa

Abstract

The aim of the present work is to broaden the scope of application of the Incremental Hole-Drilling (IHD) technique and to enable reliable residual stress measurements in anisotropic and layered materials, such as Fibre Metal Laminates (FMLs). The so-called integral method, according to the last developments in the field, was implemented with a numerical method for the resolution of the final system of linear equations using Python. The objective was to obtain non-uniform residual stresses in samples of a hybrid component made of micro-alloyed steel and Glass Fibre Reinforced Polymer (GFRP/Steel). For the IHD technique, relieved strains, caused by relaxed residual stresses during the incremental drilling process, and the necessary calibration coefficients, that relate these two variables, needed to be determined. Experimental IHD procedure was performed with the purpose of determining relieved strains in GFRP/Steel samples. Determination of calibration coefficients was done by numerical simulation using the Finite Element Method (FEM), through ANSYS software. Finally, a comparison of the results, obtained with other techniques and methods in the same samples, was performed for assessment and validation of the method studied in this thesis.

The results obtained allowed to conclude that the incremental hole-drilling technique can be used for measuring non-uniform residual stresses in FMLs. Despite some observed scattering in the residual stresses determined for deeper layers, the method used in this thesis allowed to determine the residual stress profile through the thickness of a GFRP/Steel sample, agreeing well with the results obtained by other techniques and methods, clearly identifying the singularities at the interfaces between cross-ply fibres and fibres-metal plies.

Keywords Residual Stress, Incremental Hole-Drilling Technique, Integral Method, Fibre Metal Laminate, Anisotropic Material, Finite Element Method

Resumo

O presente trabalho teve como objetivo ampliar a área de aplicação da técnica do furo incremental (TFI) e permitir uma determinação fiável de tensões residuais em laminados de fibra-metal (anisotrópicos e em camadas). O denominado método integral, de acordo com os últimos desenvolvimentos na área, foi implementado com um método numérico para a resolução do sistema final de equações lineares em Python. O objetivo era obter tensões residuais não uniformes em amostras de um componente híbrido feito de metal e polímero reforçado com fibra de vidro (PRFV/Aço). Para a TFI, deformações aliviadas, causadas pelas tensões residuais relaxadas durante o processo de furação, e os coeficientes de calibração necessários, que relacionam essas duas variáveis, precisam de ser determinados. O procedimento experimental da TFI foi realizado com o objetivo de determinar deformações aliviadas em amostras de PRFV/Aço. A determinação dos coeficientes de calibração foi feita por simulação numérica utilizando o método dos elementos finitos através do software ANSYS. Por fim, foi realizada uma comparação dos resultados obtidos com outras técnicas e métodos, nas mesmas amostras, para a avaliação e validação do método proposto nesta dissertação de mestrado.

Os resultados obtidos permitiram concluir que a técnica do furo incremental pode ser utilizada para a medição de tensões residuais não uniformes em laminados de fibra-metal. Apesar de alguma dispersividade observada nas tensões residuais determinadas para camadas profundas, o método utilizado nesta dissertação de mestrado permitiu determinar o perfil de tensões residuais ao longo da espessura de uma amostra de PRFV/Aço. Houve uma concordância com os resultados obtidos por outras técnicas e métodos, identificando claramente as singularidades nas interfaces entre as camadas de fibras orientadas e as camadas fibra-metal.

Palavras-chave: Tensão Residual, Técnica do Furo Incremental, Método Integral, Material Anisotrópico, Laminado de Fibra-Metal, Método dos Elementos Finitos

Contents

LIST OF FIGURES

LIST OF TABLES

LIST OF SIMBOLS AND ACRONYMS/ ABBREVIATIONS

List of Symbols

D – Diameter of the rosette

D_0 – Hole diameter

ε – Relieved strain

β – Clockwise angle from the x-axis (gauge 1) to the maximum principal stress direction

σ_{max} – Maximum (more tensile) principal stress

σ_{min} – Minimum (more compressive) principal stress

σ_x – Uniform normal x-stress

σ_y – Uniform normal y-stress

τ_{xy} – Uniform shear xy-stress

i – Number of hole depth increments so far

j – Sequence number for hole depth increments, $1 \leq j \leq i$

k – Strain record, $1 \leq k \leq 3$

l – Load case, $1 \leq l \leq 3$

p – Isotropic (equi-biaxial) strain

q – 45° shear strain

t – x-y shear strain

P – Isotropic (equi-biaxial) stress

Q – 45° shear stress

T – x-y shear stress

$\bar{a}_{ij}$ – Calibration constants

$\bar{b}_{ij}$ – Calibration constants

C_{ij}^{kl} – Calibration coefficients

θ – Angle between vectors UX and UR

U – Displacement

m – Index for strain gauge grid lines, $1 \leq m \leq n$

n – Number of strain gauge grid lines

E – Young's modulus

ν – Poisson's ratio

G – Shear modulus

Acronyms/Abbreviations

ARALL® – ARamid ALuminium Laminate

ASTM – American Society for Testing and Materials

BOAC – British Overseas Airways Corporation

CAFRALL® – CArbon and Flax fibre Reinforced ALuminium Laminate

CAKRALL® – CArbon and Kenaf fibre Reinforced ALuminium Laminate

CARALL® – CArbon Reinforced ALuminium Laminates

CFRP – Carbon Fibre Reinforced Polymers

CLT – Classical Laminate Theory

CTE – Coefficient of Thermal Expansion

DFG – German Research Foundation

FEM – Finite Element Method

FML – Fibre Metal Laminate

FEA – Finite Element Analysis

FOREL – National German Comprehensive Platform for Development of Lightweight System Solutions for the Electromobility

FRC – Fibre Reinforced Composite

FRP – Fibre Reinforced Polymer

GFRP – Glass Fibre Reinforced Polymer

GLARE® – Glass Laminate Aluminium Reinforced Epoxy

GTR – Grupo de Tensões Residuais

HBM – Hottinger Baldwin Messtechnik

IHD – Increment Hole-Drilling Technique

IM – Integral Method
ISF – Incremental Sheet Forming
LEIKA – Efficient Multi-Material Designs for Lightweight Bodies
MPISI – Materials Probe for Internal Strain Investigations
NECSA – South African Nuclear Energy Corporation
SPF – Shot Peening Forming
UD – Unidirectional
XRD – X-Ray Diffraction
PRFV – Polímero Reforçado com Fibra de Vidro
TFI – Técnica do Furo Incremental

1. INTRODUCTION

During the past decades, there has been an increasing demand for high strength-to-weight ratio materials, which have a great impact on the reduction of energy consumption. The main reason is to conciliate the accelerated technological evolution with a greener and more sustainable society. The technological evolution has been accompanied by the evolution of environmental awareness and so the need to take care of our world has become mandatory. As a consequence, emerges the need to find more resistant and lighter structures and materials of better quality. The necessary evolution in engineering materials led to the appearance of composite and lightweight materials, which arrived to help, not only qualitatively but also environmentally.

Hybrid composite materials, such as fibre metal laminates, make the automotive and aircraft transports lighter (around 25% weight reduction compared to a full-metal lightweight structure [1]), contributing to an efficient decrease of fuel consumption (less CO_2 into the atmosphere). The best example is the case of Glass-fibre Laminate Aluminium Reinforced Epoxy composite (GLARE®), which was selected for long parts of the fuselage of the Airbus A380 [2]. This type of materials has played an important role in history and will have an even more important role in the future. Therefore, it is essential to better understand and predict the actual behaviour of these hybrid composites.

During its production, FMLs are subjected to elevated temperatures, in particular those based in new thermoplastic matrices, compared to the thermoset ones. The difference in Coefficients of Thermal Expansion (CTE) of the different materials leads to the origin of tensile residual stresses upon cooling. The hybrid materials can be compromised due to the existence of these residual stresses, so it is essential to better understand their mechanical behaviour, by predicting how those stresses arise and determining their distribution through-thickness. Studies concerning the residual stresses in FML materials are limited and this issue still needs further attention and understanding.

1.1. Motivation

The experimental determination of residual stresses in composite laminates is difficult and complex. FML materials (anisotropic and layered) are composed of alternatively distributed layers of amorphous and crystalline structures. To determine residual stresses, diffraction techniques cannot be used, as they are only useful for crystalline materials or have highly restricted application for hybrid composites. One possible method might be the incremental hole-drilling (IHD) technique. This widely accepted semi-destructive technique is characterised by its relatively lower cost, its fastness in determining residual stress profiles and its independence from the material's microstructure, managing to provide reliable and useful information about the residual stresses near the surface of the material. Nonetheless, standard procedures related to this technique (e.g., ASTM E 837) are only valid for isotropic materials with linear elastic behaviour, therefore not applicable to the case of FMLs. While in this technique, for isotropic materials, the necessary calibration coefficients are almost material's independent, for anisotropic and layered materials there is a visible dependency on the material properties and stacking ply strategy. Due to this, valid calibration coefficients can only be determined by numerical simulation, case by case. The greatest motivation for this work is associated with the aim to develop and validate calculation methods for solving the problem to determine residual stresses in FMLs by IHD technique, cooperating under the scope of a German research project (DFG), leading by Kassel University and involving the University of the Witwatersrand (Wits - South Africa) and the University of Coimbra (GTR/CFisUC).

1.2. Main Objectives

The main objective of this work is to contribute to the development of the IHD technique, for its reliable application to FML materials. To accomplish this task, the following aims must be achieved:

- Develop the integral method, valid for isotropic materials (ASTM E 837), for its application to hybrid fibre metal composite laminates (anisotropic and layered in nature);
- Experimentally, to perform IHD tests in GFRP/Steel samples, to determine strain relaxation curves as a function of the hole depth;

- Numerically, to determine the calibration coefficients, by the finite element method (FEM), which are necessary for the determination of residual stresses using the so-called integral method;
- Computationally, contribute with a software developed in Python, complementing the one that already exists for isotropic materials at GTR/CfisUC. The software should be able to numerically solve the system of linear equations resulting from the application of the integral method;
- Validate the obtained results by comparison with results obtained by other techniques and methods (e.g., neutron diffraction).

1.3. Dissertation Structure

This document is divided into 7 chapters. Yet, 3 major parts can be clearly identified. In the initial part, an introduction and an overview of the state of the art in this field are made (chapter 1 and 2). Subsequently, the numerical and experimental part of this work is presented (chapter 3, 4 and 5). Finally, the results, discussion and conclusions are reported, as well as the recommendations for future work (chapter 6 and 7). The topics addressed in each chapter are as follows:

Chapter 2: Literature review

This chapter introduces scientific concepts about manufacturing of fibre metal hybrid composite materials and a brief approach of the origin, importance and determination of residual stresses in FMLs. The incremental hole-drilling technique is presented, as well as its principles and the residual stress calculation methods, differentiating it for isotropic and anisotropic materials.

Chapter 3: Method for calculating residual stresses in FMLs and software development

The chapter starts by describing the method chosen to solve the residual stresses calculation problem. A description of the developed software is also provided, as well as the software itself.

Chapter 4: Materials and experimental procedure

It describes the material under study (GFRP/Steel), the specimens used and its fabrication. An experimental description of the application of the incremental hole-drilling technique is also carried out.

Chapter 5: Numerical simulation: determination of calibration coefficients

Numerical simulation created from ANSYS are presented, as well as the method for determining calibration coefficients.

Chapter 6: Experimental results and discussion

It presents the relieved strains curves and residual stresses curves as a function of the hole depth. Analysis of the obtained results and comparison with partner results by other methods is carried out.

Chapter 7: Conclusions and recommendation for future work

It presents the main conclusions of the work and recommendations for future research, for an optimization and development of the methodology used.

2. LITERATURE REVIEW

2.1. FML Materials

Fibre metal laminates (FML) are hybrid composite materials. They are an ideal combination of metals and composites resulting in a material that joins the best characteristics of both, without sharing their individual disadvantages. This allows the material to retain the qualities of simple metal structure and it presents considerable advantages in other aspects such as fatigue, corrosion and fire resistance, and weight reduction. These hybrid composites are versatile, high-performance materials with applications in the aerospace industry, where weight and space savings are essential. They are composed of thin (0.2-0.5 mm thick) metal layers alternating with fibre reinforced polymer matrix composite plies, such as Glass Fibre Reinforced Polymers (GFRP) or Carbon Fibre Reinforced Polymers (CFRP). There are several types of structural arrangements for them; from asymmetric to multi-stacking laminates, based on various performance requirements and manufacturing considerations. By alternating the stacking arrangement and the fibre orientations we can obtain different material characteristics, and so specialized performance features can be achieved [3,4]. FMLs are shown in Figure 2.1.

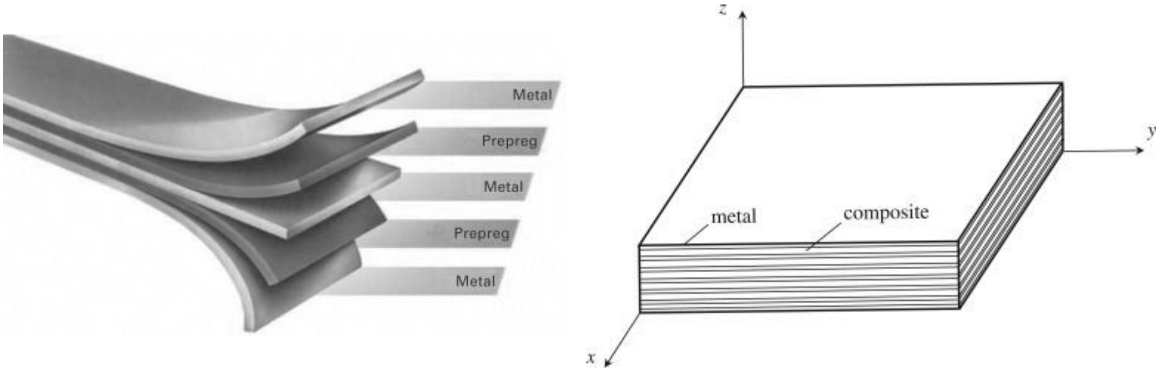

(a) (b)

Figure 2.1. Fibre Metal Laminates (a) and (b) [3,4].

Introducing a new material is a big investment in time and money. Much has to be learned about a large variety of properties; new production techniques have to be introduced and require concerted efforts of various disciplines, which turns out to be economically risky. The driving force behind hybrid composite developments was the need to reduce fatigue failure on airplanes with the incentive of reducing aircraft fuel consumption (through weight reduction) and maintenance costs [5].

2.1.1. Brief History of the Development of FMLs

In the 1950s, some tragic events caused by metal fatigue failure took place, thus compromising the use of metal in specific situations. One of the incidents that marked the history and changed the course of aviation occurred in 1954, when the BOAC Flight 781 (de Havilland DH.106 Comet, shown in Figure 2.3.a)) crashed after suffering a catastrophic decompression in mid-flight. The cause was fatigue fracture of the plane's roof. The fact that the windows were square at the time, with sharp corners, made the fuselage undergo considerably higher stresses than expected due to stress concentration effects. As a result, the incident changed the history of aviation where windows started to feature rounded corners (oval windows) [6]. Like this disaster many other happened, leading the aviation industry to improve and correct this so important impasse, the fatigue failure. Around that time, while composites were gaining notoriety, some weaknesses in them were observed, such as poor impact resistance and lower residual strength, weak plastic behaviour and inferior durable characteristics. Therefore, researchers have embarked on intensive investigation to find effective solutions [7].

In the end of the 70’s, due to costs (related to lack of investment capital) and in order to increase structural stability, Fokker, a NASA worker, embedded fibres into the adhesive between titanium layers. Surprisingly, the bonded structures offered a new advantage: better fatigue resistance. Fibres were shown to resist to crack initiation and further crack growth, thus improving the fatigue strength of the material [7,8]. In a multilayer material, the adhesive layers behave as crack dividers. If cracks start in only one of the sheets of the laminate, the sheets that are still uncracked reduce the crack growth rate in the cracked sheet, until a crack is initiated in the neighbouring sheet. Crack growth in thin sheet materials is slower than in plate material, because of the plane-stress effect. That is why FMLs have such a high fatigue resistance, especially against fatigue crack growth [5]. In Figure 2.2 it is shown the mechanism of fibre metal laminates to prevent crack propagation.

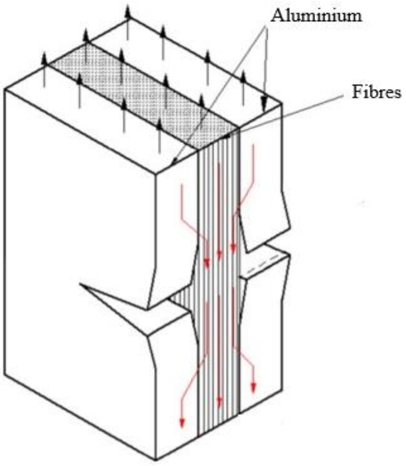

Figure 2.2. Schematic of fibre bridging mechanism to prevent crack propagation in FMLs. (adapted from article [9]).

In order to continue the research started by Fokker, the Delft University of Technology (TU Delft) in the Netherlands (1978) conceived an FML, consisting of aluminium sheets and aramid fibre reinforced epoxy (ARALL®), to increase fatigue performance of aluminium alloys. They were initially applied in the aviation industry, as wing panel materials on the Fokker F-27 and in cargo doors of the military transport C-17 Globemaster III in 1980s [1,7].

To avoid potential failure when using ARALL® as fuselage materials (to improve fatigue crack growth resistance), aramid fibres were replaced by glass fibres [10]. In the 1990s, GLARE® was developed at TU Delft and commercialized on the Airbus A380 (shown in Figure 2.3.b)) in fuselage and then in cargo doors at aircraft C-17. During this period, many investigations and developments were made regarding FML materials. Lin *et al*. [11] replaced the aramid fibres in ARALL® with carbon fibres, and developed CArbon Reinforced ALuminium Laminates (CARALL®). Then, NASA developed TiGr [12], which also belongs to the FMLs class. It consists of titanium layers interleafed with graphite fibre reinforced polymer. With the appearance of these FMLs, many more were created, using different metals, like steels and magnesium alloys.

(a) (b)

Figure 2.3. (a) The world's first commercial jet airliner, de Havilland DH.106 Comet [13]; (b) the world's largest passenger airliner, A380 [14]. The figures present different scales.

Until then these hybrid materials were used to create simple components, as the techniques used (bending and lay-up techniques) did not allow it to be different. Since the 2000s, interest in expanding the industrial applications of FMLs to mechanical, construction, aerospace, automobile, biomedical and marine industries led to research for producing complex shaped FML components, using different techniques that increase complex geometry and enable a large production volume (forming, especially die forming techniques) [1].

Among the development of FML forming techniques, LEIKA – efficient multi-material designs for lightweight bodies, the first interdisciplinary research project launched by FOREL (a national German comprehensive platform for development of lightweight system solutions for the electromobility), was a particularly remarkable project partnering with several German industrial and academic research institutes. They bonded cover sheets of steel or magnesium to a core of carbon fibre reinforced plastic to create a sandwich laminate, presenting a lighter weight alternative to aluminium. Since lightweight engineering is critical to the development of new electric vehicles and for demonstrating the material's unique properties, LEIKA aimed to create a hybrid vehicle floor. The three-year project demonstrated the significant light-weighting opportunities presented by FMLs and their advanced manufacturing technologies in the automotive industry [1,15].

To summarise all the events that marked the discovery and evolution of such important materials, a review of these events is presented in Figure 2.4.

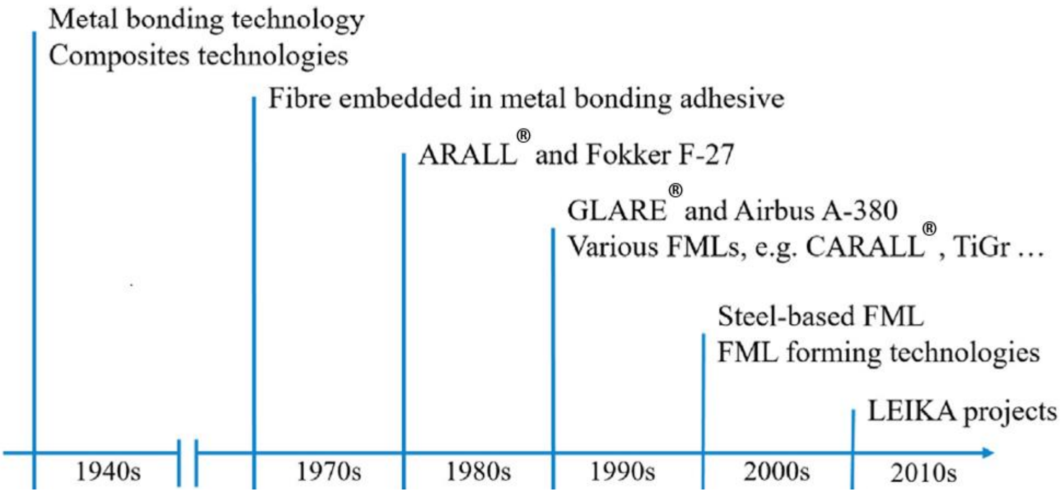

Figure 2.4. Development of fibre metal laminates (FMLs). (adapted from article [1]).

2.1.2. Range of Materials

The material selection to create FMLs, considerably affects their material properties and impact characteristics. Fibre reinforced composite (FRC) largely determine the stiffness and strength of FMLs, while metallic materials contribute for impact resistance, energy absorption and ductility [7]. Aluminium sheet is the most commonly used metallic material in FMLs attributable to its high impact resistance and superior ductility. Laminates with permanent bonding between aluminium and fibre composite are characterised by favourable strength and anti-corrosion parameters (excluding CARALL® laminates) and by resistance to impacts by means of concentrated force. On account to its low density, magnesium alloy is also used in FMLs [16].

FMLs applications in marine engineering were very restricted due to corrosion and hygrothermal (stress produced by humidity and temperature) effect. Fortunately, corrosion resistance of FMLs can be improved using titanium based. As laminates consisting of titanium and carbon fibres do not suffer from galvanic corrosion in operation conditions, it can be used in humid environments [7,16]. Titanium based FMLs, compared with aluminium based FMLs, have higher stiffness, high yield strength, fatigue and impact resistance at both room and elevated temperatures. Stainless steel based FMLs are also an alternative, due to the higher stiffness [7].

Regarding the fibre reinforced laminates, glass and carbon fibres are the most commonly used in FMLs. However, polypropylene fibres are a promising candidate against the impact loading.

In what fibres is concerned, several different composite recycling processes have been developed to cope with the rising accumulation of plastic waste. The innovation of adding natural fillers (e.g., natural fibres, cellulose nanocrystals, etc) in the polymers matrix to fabricate eco-friendly composites has improved material properties while minimising the problem regarding residue accumulation. This idea of hybrid composites with the combination of natural and synthetic fibres is still recent but there are already studies that conclude these composites can be very useful, as they exhibit important properties. More of this topic is presented in the article [17].

In a recent study, fibre metal laminates of aluminium alloy with a sandwich of synthetic and natural fibre were investigated for its fire flexible blankets and thermal insulation properties. It was verified that CArbon and Flax fibre Reinforced ALuminium Laminate (CAFRALL®) and CArbon and Kenaf fibre Reinforced ALuminium Laminate (CAKRALL®) are suitable to be used in fire-designated zones of an aircraft engine, as they can be candidates for future use in aerospace industry. More about this work can be found in article [18].

Among several reinforced laminates, thermoset epoxy resin is extensively used for bonding unidirectional prepregs. Thermoplastic resins (e.g.: Bispheno-A and polypropylene) are used in some FMLs due to their relatively short processing cycles [7]. In Figure 2.5, the most known FML materials are indicated, as well as their corresponding composition.

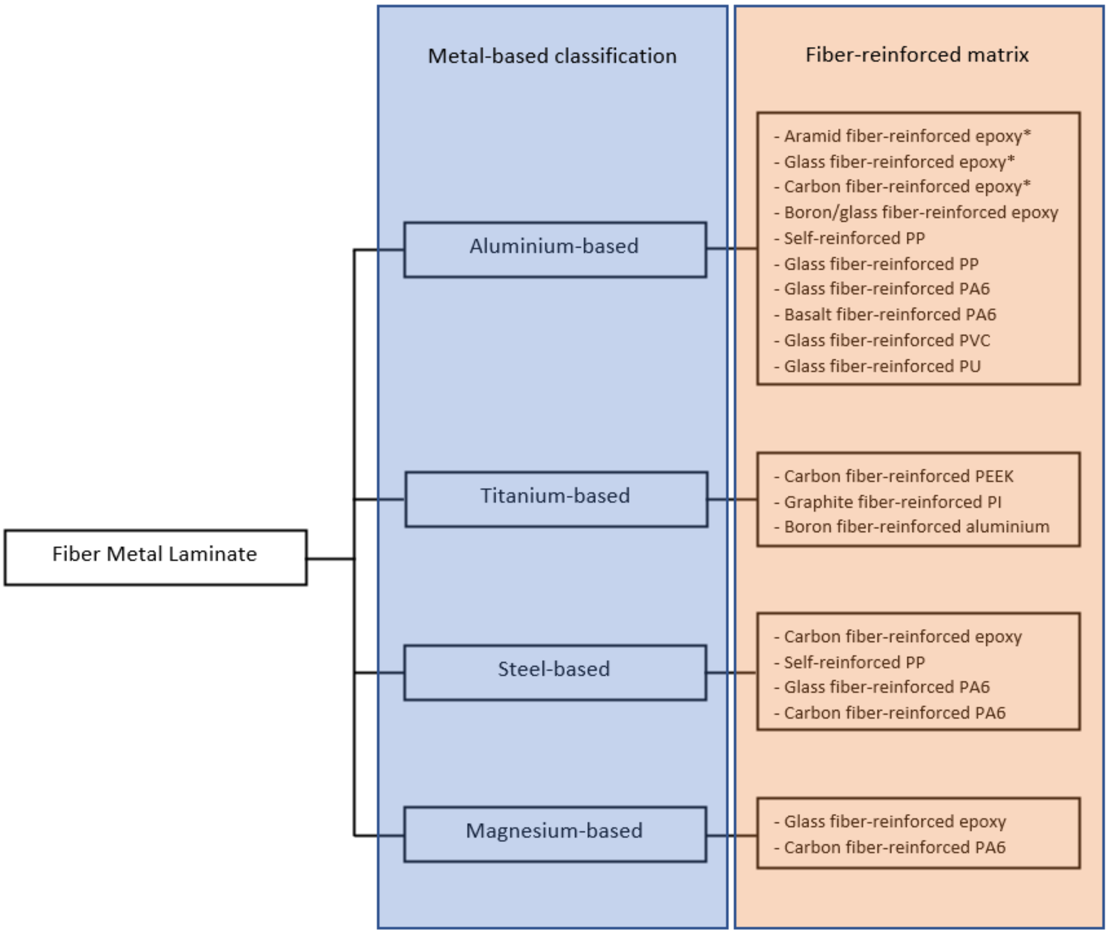

*Aluminium-based FMLs with aramid, glass and carbon fiber-reinforced epoxy are commonly known as ARALL®, GLARE® and CARALL®, respectively.

Figure 2.5. FMLs classification based on material constituents. (adapted from article [1]).

2.1.3. Manufacturing FMLs

Hybrid materials can be manufactured by forming metal and Fibre Reinforced Polymers (FRP) panels separately and then bonding them with adhesives. But, since this method requires a long cycle time and multiple tool sets, the manufacturing process bonding of the metal and the FRP before forming is more accurate. The most common process for fabricating FMLs, similar to the polymeric composite materials, is the use of autoclave technology. A few steps are needed for the correct manufacturing process of FMLs [7,19,20]:

- Treatment of metal to improve the adhesive bonding between metallic layer and fibre reinforced laminate.
- Preparation of materials with cutting, lay-up and debunking.

- Cure preparation - involves tool cleaning and part transferring (in some cases), and the vacuum bag preparation shown in Figure 2.6 (in all cases).
- Cure - incorporates the flow-consolidation process, chemical curing reactions, and bonding between fibre and metal layers.
- Post-treatment - After hot-curing cycle in an autoclaving process, the residual stress in FMLs is inevitable due to the different thermal expansion of metal and FRP layers. It can lead to certain tensile stresses in metal sheets and compression stresses in fibre laminates. Residual stress could have a negative effect on the fatigue resistance of FMLs, and so the material's fatigue performance could be decreased. This condition can be improved by post-stretching, thus reversing the effect of residual stress (reduce or eliminate residual stress).

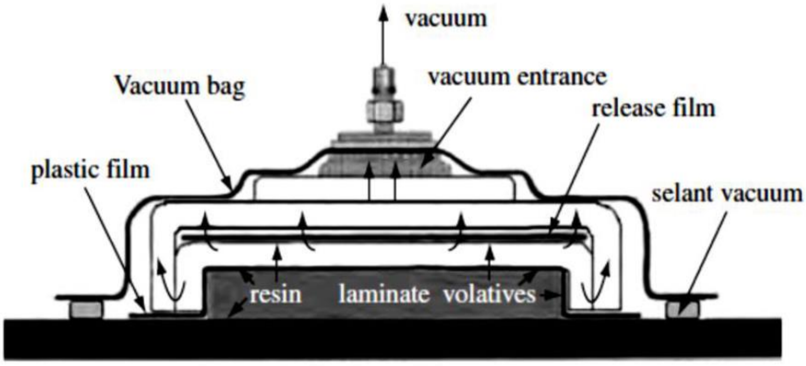

Figure 2.6. Schematic representation of vacuum bag system [19].

2.1.4. Forming Techniques for FMLs

Composite layers have a very limited formability. Metal alloys can be deformed plastically but they also exhibit some elastic deformation. The deformation of fibres is pure elastic, so after deforming, the fibres cause spring back. During the deformation process to create different shapes of elements, most of the applied work in FMLs is elastic, which leads to spring back, residual stresses, or both [8]. Due to these characteristics, the need of high technology for its production, as well as manufacturing costs, FMLs did not move sooner to other industries. When realised FMLs would be an indispensable material, possible to be applied in various industries, showing the best properties, production research has been done in order to decrease cost production while increasing production.

The lay-up and press brake bending forming techniques were used initially, when more advanced techniques were not yet known. Today, they are still used, but less often. The lay-up technique can be used for large components like fuselage and wing panels. This technique shown in Figure 2.7.a), is a similar technique used in manufacturing FRP components. With a designated sequence, each layer is stacked onto a mould and since it is a large area-to-thickness ratio, the material deforms into the mould without significant forming force. The panel is then vacuum bagged and sent to an autoclave for curing. The applicable geometries of this technique are significantly restricted, only managing to form a simple curve [1]. The next technique, press brake bending, also applied in metal working process, is used to produce single curvature FML components. However, the design of such components is limited by the low failure strain of the embedded fibres. Thin FMLs with unidirectional (UD) reinforcement can be bent easily when the bending line is parallel to the direction of the embedded fibres. Bending thicker FMLs will increase the risk of delamination due to the increased interlaminar shear stress [1].

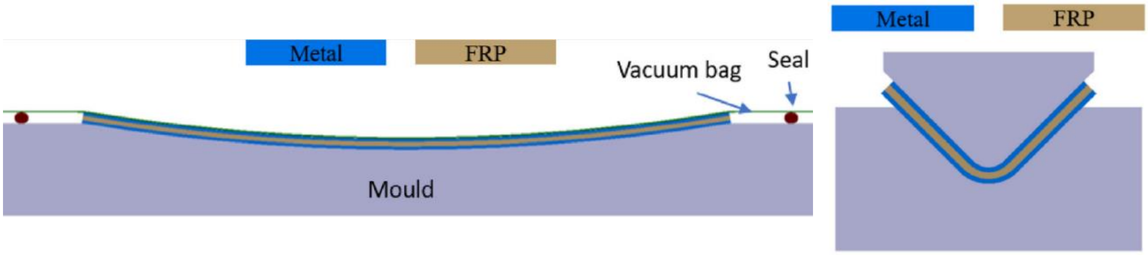

(a) (b)

Figure 2.7. Schematic illustration of lay-up (a) and press brake bending (b) techniques [1].

More recent forming technologies for FML components are shot peening forming (SPF), incremental sheet forming (ISF) and die forming methods. There are some variants of die forming like stamping, hydroforming and electro-magnetic forming – see Figure 2.8. In die forming, material blanks are pressed against a die mould and shaped under the deforming force introduced [1]. The most widely used die forming method is stamping. It is a well-developed mass production technology for forming sheet metal components. It has also drawn extensive interests in producing FRP components and has recently been used to form FMLs. In stamping method, the tool sets typically comprise a set of matched dies, and a blank holder. Tool sets are usually heated [1].

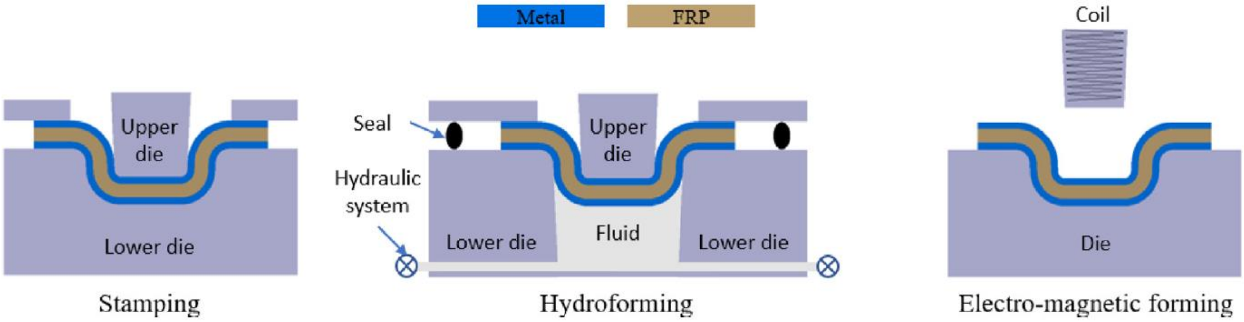

Figure 2.8. Variants of die forming methods [1].

According to article [1], alternative forming technologies, such as SPF, ISF and laser forming, are feasible but limited. Limitations in formability and/or productivity make them not the best candidates for the high-volume production of complex-shaped FML components. On the other hand, stamp forming has shown progress for producing more complex-shaped FML components, such as deep drown panels. Table 2.1 presents a comparison of several important forming methods; comparing the ability to create complex forms, the radius size that can be realised in each of the techniques, as well as their cycle time and production volume.

Table 2.1. Comparison of different FML forming technologies. (adapted from article [1]).

	Shape	**Radii**	**Cycle time**	**Production volume**
Bending (Press brake)	Single curvature	Small	Short	Large
Lay-up	Single, shallow double curvature	Large	Long	Medium
Laser forming	Single curvature	Large	Long	Small
Shot peening forming (SPF)	Single, shallow double curvature	Large	Long	Medium
Incremental sheet forming (ISF)	Complex double curvature	Small	Long	Small
Die forming/Stamping	Complex double curvature	Small	Medium	Large

2.1.5. Residual Stresses in FMLs: Origin, Importance and Determination

Residual stresses are static multiaxial stresses, existing in an isolated system without any external force or moment being exerted on it. These stresses are found in mechanical equilibrium within the material. The combination of residual and applied stress can affect structural integrity and safety [21].

The residual stress could either enhance the material properties or be detrimental to its service life, depending on its state. Usually, residual stresses should be minimised as they can cause different detrimental effects (if we are dealing with tensile residual stresses), thus, reducing the lifetime of the components, e.g., in case of fatigue loading. But sometimes, deliberately introducing compressive residual stresses might be beneficial, e.g., by shot peening or deep rolling at the surface of metallic components. In some cases, they can improve component's mechanical behaviour, enhancing its fatigue life (e.g., in polycarbonate samples by quenching), generally increasing the lifetime of products [22].

FML materials are well known for their excellent characteristics, such as high tensile strength, low density, excellent fatigue properties and impact damage resistance. However, they have a major disadvantage that can compromise the excellent properties they present. The existence of tensile residual stresses has a very negative effect on the durability of hybrid components, which can decrease their lifetime. After processing these hybrid components at elevated temperatures, the difference in the CTE between the metal and the composite leads to the appearance of residual stresses during cooling [23]. The residual stresses created can have a decisive effect on the mechanical properties of hybrid components and can cause defects as well as delamination, part failure due to geometric distortion, built-in cracking or premature failure of parts subjected to alternating loading or corrosive environments [24]. So, it is very important to identify the residual stresses to evaluate different combinations of FML materials and to accelerate the development of promising material FML systems [23].

Although a great development in this area has been carried out in the last decades, regarding the determination of residual stresses in metallic materials, studies concerning the residual stresses in FML materials are limited and this issue still needs further attention and understanding. There are many well-known and effective methods capable of determining residual stresses, which are divided into three main groups: destructive, semi-destructive and non-destructive methods. Examples of non-destructive methods, also called physical methods, are: diffraction method, ultrasonic method, magnetic method, etc. Unfortunately, these techniques have some barriers that unable their use in hybrid composites, as they are only useful for crystalline materials or have highly restricted application. A diffraction method, such as X-Ray Diffraction (XRD), is based on measuring the strains of the crystal lattice through variations in the interplanar distance of the crystalline material. Hence, it is not possible to be used in non-crystalline materials. Furthermore, XRD technique is a method limited to sample surface characterisation (up to $\approx 20\,\mu m$ depth, depending on the material under testing), therefore it cannot be used for layered materials as it would not reach all the layers [25,26]. Another diffraction method, neutron diffraction, is based on the same principles as the prior technique, but instead of using X-rays, it uses a neutron beam. Comparatively, this technique allows a complete description of complex stress states and analyses samples to greater depths (up to $\approx 150\,mm$, depending on the material) due to the penetrating nature of neutrons. However, the necessary neutron beams are only available in facilities that have nuclear reactors, which reduces their availability and substantially increases their cost [25,27].

Regarding semi-destructive methods, the Incremental Hole-Drilling (IHD) technique is one of the most common residual stress measuring method [28]. This technique is considered semi-destructive as it involves the removal of a small portion of the sample material, which can be repaired later in case of large components. In this mechanical technique, a small hole is drilled into increments along depth. The residual stress determination is made from the measured relieved strain values and numerically determined calibration coefficients. A more exhaustive approach to this technique is made in the next section (2.2). There is already a standard test method for determining residual stresses by the IHD technique in isotropic materials with linear elastic behaviour, such as the procedure proposed by the American standard ASTM E 837-20 [28]. This was possible due to the almost independence of the necessary calibration coefficients from the material properties. It was shown that these coefficients depend on the geometry only. Due to recent developments, the use of this technique in FML materials is feasible, but, unfortunately, a standard test method for anisotropic and layered materials (FML) seems to be impossible to achieve, due to dependency of the calibration coefficients from the material properties and stacking ply strategy. This is in the scope of the present work.

2.2. Incremental Hole-Drilling Technique (IHD)

The Hole-Drilling (Strain-Gauge) Method is one of the most cost-efficient and simple methods to evaluate the residual stresses present in industrial workpieces. This mechanical technique is relatively simple, inexpensive, fast, versatile, well known and with a long history of application to isotropic materials with a linear elastic behaviour [29]. It consists in making a small hole at material's surface, in successive depth increments (drilling the hole in a series of steps) and measuring the relaxed strains on the surface at the end of each drilled increment, using most commonly, electrical strain gauges (see Figure 2.9.a)) – usually a ASTM standard three-element strain gauge rosette (type A, B or C) is used (see Figure 2.9.b)) [28]. The technique is based on relating the measured strain relaxation at surface with the residual stress existing at a given depth increment, along the total depth of the hole. This method allows to evaluate the residual stresses not only along the layers but also between layers. There are several calculation procedures that can be used, all of them requiring valid calibration procedures [30].

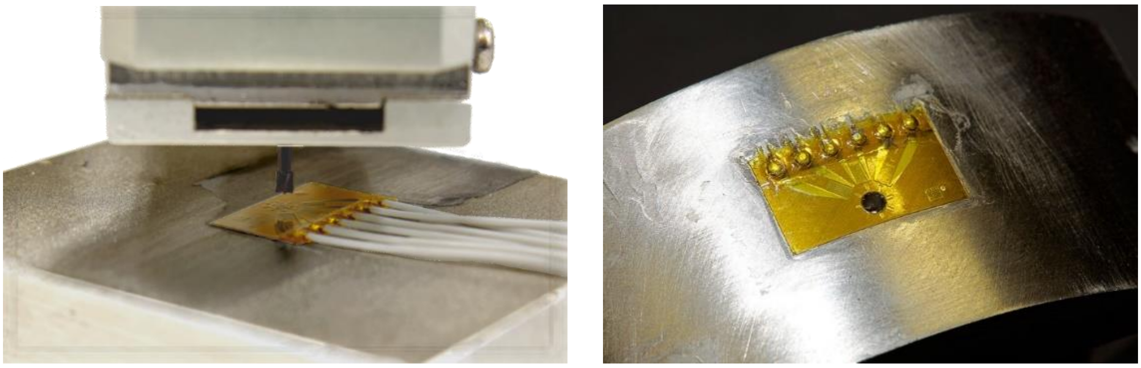
(a) (b)

Figure 2.9. (a) Head of IHD machine: end mill, strain gauge rosette, connection wires to the data acquisition system (a three wire connection in a 1/4 Wheatstone bridge configuration is commonly used); (b) three-element strain gauge rosette (ASTM type B) [31].

The equipment used in this study for performing IHD procedure is presented in Figure 2.10. Shortly summarising, the measurement procedure with the IHD method is done following the steps shown in Figure 2.11. It should be emphasised that the incremental hole-drilling method is not just about making a hole in a series of small steps, this method incorporates the entire process required for the calculation of residual stresses.

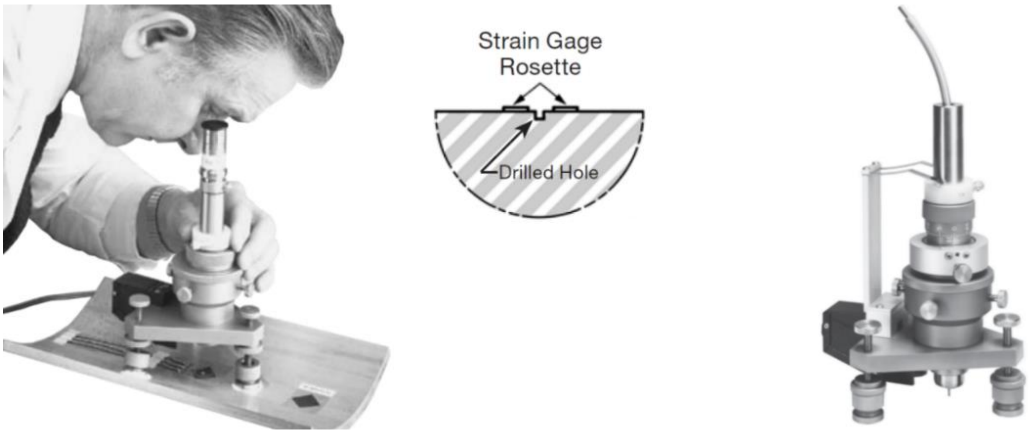

(a) (b)

Figure 2.10. (a), (b) Vishay RS 200 Milling Guide - a typical hole-drilling apparatus (an optical device for centring the tool holder and a hole-drilling tool, respectively) [32,33].

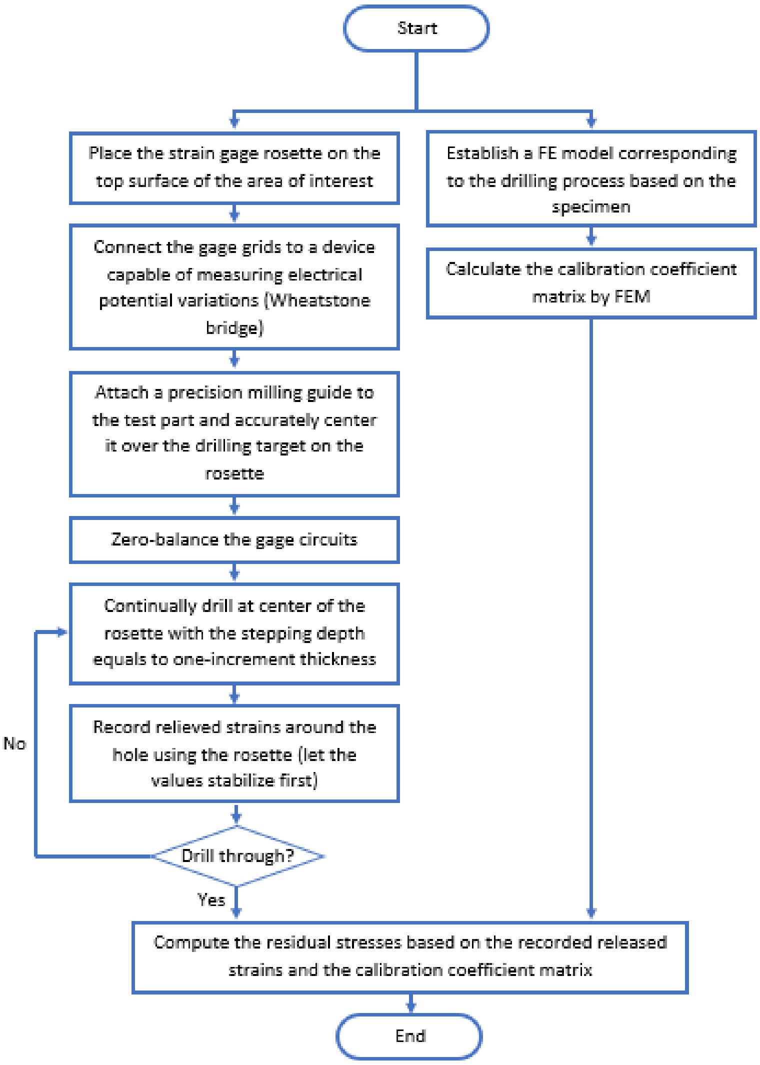

Figure 2.11. IHD method process flowchart. (adapted from article [34]).

As we can observe in the Figure 2.11, on the left side is shown the process of calculating the relieved strains, caused by the drilled hole. On the right side, the process of calculating the calibration coefficients by using the Finite Element Method (FEM) is presented. The calibration coefficients are necessary since it is required to relate the residual stress existing in a given depth increment with the relieved strains measured at surface. So, the two distinct procedures are needed to calculate the residual stresses existing in the material to be tested. However, in some specific cases (isotropic materials) the coefficients determination process is not necessary, as there are already tabulated values for calibration coefficients (previously calculated using the FEM) in materials that fulfilled all conditions announced by the ASTM E837, since, as previous referred, these coefficients are almost material independent and depend only on the geometry (hole diameter and depth, incremental size, and strain gauge geometry). Composite laminates (anisotropic and layered materials), which are out of the scope of the ASTM standard, need the coefficients determination phase since there is a clear dependency on the material properties.

Some of the limitations of the hole technique are the potentially errors and uncertainties due to inaccuracies committed during drilling (e.g.: cutter bias, hole eccentricity, surface roughness, poor sample surface preparation, etc). Besides, residual stress determination by IHD is very sensitive to measurement errors, due to error propagation in the inverse problem involved. In an in-depth analysis of all types of errors [35], it is shown that the margin of error increases with depth. The relieved strains are mostly influenced by the near-surface residual stresses. Interior stresses have influences that diminish with their depth from the surface. Since the strains, related with the residual stresses existing at each depth increment, are measured at material’s surface, the sensitivity of the method decreases with the hole depth and, therefore, there is a limit depth from which is not possible to measure the strain relaxation, i.e., the curves of strain relaxation curves present an asymptotic behaviour. Thus, the depth of the hole is limited to approximately 0.4 times the nominal radius of the rosette $(Z \leq 0.4 \cdot D)$ (D is the diameter of the rosette); more or less equal to the hole diameter [32]. Another limitation is the plasticity effect that occurs whenever the residual stress state induces localised plastic deformations. This happens due to the stress concentration around the hole. If the local stress concentration exceeds the yield stress of the material, the strain field around the hole is modified. Since the theory for calculating the residual stresses for this technique is based on a purely elastic situation, as it happens with the finite element calculation of the calibration coefficients, an overestimation of the residual stresses installed in the material in this situation would be observed (the actual values are usually smaller than indicated). Therefore, the domain of application of the standard for the IHD method is in isotropic materials with linear elastic behaviour whose residual stresses do not exceed 60% of the material's yield stress, according to Nobre *et al*. (2020) [36]. The ASTM E837 indicates 80% [28].

The ASTM E837 standard [28] is an internationally accepted reference for the hole-drilling strain-gauge method, which defines the scope, measurement range, minimum requirements of instrumentation, test procedure, and algorithms and coefficients for the computation of uniform and non-uniform stress distribution, but only for isotropic and linear elastic materials. For isotropic materials the values for calibration coefficients are already tabulated, this because calibration coefficients are almost material independent, and so it is considered that the values do not vary from material to material. They just depend on hole geometry (depth and diameter), strain gauge type and position. In the case of anisotropic and layered materials there is also a dependence on the material properties, where the type of material used is relevant. On the other hand, the general equation which governs the strain distribution around the hole, based on the Kirsch's solution, does not present a trigonometric form, as it happens for the case of isotropic materials [37]. For this particular situation it is necessary to find new calculation procedures.

2.2.1. Brief History of the IHD Technique

There is already a lot of published literature and consolidated information about the hole-drilling method. A description of the most important events that marked the history of this method are presented, by points in history [38,39]:

- The discovery of this technique was made by Mathar in 1934, he used mechanical strain gauges to measure displacements around holes that were made in tensioned plates [40].
- In 1950, the mechanical strain gauges were replaced by electric strain gauges, thus improving the measurement accuracy of the method. This step was taken by two professors from Ghent University in Belgium, Soete and Vancrombrugge [41].

- In 1951, a new method was proposed, similar to the hole-drilling method, the ring drilling method. It was introduced by Milbradt and then improved by Gunnert in 1958 [42,43].
- In 1956, Kelsey published the first investigation into residual stress variation with depth by using the hole-drilling method [44]. Kelsey is also known for using blind holes instead of through holes.
- The work of Rendler and Vigness [45], in 1966, turned the IHD method into a systematised and easily reproducible procedure. They also geometrically defined the ASTM E 837-99 type A strain gauge rosette.
- An important step was also taken in 1971, when Beaney and Procter perfected the use of abrasive air jets to allow the formation of a hole without stresses induced by the friction process [46].
- In 1978, Bijak-Zochowski was the first to describe a reliable method for the calculation of non-uniform residual stresses in depth (first reference to the so-called integral method) [30].
- Regarding the theoretical field, in 1981, Schajer achieved the first generalised study of the IHD, using a finite element analysis (FEA). He established a numerical procedure for obtaining the calibration coefficients (in isotropic materials) using a FEA, also demonstrating the independence of these coefficients from the material properties [47].
- In 1982, Flaman proposed ultra-high speed drilling as a process that did not introduce residual stresses in steels [48].
- In 1994, Zhu and Smith presented a theoretical analysis in order to apply the method to curved surfaces [49]. In the same year, Schajer and Yang developed the method to be used in situations of elastic orthotropy (common in modern materials such as fibre reinforced composites) considering only uniform stresses in depth [37].
- Tootoonian and Schajer proposed, in 1995, a hole drilled incrementally with a progressive increase in diameter. This allowed to increase the sensitivity in the measurement of strain relaxation by the IHD method [50].

- In 1997, a new rosette proposal was made. This rosette had 6 extensometers and allowed the measurement and relaxation of radial and tangential strain. Thanks to this, sensitivity in measuring strains has been improved and the depth of evaluation increased. The rosette was designated a type C rosette in the revision of ASTM E 837-99.
- Sicot *et al*. [51] (2000 to 2003) published works carried out on composites where the application of the method was studied for different translation and rotation speeds. The objective was to know which parameters provide a better drill hole. The same author, in 2004, also studied the influence of the number of increments per layer [52].
- Some important modifications of ASTM E 837, up to the latest version from 2020, were carried out. In 2007, the integral method was inserted in the ASTM E 837 standard. Later, in 2013, the Tikhonov regularization was also included.
- Pagliaro and Zuccarello (2007) [53] conducted a study regarding the development and application of the through-hole drilling method for the residual stress analysis in orthotropic materials.
- In 2013, Nobre *et al.* [54] have shown that commercially available ultra-high speed milling equipment are able to obtain perfect hole shapes without observed delamination in GFRPs. In addition, induced drilling strains due to the thermomechanical effects of cutting are relatively low.
- In 2018, Smit and Reid [55] presented a work where Power Series were used for determining the residual stress in composite laminates using IHD method. In 2020, these authors also extended the use of Tikhonov regularization to incremental hole-drilling of composite laminates using the integral method. The objective was to smooth the results of residual stress distribution and to reduce stress uncertainties through Tikhonov regularization [56].
- Great contributions were also made by Magnier *et al*. [45], Shokrieh and Ghasemi [57], and Ghasemi and Mohammadi [58], for the development of the incremental hole drilling technique applied to orthotropic materials.

2.2.2. Residual Stress Calculation in Isotropic Materials

When a hole is drilled in a body that presents residual stresses, a relaxation of stresses occurs at that location. This happens because every perpendicular to a free surface (the hole surface, in this case) is necessarily a principal axis on which the shear and normal stresses are zero [32]. The elimination of these stresses on the hole surface changes the stress in the immediately surrounding region, causing the local strains on the surface of the test object to change correspondingly [32,40]. Because of this effect, there is a relation between residual stresses and relaxed strains, making it possible to calculate the residual stresses using the relaxed strain values. Furthermore, the residual stresses can either be approximately constant (uniform) with depth or can vary significantly in the depth direction (non-uniform), as shown in Figure 2.12.

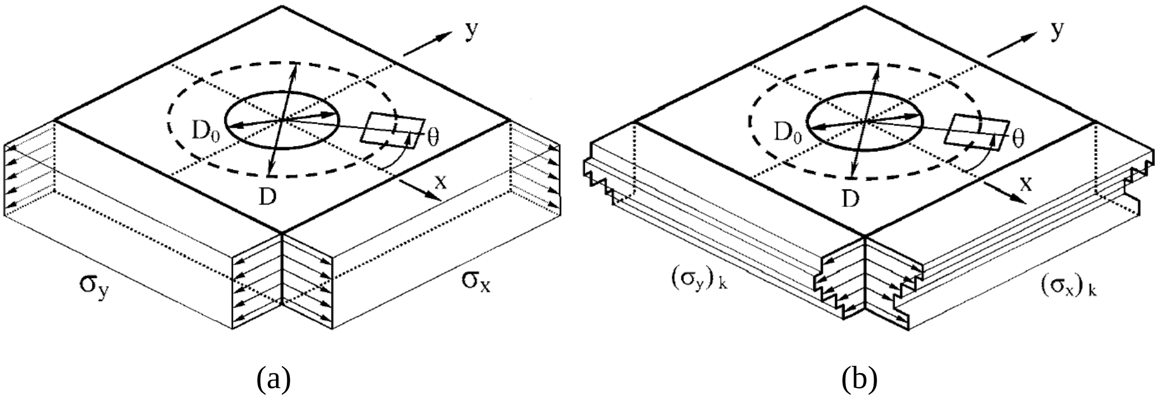

Figure 2.12. Hole geometry and residual stresses: (a) uniform stresses; (b) non-uniform stresses [28].

The surface strains that will be relieved by drilling a hole (diameter D_0) only depend on the stresses that originally existed at the boundaries of the hole [59]. Important to note that residual stresses are not necessarily along the entire depth of the region around the test location. The in-plane stresses are σ_x, σ_y and τ_{xy} throughout the thickness. From these values it is possible to determine the principal stresses σ_{max}, σ_{min} and the angle β defining the direction of the maximum principal stress σ_{max}, clockwise from the direction of gage 1 (see Figure 2.13).

Based on ASTM E 837 standard, the equations for determining in-depth residual stresses in isotropic materials are described, for both uniform and non-uniform stresses. Normally, uniform residual stress measurements are made in thin workpieces but, it can also be made for thick workpieces. Nonetheless, non-uniform residual stress measurements are only made in thick workpieces (ASTM E 837). It is important to defer between thin and thick materials. According to Nobre *et al.* [36], for a thin workpiece, the material thickness is small compared with the hole and strain gauge circle diameters, i.e., thickness ranging from $0.2D$ to D (where D represents strain gauge circle diameter). On the contrary, for a thick workpiece, the material thickness is large compared with the hole and strain gauge circle diameters, i.e., thickness greater than D to $1.2D$ [36].

2.2.2.1. Uniform Stress

Considering the simplest uniaxial residual stress case, where a thin plate is subjected to a uniform stress state and where a hole was drilled. For uniform stress state, the surface strain relief is related to the relieved principal stresses and their orientation by the following equation, based on the Kirsch's solution [61]:

$$\varepsilon_r = (A + B\cos 2\beta)\sigma_{max} + (A - B\cos 2\beta)\sigma_{min} \tag{2.1}$$

Since there are three unknown values, it is necessary three independent strain measurements and, therefore, a standard three-element strain gauge rosette is used. Figure 2.13 shows a typical three-element hole-drilling rosette, where the unknowns β, σ_{max} and σ_{min} are represented.

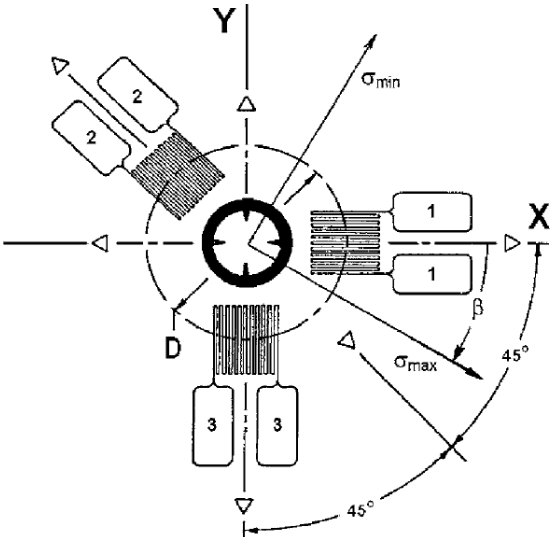

Figure 2.13. Schematic geometry of a typical three-element clock-wise (CW) hole-drilling rosette [28].

In the above Equation (2.1), A and B are two calibration constants, which depend on the geometry of the strain gauge used, the elastic properties of the material and the radius and depth of the hole. Due to its physical size, strain gauges measure an average strain rather than a point value and, thus, the new coefficients $\bar{A}$ and $\bar{B}$ are obtained by integrating over the active gauge area. An important achievement provided by Schajer in 1981 is that these constants are almost material independent, and the following relations are valid [32,48]:

$$\begin{cases} \bar{A} = \dfrac{-\bar{a}(1+\nu)}{2E} \\ \bar{B} = \dfrac{-\bar{b}}{2E} \end{cases} \tag{2.2}$$

where, $\bar{a}$ and $\bar{b}$ are dimensionless, almost material-independent and vary only with the hole geometry and strain gauge rosette used. They represent the strains measured for unit stress cases. Due to this achievement, the ASTM E 837 standard was proposed tabulating values for types A, B and C strain gauge rosettes (see Figure 2.14), based on finite element analysis over the practical limits of hole diameters and depths.

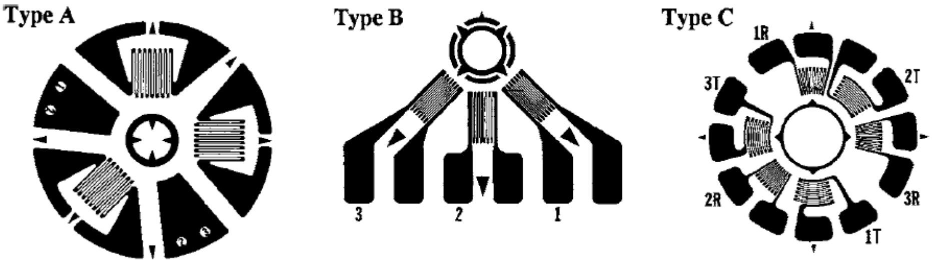

Figure 2.14. ASTM three element strain gauge rosette types (different sizes) [28].

2.2.2.2. Non-Uniform Stress

In engineering practice, however, almost all cases present a non-uniform stress field distributed over the depth. Manufacturing processes, such as welding, machining, etc. or finishing processes, such as surface treatments, to induce favourable compressive residual stresses at material surface (shot-peening, deep rolling, case hardening, nitriding, etc.) induce non-uniform stresses over the depth with relative high gradients. Due to development of calculation methods, it was possible to improve and refine the hole-drilling technique to be applied in the study of non-uniform residual stresses in depth.

In order to assess the non-uniform residual stresses that are present in a material, it is necessary to drill the hole incrementally, to a maximum depth that depends on the hole diameter. It is needed to calculate the residual stresses at each increment, based on relieved strains measured by strain gauges in the surface material. There are several methods for calculating residual stresses in a non-uniform case (e.g., integral method, power series method, average stress method, and differential method). In this work, only the integral method and the power series method will be further presented as they are considered the most important ones. For more information about the other methods see [39]. The integral method is the most accurate and used one. It assumes that the relieved strain measurements are the accumulated result of the residual stress in each of the successive depth increments. Another important method is the power series method. It assumes that the non-uniform stress can be described using a polynomial, dividing the stress field into components of a power series.

Integral Method

The integral method was proposed by Bijak-Zochowski [30] and later developed by several authors, among which Schajer's work (1988) stands out [61]. It is, theoretically, the most correct method of calculating residual stresses by IHD technique, and it is only possible due to the availability of viable calibration coefficients provided by the use of the FEM [61]. In the integral method, the contributions to the total measured strain relaxations of the stresses at all depths are considered simultaneously. It is also assumed a constant and uniform residual stress analysis in each depth increment. This is an important method because it can measure high stress gradients. However, the calculations of this method are very sensitive to experimental errors, therefore strain measurements must be extremely accurate. Also, the relieved strain values to be used are limited to approximately half the hole diameter ($Z \leq 0.2 \cdot D_0$) (D_0 is the hole diameter) as the margin error increases with depth.

In the hole integral drilling method, it is considered that for each increment in hole-depth, the total strain measured on the surface can be divided in two parts. First the relieved strain caused by residual stresses on the removed layer, and then the relieved strain due to contribution of the residual stress re-distribution caused by the change in hole-geometry (due to the removal of other layers) [58]. This relation between measured relaxed strains and residual stresses in the integral method is shown in Figure 2.15.

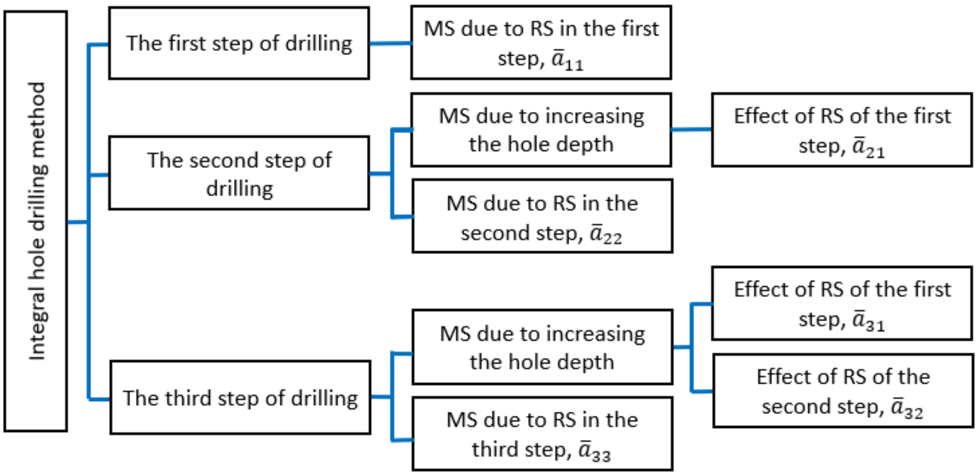

Figure 2.15. Relation between measured strains (MS) and residual stresses (RS) in the integral method for three drilling steps [58].

For the integral method, the total measured strain is the sum of the strains caused by the relaxation of the existing stresses in each increment. According to the procedure indicated by ASTM E 837 [28], the following combination strain vectors for each set of measured strains ε_1, ε_2, ε_3, have to be calculated:

$$\begin{cases} \mathrm{p_i} = \dfrac{(\varepsilon_3 + \varepsilon_1)_\mathrm{i}}{2} \\ \mathrm{q_i} = \dfrac{(\varepsilon_3 - \varepsilon_1)_\mathrm{i}}{2} \\ \mathrm{t_i} = \dfrac{(\varepsilon_3 + \varepsilon_1 - 2\varepsilon_2)_\mathrm{i}}{2} \end{cases} \tag{2.3}$$

where p corresponds to the isotropic (equi-biaxial) strain, q are the 45° shear strain and t are the x-y shear strain. The components p_i, q_i and t_i, after i increments, are given by:

$$\begin{cases} \mathrm{p_i} = \dfrac{1+\nu}{\mathrm{E}} \displaystyle\sum_{\mathrm{i=1}}^{\mathrm{j=i}} \bar{\mathrm{a}}_{\mathrm{ij}} \mathrm{P_j} \\ \mathrm{q_i} = \dfrac{1}{\mathrm{E}} \displaystyle\sum_{\mathrm{i=1}}^{\mathrm{j=i}} \bar{\mathrm{b}}_{\mathrm{ij}} \mathrm{Q_j} \qquad , \qquad 1 \le \mathrm{j} \le \mathrm{i} \\ \mathrm{t_i} = \dfrac{1}{\mathrm{E}} \displaystyle\sum_{\mathrm{i=1}}^{\mathrm{j=i}} \bar{\mathrm{b}}_{\mathrm{ij}} \mathrm{T_j} \end{cases} \tag{2.4}$$

For the first equation present in (2.4), the matrix form is:

$$\bar{\mathrm{a}}\,\mathrm{P} = \frac{\mathrm{E}}{1+\nu}\,\mathrm{p} \tag{2.5}$$

where, for a hole of i increments:

$$\mathrm{p} = \begin{bmatrix} \mathrm{p}_1 \\ \mathrm{p}_2 \\ \mathrm{p}_3 \\ \vdots \\ \mathrm{p}_\mathrm{i} \end{bmatrix} \qquad \bar{\mathrm{a}} = \begin{bmatrix} \bar{\mathrm{a}}_{11} & 0 & 0 & \cdots & 0 \\ \bar{\mathrm{a}}_{21} & \bar{\mathrm{a}}_{22} & 0 & \cdots & 0 \\ \bar{\mathrm{a}}_{31} & \bar{\mathrm{a}}_{32} & \bar{\mathrm{a}}_{33} & \cdots & 0 \\ \vdots & \vdots & \vdots & \ddots & \vdots \\ \bar{\mathrm{a}}_{\mathrm{i}1} & \bar{\mathrm{a}}_{\mathrm{i}2} & \bar{\mathrm{a}}_{\mathrm{i}3} & \cdots & \bar{\mathrm{a}}_{\mathrm{ij}} \end{bmatrix} \qquad \mathrm{P} = \begin{bmatrix} \mathrm{P}_1 \\ \mathrm{P}_2 \\ \mathrm{P}_3 \\ \vdots \\ \mathrm{P}_\mathrm{j} \end{bmatrix}$$

For the next equations, the corresponding vectors and matrices are very similar. It should be noted that both matrix $[\bar{a}]$ and $[\bar{b}]$ are lower triangle matrices. Their lines correspond to the strain relaxation due to the applied stress in varied increment, keeping the hole depth constant.

The relieved strain (measured on the surface) after performing i steps in the hole depends on the residual stresses that exist in that material from the first to the i increment $(1 \leq j \leq i)$. The calibration constants $\bar{a}_{ij}$ and $\bar{b}_{ij}$ (presented in Equations (2.4)) relate the relieved strains with the residual stresses. They indicate the relieved strains in a hole i steps deep, due to unit stresses within a hole step j [58]. The interpretation of de calibration constants is shown in Figure 2.16.

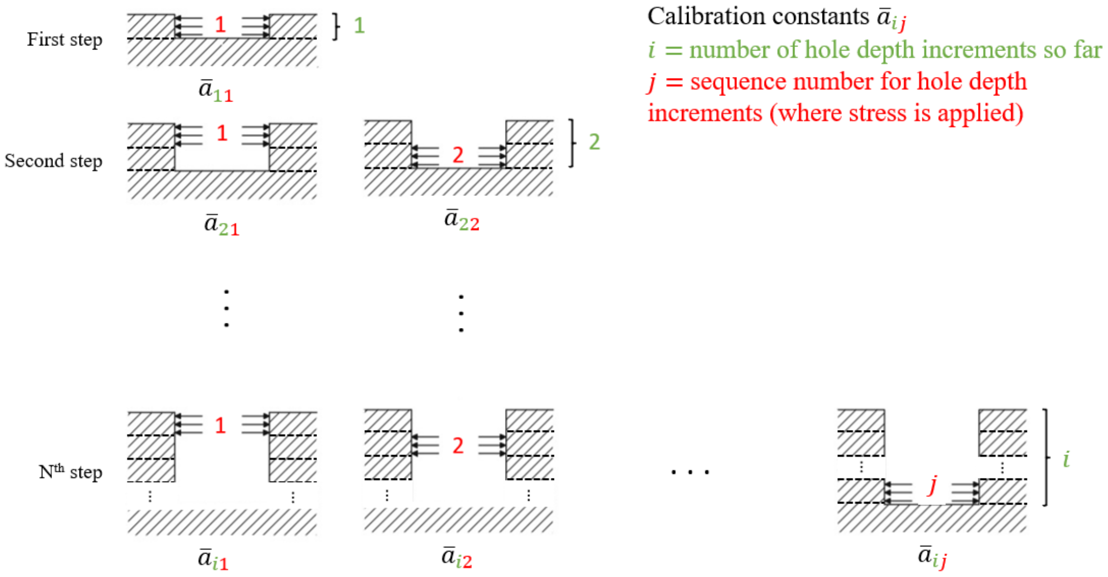

Figure 2.16. Physical interpretation of coefficients $\bar{\mathbf{a}}_{\mathbf{ij}}$ for the integral method. (adapted from article [56]).

The σ_{max}, σ_{min} and β values for each set of measurements corresponding to each increment, are calculated using the equations:

$$(\sigma_{\max})_j, (\sigma_{\min})_j = P_j \pm \sqrt{{Q_j}^2 + {T_j}^2} \tag{2.6}$$

$$\beta_j = \frac{1}{2}\arctan\left(\frac{-T_j}{-Q_j}\right) \tag{2.7}$$

They are nearly the same as the equations used for uniform stress, but in this case the calculation is done for each increment.

Power Series Method

The power series method was introduced by Schajer in 1981 [47]. By using weighted averages, this method allows to minimise the influence of random errors in the relieved strain measurement. Thus, there is a substantial improvement in the numerical stability and reliability of calculations, especially if many strain measurements are made in small increments, contrary to the integral method. The disadvantage of this method is that it has a lower spatial resolution. Finite element calculations are used to compute series of coefficients ${}^0\bar{a}(h)$, ${}^1\bar{a}(h)$, ${}^2\bar{a}(h)$ and ${}^0\bar{b}(h)$, ${}^1\bar{b}(h)$, ${}^2\bar{b}(h)$, these corresponding to the strain responses when hole-drilling into stress fields with power series variations with depth h. This is, ${}^0\sigma(h) = 1, {}^1\sigma(h) = h$, ${}^2\sigma(h) = h^2$, etc. Thus, the value of each component of the power series ${}^0\sigma(h)$, ${}^1\sigma(h)$, ${}^2\sigma(h)$, etc., is determined relative to the original residual stress field. In practice, two terms are typically used (linear distributions in depth). Applying the least squares method, the P component is obtained by solving the equation:

$$\begin{bmatrix} \sum \bar{a}_0\bar{a}_0 & \sum \bar{a}_0\bar{a}_1 \\ \sum \bar{a}_1\bar{a}_0 & \sum \bar{a}_1\bar{a}_1 \end{bmatrix} \begin{bmatrix} P_0 \\ P_1 \end{bmatrix} = \frac{E}{1+\nu} \begin{bmatrix} \sum \bar{a}_0 p \\ \sum \bar{a}_0 p \end{bmatrix} \tag{2.8}$$

The Q and T components are obtained by equations identical to Equation (2.8).

One of the most current methods, presented by Smit and Reid [56] for determining residual stresses is based on this method. However, rather than using it for determine the residual distribution through the total hole depth, they came up with the idea of considering the method for each layer of the laminate.

2.2.3. Residual Stress Calculation in Composite Laminates

Since composite laminates are anisotropic and layered materials, presenting different properties through it, there is a non-uniform residual stress along its depth. The calculation of residual stresses in hybrid components are distinct from what is used in isotropic materials with non-uniform stress field (ASTM E 837 [28]). Measuring the residual stresses in fibre reinforced composites, the calibration coefficients that relate the residual stress existing in a depth increment with the relieved strains measured at material surface, depend directly on the elastic constants of the material. Every time a new material is analysed, new coefficients need to be calculated by FEM. Because of this, it becomes an impossible task to develop a standard methodology for determination of residual stresses in composite materials.

The integral method used for isotropic materials cannot be applied for composite materials, as mentioned in [62]. As an alternative, Equation (2.9), where relieved strain and residual stress can be related are presented below, being applicable for any material where a linear elastic behaviour is assumed [45].

$$\begin{bmatrix} \varepsilon_1 \\ \varepsilon_3 \\ \varepsilon_2 \end{bmatrix} = \begin{bmatrix} C^{11} & C^{12} & C^{13} \\ C^{21} & C^{22} & C^{23} \\ C^{31} & C^{32} & C^{33} \end{bmatrix} \cdot \begin{bmatrix} \sigma_x \\ \sigma_y \\ \tau_{xy} \end{bmatrix} = [C] \cdot (\sigma) \tag{2.9}$$

The matrix $[C]$, instead of a single calibration coefficient, in Equation (2.9), result from the material being anisotropic, as the 9 coefficients C^{kl} directly depend on the elastic constants of the material. By imposing a unit uniform stress value σ_x, it contributes to strain values ε_1, ε_3 and ε_2. The contribution of this single stress value (σ_x) on the relieved strains measured is given by the coefficients C^{11}, C^{21} and C^{31}, respectively. For calculating the calibration coefficients C^{12}, C^{22} and C^{32} a unit load is applied in the y direction (σ_y) and for the coefficients C^{13}, C^{23} and C^{33}, they can be obtained by imposing the in-plane unit shear load (τ_{xy}), [23,45,58]. The Figure 2.17 shows a strain gauge rosette placement as well as the localised strain gauges that correspond to the measured relieved strains ε_1, ε_2, ε_3, and the direction of the imposed stresses σ_x, σ_y, τ_{xy}.

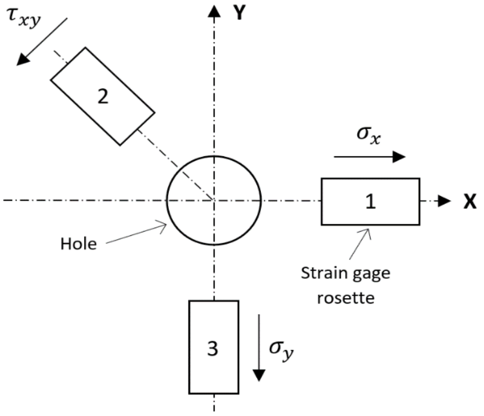

Figure 2.17. Example of a strain gauge rosette placement.

For measuring a non-uniform residual stress state in anisotropic and layered materials, Akbari *et al.* [63] proposed the pulse integral method. The equation that results from the application of this method, where the Equation (2.9) was expanded by using the integral incremental formalism, is [45,58]:

$$(\varepsilon)_i = \begin{bmatrix} \varepsilon_1 \\ \varepsilon_3 \\ \varepsilon_2 \end{bmatrix}_i = \sum_{j=1}^{i} \begin{bmatrix} C^{11} & C^{12} & C^{13} \\ C^{21} & C^{22} & C^{23} \\ C^{31} & C^{32} & C^{33} \end{bmatrix}_{ij} \cdot \begin{bmatrix} \sigma_x \\ \sigma_y \\ \tau_{xy} \end{bmatrix}_j = \sum_{j=1}^{i} [C]_{ij} \cdot (\sigma)_j, 1 \leq j \leq i \qquad (2.10)$$

In this case, although it is a non-uniform stress situation, the residual stress state within each depth increment is considered constant and uniform. Each matrix $[C]_{ij}$ in Equation (2.10) is composed by 9 coefficients C^{kl} for evaluating residual stress. The coefficient C_{ij}^{kl} inside the matrix $[C]_{ij}$ depends not only on the residual stress $(\sigma)_j$ in the present jth increment, but also on all the residual stresses which were present in all previously drilled increments. For an easier comprehension, the general expanded matrix equation, for a situation where i increments are performed, is following represented (in Figure 2.18), with some extra information.

The matrix $[C]_{kl}^{ij}$ is lower triangular (since only stresses that exist within the hole contribute to measured relieved strains) and square, as the number of rows (equal to the number of columns) represents the number of increments in the drilled hole ($i \times i$). The interpretation of de calibration coefficient sub-matrices is shown in Figure 2.19. It is similar for isotropic materials (Figure 2.16), but in place of the calibration constants, there are sub-matrices of calibration coefficients, this due to the dependance on the elastic constants of the anisotropic and layered material.

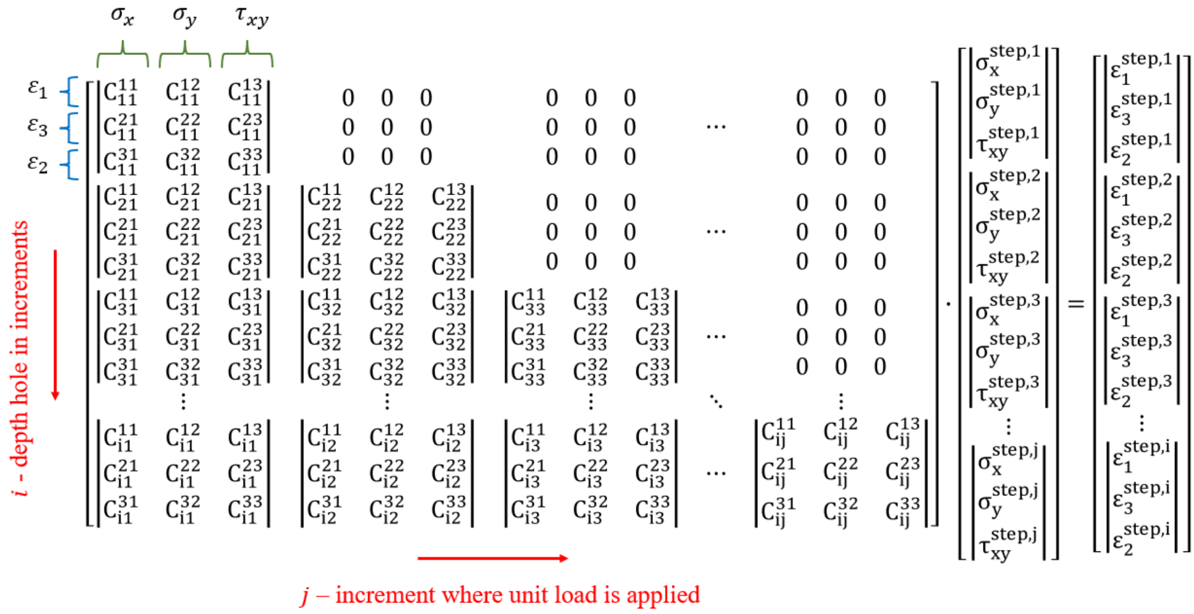

Figure 2.18. General matrix format of the Equation (2.10) corresponding to the integral method (adapted form article [58]).

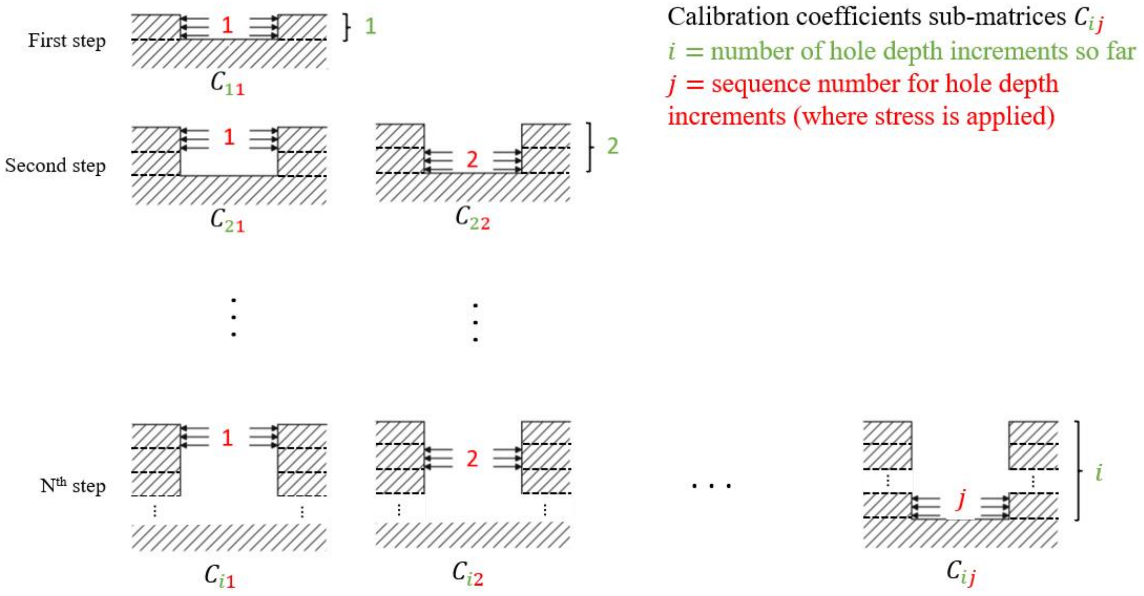

Figure 2.19. Physical interpretation of 2D calibration coefficients $\boldsymbol{C_{ij}}$ for the integral method. (adapted from article [56]).

To determine the residual stresses from the integral equations, numerical solutions are required [64]. Two ways of obtaining residual stresses are presented in this work.

Inverse problem by Tikhonov regularization

It is possible to solve the Equation (2.10) by an inverse problem, using Tikhonov regularization. This method, successfully used in isotropic materials to reduce uncertainty in residual stress determination, due to measurement errors, can be applied in composite laminates, but just through the use of an approximation. This because there is no trigonometric relationship between residual stresses and residual strains as there is for isotropic materials and, therefore, decoupling of equi-biaxial and shear components of residual stress is not possible. However, for orthotropic laminates, Tikhonov regularization can be applied separately to the primary strain in each measurement direction through simplifying approximations [56]. The approach consists of considering the use of regularization independently for x and y, considering that the shear stresses are negligible. For this specific situation, a part of equation shown in Figure 2.18 is presented in a simple form by Equation (2.11). Where $\{\varepsilon_1, \varepsilon_2, \varepsilon_3, \cdots, \varepsilon_i\}^T$ corresponds to measured strains in the same strain gauge for all increments. $\{\sigma_1, \sigma_2, \sigma_3, \cdots, \sigma_j\}^T$ corresponds to the residual stresses for all increments, where only one load case is applied, and matrix $[C]$ is composed by all coefficients C_{ij}^{kl}, existing in matrix $[C]_{ij}^{kl}$ from Figure 2.18, when k and l do not vary.

$$\begin{bmatrix} \varepsilon_1 \\ \varepsilon_2 \\ \varepsilon_3 \\ \vdots \\ \varepsilon_i \end{bmatrix} = \begin{bmatrix} C_{11} & 0 & 0 & \cdots & 0 \\ C_{21} & C_{22} & 0 & \cdots & 0 \\ C_{31} & C_{32} & C_{33} & \cdots & 0 \\ \vdots & \vdots & \vdots & \ddots & \vdots \\ C_{i1} & C_{i2} & C_{i3} & \cdots & C_{ij} \end{bmatrix} \cdot \begin{bmatrix} \sigma_1 \\ \sigma_2 \\ \sigma_3 \\ \vdots \\ \sigma_j \end{bmatrix} \tag{2.11}$$

By adding a penalty function to Equation (2.11), where $[D]$ is the matrix to define the penalization type, it is possible to improve the stabilization of the calculated results:

$$[\mathrm{C}]^T[\varepsilon] = ([C]^T[C] + \alpha[D]^T[D])[\sigma] \tag{2.12}$$

For taking into account the discontinuities at the interfaces between materials, the rows of matrix $[D]$ on both sides of an interface need to be zero. As α is the regularization parameter, an estimate of the optimal value can be iteratively determined by using Morozov Discrepancy Principle [65]. The Equation (2.12) is implemented separately for each stress component (x and y). More about the use of Tikhonov regularization in anisotropic and layered materials can be seen in articles [34,56].

Iterative method

Another alternative resolution, based on Magnier’s [45] and Ghasemi’s [58] works, is solving the Equation (2.10), as a function of residual stresses in a iterative solving process. With this direct process of substitution, it is possible to obtain the global equation capable of determining the corresponding residual stresses for each increment. Still, this iterative method causes the solutions to be quite sensitive to measurement errors for the ill-conditioned $[C]_{ij}$, as well as the inverse solution, so the Tikhonov regularization should get better results. The iterative resolution process is further developed in the following chapter, as this was the solving process chosen to be used in this work.

3. METHOD FOR CALCULATING RESIDUAL STRESSES IN FMLS AND SOFTWARE DEVELOPMENT

The rosette is attached on the specimen surface, so the relieved strains are read in the surface part, while the non-uniform stresses exist through thickness. Since there is a difference in depth of the residual stresses and the measured relieved strains, and all stress components in all material removed affect the measured strains, residual stresses and relieved strains do not present a one-to-one relationship [56,58]. As already mentioned, calibration coefficients relate the residual stresses that exist initially in the material with the relaxed strains measured on the specimen surface. Integral equations govern the relationship between the residual stresses and the measured strains, with the calibration coefficients always being part of them. An integral matrix equation that relates these variables was presented in the previous chapter (Figure 2.18). It is necessary to solve the system of equations as a function of the variable residual stress. It was already mentioned that the system of equations can be solved by the inverse problem using Tikhonov regularization. This method, prescribed by the ASTM standard, is more efficient for ill-conditioned numerical cases, and usually involved in inverse problems, as in the case of the incremental hole-drilling residual stress calculation. This approach is a good choice, since this method is able to smooth the final residual stress values and, therefore, the scattering, in particular for the deeper increments. Since South African partners (Wits University) developed and determine the residual stresses by this method, our final results will be compared with Tikhonov regularization.

In this work, Equation (2.10) was solved by an iterative solving method, that was also used by Magnier [45] and Ghasemi [58]. First, and to facilitate the problem solving, the equation was divided in two parts (see Figure 2.15): the relieved strain caused by residual stresses on the removed layer (sub-matrix that lie on the diagonal of the whole matrix and residual stresses (i)) and the relieved strain due to contribution of the residual stress redistribution caused by the change in hole-geometry (remaining sub-matrices and residual stresses (j)), for each line (increment), as shown in the Equation (3.1).

$$\begin{bmatrix} \varepsilon_1 \\ \varepsilon_3 \\ \varepsilon_2 \end{bmatrix}_i = \sum_{j=1}^{i-1} \begin{bmatrix} C^{11} & C^{12} & C^{13} \\ C^{21} & C^{22} & C^{23} \\ C^{31} & C^{32} & C^{33} \end{bmatrix}_{ij} \cdot \begin{bmatrix} \sigma_x \\ \sigma_y \\ \tau_{xy} \end{bmatrix}_j + \begin{bmatrix} C^{11} & C^{12} & C^{13} \\ C^{21} & C^{22} & C^{23} \\ C^{31} & C^{32} & C^{33} \end{bmatrix}_{ii} \cdot \begin{bmatrix} \sigma_x \\ \sigma_y \\ \tau_{xy} \end{bmatrix}_i \tag{3.1}$$

Then, the equation was developed as a function of the residual stresses for each increment, while the sub-matrices that lie diagonally, become inverse matrices:

$$\begin{bmatrix} \sigma_x \\ \sigma_y \\ \tau_{xy} \end{bmatrix}_i = \begin{bmatrix} C^{11} & C^{12} & C^{13} \\ C^{21} & C^{22} & C^{23} \\ C^{31} & C^{32} & C^{33} \end{bmatrix}_{ii}^{-1} \cdot \left[\begin{bmatrix} \varepsilon_1 \\ \varepsilon_3 \\ \varepsilon_2 \end{bmatrix}_i - \sum_{j=1}^{i-1} \begin{bmatrix} C^{11} & C^{12} & C^{13} \\ C^{21} & C^{22} & C^{23} \\ C^{31} & C^{32} & C^{33} \end{bmatrix}_{ij} \cdot \begin{bmatrix} \sigma_x \\ \sigma_y \\ \tau_{xy} \end{bmatrix}_j \right] \tag{3.2}$$

As already mentioned, for each drilling increment, there is an influence by the previous ones. This influence can be seen in Equation (3.2), when residual stresses are determined, increment by increment, taking into account all previous residual stresses. The sub-matrices which are part of the same row of the whole matrix (Figure 2.18) are used in resolution of each equation corresponding to its incremental depth i. For a better understanding, the equations used to obtain the residual stresses within three depth increments are presented below.

For the first drilling increment, residual stresses are determined by:

$$\begin{bmatrix} \sigma_x \\ \sigma_y \\ \tau_{xy} \end{bmatrix}_1 = \begin{bmatrix} C_{11}^{11} & C_{11}^{12} & C_{11}^{13} \\ C_{11}^{21} & C_{11}^{22} & C_{11}^{23} \\ C_{11}^{31} & C_{11}^{32} & C_{11}^{33} \end{bmatrix}^{-1} \begin{bmatrix} \varepsilon_1 \\ \varepsilon_3 \\ \varepsilon_2 \end{bmatrix}_1 \tag{3.3}$$

In the second drilling increment, residual stresses are:

$$\begin{bmatrix} \sigma_x \\ \sigma_y \\ \tau_{xy} \end{bmatrix}_2 = \begin{bmatrix} C_{22}^{11} & C_{22}^{12} & C_{22}^{13} \\ C_{22}^{21} & C_{22}^{22} & C_{22}^{23} \\ C_{22}^{31} & C_{22}^{32} & C_{22}^{33} \end{bmatrix}^{-1} \left[\begin{bmatrix} \varepsilon_1 \\ \varepsilon_3 \\ \varepsilon_2 \end{bmatrix}_2 - \begin{bmatrix} C_{21}^{11} & C_{21}^{12} & C_{21}^{13} \\ C_{21}^{21} & C_{21}^{22} & C_{21}^{23} \\ C_{21}^{31} & C_{21}^{32} & C_{21}^{33} \end{bmatrix} \begin{bmatrix} \sigma_x \\ \sigma_y \\ \tau_{xy} \end{bmatrix}_1 \right] \tag{3.4}$$

For the third drilling increment, residual stresses are obtained by:

$$\begin{aligned} \begin{bmatrix} \sigma_x \\ \sigma_y \\ \tau_{xy} \end{bmatrix}_3 = \begin{bmatrix} C_{33}^{11} & C_{33}^{12} & C_{33}^{13} \\ C_{33}^{21} & C_{33}^{22} & C_{33}^{23} \\ C_{33}^{31} & C_{33}^{32} & C_{33}^{33} \end{bmatrix}^{-1} & \left[\begin{bmatrix} \varepsilon_1 \\ \varepsilon_3 \\ \varepsilon_2 \end{bmatrix}_3 - \begin{bmatrix} C_{31}^{11} & C_{31}^{12} & C_{31}^{13} \\ C_{31}^{21} & C_{31}^{22} & C_{31}^{23} \\ C_{31}^{31} & C_{31}^{32} & C_{31}^{33} \end{bmatrix} \begin{bmatrix} \sigma_x \\ \sigma_y \\ \tau_{xy} \end{bmatrix}_1 \right. \\ & \left. - \begin{bmatrix} C_{32}^{11} & C_{32}^{12} & C_{32}^{13} \\ C_{32}^{21} & C_{32}^{22} & C_{32}^{23} \\ C_{32}^{31} & C_{32}^{32} & C_{32}^{33} \end{bmatrix} \begin{bmatrix} \sigma_x \\ \sigma_y \\ \tau_{xy} \end{bmatrix}_2 \right] \end{aligned} \tag{3.5}$$

To solve the general equation for each increment, a code in Python was created. By implementing the Equation (3.2), the code gives us the values of residual stresses corresponding to each increment, $\{\sigma_x, \sigma_y, \tau_{xy}\}_j^T$. It is important to note that the coefficient matrix obtained by the FEM, through a 3D simulation, presents a different format from the matrix presented in Figure 2.18. Nonetheless, the calibration coefficients C_{ij}^{kl} present in each are the same, just differentiating in its location. The whole matrix obtained by FEM is shown in Equation (3.6) and has 9 lower triangular sub-matrices $[C]^{kl}$ associated.

$$\begin{bmatrix} |\mathrm{C}^{11}| & |\mathrm{C}^{12}| & |\mathrm{C}^{13}| \\ |\mathrm{C}^{21}| & |\mathrm{C}^{22}| & |\mathrm{C}^{23}| \\ |\mathrm{C}^{31}| & |\mathrm{C}^{32}| & |\mathrm{C}^{33}| \end{bmatrix}
= \begin{bmatrix}
\begin{vmatrix} \mathrm{C}_{11}^{11} & 0 & \cdots & 0 \\ \mathrm{C}_{21}^{11} & \mathrm{C}_{22}^{11} & \cdots & 0 \\ \vdots & \vdots & \ddots & \vdots \\ \mathrm{C}_{i1}^{11} & \mathrm{C}_{i2}^{11} & \cdots & \mathrm{C}_{ij}^{11} \end{vmatrix} &
\begin{vmatrix} \mathrm{C}_{11}^{12} & 0 & \cdots & 0 \\ \mathrm{C}_{21}^{12} & \mathrm{C}_{22}^{12} & \cdots & 0 \\ \vdots & \vdots & \ddots & \vdots \\ \mathrm{C}_{i1}^{12} & \mathrm{C}_{i2}^{12} & \cdots & \mathrm{C}_{ij}^{12} \end{vmatrix} &
\begin{vmatrix} \mathrm{C}_{11}^{13} & 0 & \cdots & 0 \\ \mathrm{C}_{21}^{13} & \mathrm{C}_{22}^{13} & \cdots & 0 \\ \vdots & \vdots & \ddots & \vdots \\ \mathrm{C}_{i1}^{13} & \mathrm{C}_{i2}^{13} & \cdots & \mathrm{C}_{ij}^{13} \end{vmatrix} \\
\begin{vmatrix} \mathrm{C}_{11}^{21} & 0 & \cdots & 0 \\ \mathrm{C}_{21}^{21} & \mathrm{C}_{22}^{21} & \cdots & 0 \\ \vdots & \vdots & \ddots & \vdots \\ \mathrm{C}_{i1}^{21} & \mathrm{C}_{i2}^{21} & \cdots & \mathrm{C}_{ij}^{21} \end{vmatrix} &
\begin{vmatrix} \mathrm{C}_{11}^{22} & 0 & \cdots & 0 \\ \mathrm{C}_{21}^{22} & \mathrm{C}_{22}^{22} & \cdots & 0 \\ \vdots & \vdots & \ddots & \vdots \\ \mathrm{C}_{i1}^{22} & \mathrm{C}_{i2}^{22} & \cdots & \mathrm{C}_{ij}^{22} \end{vmatrix} &
\begin{vmatrix} \mathrm{C}_{11}^{23} & 0 & \cdots & 0 \\ \mathrm{C}_{21}^{23} & \mathrm{C}_{22}^{23} & \cdots & 0 \\ \vdots & \vdots & \ddots & \vdots \\ \mathrm{C}_{i1}^{23} & \mathrm{C}_{i2}^{23} & \cdots & \mathrm{C}_{ij}^{23} \end{vmatrix} \\
\begin{vmatrix} \mathrm{C}_{11}^{31} & 0 & \cdots & 0 \\ \mathrm{C}_{21}^{31} & \mathrm{C}_{22}^{31} & \cdots & 0 \\ \vdots & \vdots & \ddots & \vdots \\ \mathrm{C}_{i1}^{31} & \mathrm{C}_{i2}^{31} & \cdots & \mathrm{C}_{ij}^{31} \end{vmatrix} &
\begin{vmatrix} \mathrm{C}_{11}^{32} & 0 & \cdots & 0 \\ \mathrm{C}_{21}^{32} & \mathrm{C}_{22}^{32} & \cdots & 0 \\ \vdots & \vdots & \ddots & \vdots \\ \mathrm{C}_{i1}^{32} & \mathrm{C}_{i2}^{32} & \cdots & \mathrm{C}_{ij}^{32} \end{vmatrix} &
\begin{vmatrix} \mathrm{C}_{11}^{33} & 0 & \cdots & 0 \\ \mathrm{C}_{21}^{33} & \mathrm{C}_{22}^{33} & \cdots & 0 \\ \vdots & \vdots & \ddots & \vdots \\ \mathrm{C}_{i1}^{33} & \mathrm{C}_{i2}^{33} & \cdots & \mathrm{C}_{ij}^{33} \end{vmatrix}
\end{bmatrix} \tag{3.6}$$

These sub-matrices' format $[C]^{kl}$ is presented in Equation (3.7) and each one corresponds to a load case (l) and a strain (k) record.

$$\mathrm{C}^{\mathrm{kl}} = \begin{bmatrix} \mathrm{C}_{11}^{\mathrm{kl}} & 0 & 0 & \cdots & 0 \\ \mathrm{C}_{21}^{\mathrm{kl}} & \mathrm{C}_{22}^{\mathrm{kl}} & 0 & \cdots & 0 \\ \mathrm{C}_{31}^{\mathrm{kl}} & \mathrm{C}_{32}^{\mathrm{kl}} & \mathrm{C}_{33}^{\mathrm{kl}} & \cdots & 0 \\ \vdots & \vdots & \vdots & \ddots & \vdots \\ \mathrm{C}_{i1}^{\mathrm{kl}} & \mathrm{C}_{i2}^{\mathrm{kl}} & \mathrm{C}_{i3}^{\mathrm{kl}} & \cdots & \mathrm{C}_{ij}^{\mathrm{kl}} \end{bmatrix} \tag{3.7}$$

Therefore, in this code it was necessary to transform the obtained matrix (3.6) into a matrix with the same format as presented in Figure 2.18, so that it was possible to calculate the residual stresses through the use of Equation (3.2). The script created, capable to solve, by iterative method, the system of equations presented by the integral method, can be seen in ANNEX A

4. MATERIALS AND EXPERIMENTAL PROCEDURE

To study the mechanical behaviour or to determine residual stresses, it is very important to consider what material is used and its properties, since for FMLs there is a great dependence on the material properties and the stacking ply strategy. In the case of the IHD, the calibration coefficients, necessary for residual stresses calculation, are dependent of the fibre properties (orthotropic in nature), but also of such strategy. The manufacturing/forming process used, ends up having its influence on the existence of residual stresses and in their corresponding amplitude. The FML used in the present work was glass fibre reinforced polymer embedded with steel.

During IHD tests, to determine the relaxed strains caused by the relief of residual stresses, it was necessary to carry out the experimental procedure of the IHD method. The incremental hole-drilling performed on the specimens was done carefully and always following the rules for this technique to obtain viable relaxed strain values. A description of each step of this process is given, from the moment the specimen is prepared to the end of the determination of the relieved strains.

4.1. GFRP/Steel Material

GFRP composites are highly favourable structural materials in aerospace and automotive applications due to their superior high strength-to-weight ratio, but their brittle failure behaviour compromises the structural integrity and damage tolerance in case of impact or crash event. Since metallic materials are comparatively more ductile but heavier, by combining metals and GFRP, a hybrid composite with optimised mechanical properties is obtained [38].

4.1.1. Manufacturing Process

Samples were manufactured by using an advanced intrinsic manufacturing technology, where two plies of cross ply prepreg glass were pressed and bonded together on both sides of an internal steel sheet (1 mm). For increasing the bonding behaviour of dissimilar materials, the surface of the metal side was processed by sand blasting before manufacturing for increasing the surface roughness, thus improving the mechanical interlocking. In the manufacturing process of the samples, prepared glass fibre prepregs [0º/90º] with a thickness of 0.44 mm (2 plies) were first placed into a heated die with the dimension of 100 mm × 250 mm × 20 mm. As the next step, a thin metal sheet with thickness of 1 mm was placed on top of the GFRP prepreg and finally the same GFRP prepregs [0º/90º] were pressed onto the sheet metal by a heated punch. A pressure of 0.3 MPa and the temperature of 160 °C, with the constant curing process of 18 minutes, were employed. After curing, the samples which were not further pressed were cooled down in laboratory atmosphere with a cooling rate of approximately 100 °C/min. The objective was to obtain final samples to also allow the use of diffraction methods, in particular neutron diffraction, to complement the analysis performed by IHD and validate the obtained results. Figure 4.1 shows the designed sample configuration used in the present work.

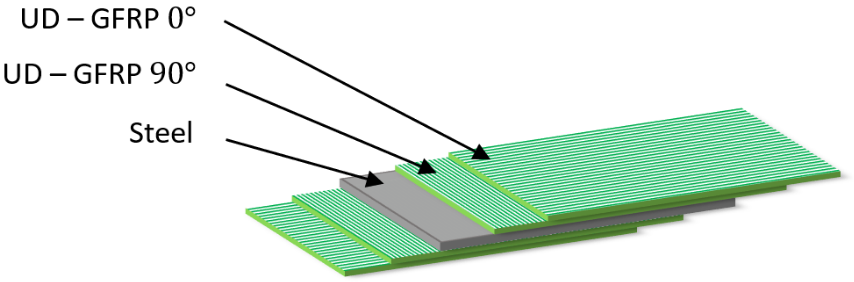

Figure 4.1. Schematic illustration of GFRP/steel FML, with $[\mathbf{0°/90°}/\boldsymbol{Steel}]_s$ configuration, used in this work.

4.1.2. Specimen Information

In this particular situation, the type of glass used was G U300-0/NF-E506/26% (with resin content 26%), while the steel employed was HC340LA (micro-alloyed steel). The relevant properties of these two materials are given in Table 4.1. The mechanical properties were experimentally determined and evaluated by using the Classical Laminate Theory (CLT). Table 4.1 presents the mechanical properties determined for the GFRP plies and steel of the hybrid composites used in the present work. The obtained values are according to DIN EN ISO 527, DIN 256 EN ISO 14129 and DIN EN ISO 6892-1.

Table 4.1. Material properties of GFRP/steel FML used in the numerical/experimental results.

	Young's Modulus (GPa)			**Poisson's Ratio**			**Shear Modulus (GPa)**		
	E_x	E_y	E_z	ν_{xy}	ν_{xz}	ν_{yz}	G_{xy}	G_{xz}	G_{yz}
GFRP	33.98	8.79	8.79	0.0861	0.3343	0.37	5.23	5.23	3.21
Steel	190000			0.29					

Final GFRP/Steel samples exhibit dimensions of 1.88 mm (thickness) × 25 mm (width) × 250 mm (length). The total thickness is divided into two pairs of glass fibre layers, where each layer is 0.22 mm thick, and 1 mm thick layer of alloy steel. A cross-section of this specimen can be seen in Figure 4.2. These specimens have this distribution of layers in order to perform different techniques on them.

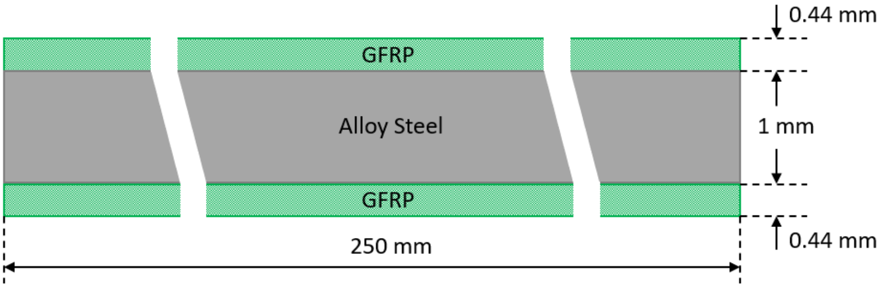

Figure 4.2. Representation of the cross-section of the specimen used in this work.

4.2. Experimental Application of the IHD Technique

The experimental procedure related to the IHD is a crucial part for determining the existing residual stresses in the material. Without obtaining the values of the relieved strains, it would not be possible to reach the residual stress values by this method. So, it is vital to make sure this process is done carefully and correctly. The experimental procedure of the IHD method can be divided into several important parts, bearing in mind that the success of all these parts depends on the operator who is carrying out the process. For a correct and complete description of the entire procedure, see [51,67].

First, the most suitable rosette for this type of application must be selected. In this study, the rosette used is an HBM rosette (RY61M) which has six strain gauges, is the same as the one shown in Figure 4.3.

For evaluation of residual stresses, only the strain information of three strain gauges is required. However, the more strain gauges used, the higher the accuracy of the values obtained. As in this case (Figure 4.3), each rosette has a diametrically opposite strain gauge, the values are obtained in pairs and an average between them is made, so if the hole is not fully centred between the strain gauges, the error that comes with it ends up disappearing. In the end, only three strain gauge values ($\varepsilon_1, \varepsilon_2, \varepsilon_3$) in each measurement were used.

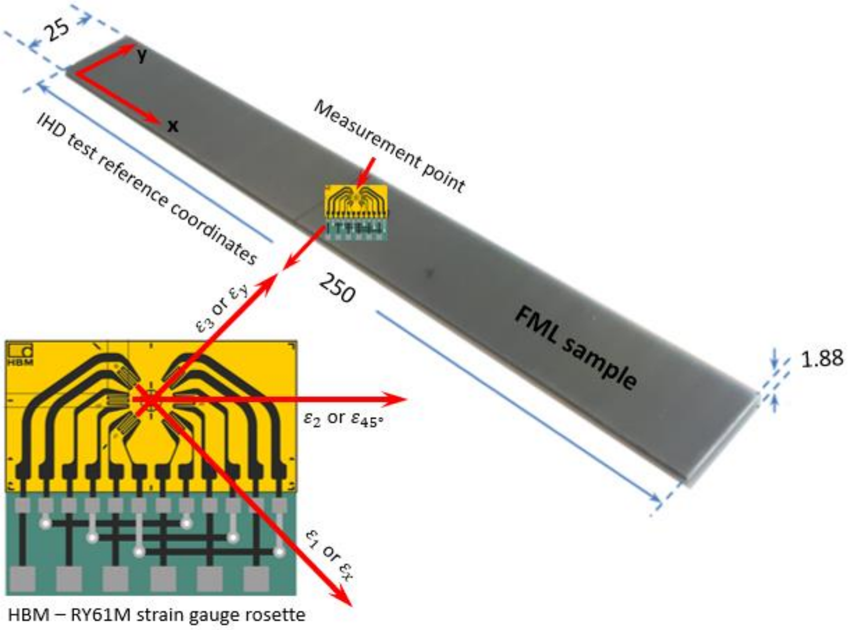

Figure 4.3. FML samples showing the stacking ply configuration, its geometry and IHD measuring point using a HBM RY61M strain gauge rosette. The IHD measuring coordinates are also shown.

To start the rosette installation, a careful prepared surface is needed. No product that could eventually change the material’s properties should be used, to avoid contamination of the material’s surface. Polishing should be avoided to ensure that no residual stresses are added to the material. Only isopropyl alcohol should be used to clean the surface of the GFRP/Steel specimens (acids and bases attack polymers).

Accurate alignment is crucial to achieve a good measurement, so it is extremely important to ensure that the drill is centred precisely at the centre of the gauge rosette. To correctly orient the rosette and to place it in the desired position, it is important to make four lines in the surface around the target centre.

To place the rosette, a special high temperature resistant glue is needed along with a catalyst to speed up the bounding. After inserting the glue into the rosette, and placing it in the desired location, finger’s pressure should be applied for a few minutes (3 min.).

After the rosette installation, it is necessary to connect the rosette to a system that can read the data and analyse it, so it can convert the information obtained by each strain gauge into relieved strain values. The electrical connection is done by connecting the rosette grids into a Wheatstone bridge circuits and by making small welds that connect the rosette grids to the cables. A spot-welding pen is used at this step of the procedure. For this particular case, relaxed surfaced strains are measured using a universal digital system, Spider 8-30, HBM. The system is connected to the computer and data acquisition is done by software Catman Express, HBM.

Regarding the drilling procedure, it is of extreme importance that the hole is drilled into the exactly target centre of the strain gauge rosette. By using the optical head provided with the drilling machine we can centre the tool holder, so when the drilling tool is placed, it will drill in the exact location. In Figure 4.4, the drilling tool and the experimental procedure can be observed.

Figure 4.4. Vishay RS 200 Milling Guide (drilling tool) existing at GTR lab and experimental procedure.

There are several end mills of varying diameter that can be used for this procedure (smaller (0.8 mm) or larger (3.2 mm)), depending on the assessment strategy. For the present work, an end mill of 1.6 mm diameter was used, where final diameter of the hole surrounded 1.8 mm. The incremental hole-drilling procedure is usually done in small increments, always measuring the relieved strains after each increment. In the experimental procedure, eighteen material removal increments were done, and very small depth increments were considered (0.01 mm) up to a depth of about 1 mm. Despite this depth value, it is not possible to consider all depth for determination of residual stresses since the values obtained at a depth greater than $0.4 \cdot D$ are not feasible [32]. As we drill, the sensitivity to measure surface strains due to stresses in depth is lost.

4.3. Neutron Diffraction Technique

Before hole-drilling, the residual stresses were previously determined, at same locations in the sample, at the South African Nuclear Energy Corporation – NECSA, by neutron diffraction.

Briefly explaining, the neutron diffraction technique uses the unique penetrating power of the neutron with the sensitivity of diffraction, to measure the separation of lattice planes within grains of polycrystalline engineering materials, thus providing an internal strain gauge. Using calibrated elastic constants, the strain is then converted to stress [27,68].

The stress investigations in South Africa (NECSA) were performed using the Materials Probe for Internal Strain Investigations (MPISI) [69] angle dispersive neutron strain scanner located at beam port 5 of the SAFARI-1 nuclear research reactor. In this technique the penetrating capabilities of thermal neutrons are used to measure the interatomic spacing of the crystal lattice structure within a well-defined gauge volume (GV), from which the lattice strain and tri-axial residual stresses can be calculated by incorporating the elasticity modulus of the material. The beam was monochromatic with a wavelength of 1.67 Å. A gauge volume of 0.2 mm × 0.2 mm × 10 mm was used and the d-spacing of the α-Fe (211) lattice plane was measured around a 2θ angle of 85.5°. The 10 mm length was aligned parallel to the surface and 0.44 mm length was aligned through the depth. This shape and orientation were chosen to reduce the gauge volume, having enough space resolution to measure high gradient residual stresses through the steel layer, since ND technique requires as large a gauge volume as possible to improve neutron counting statistics. Table 4.2 resumes the MPISI configuration parameters used during the experiments.

Table 4.2. MPISI configuration parameters for ND residual stress measurements.

Monochromator crystal plane	Si (331)
Estimated wavelength [Å]	1.648
Detector centre angle (2θ)	90.0°
Positional accuracy of calibration sample edges [mm]	~ 0.02
Primary and secondary slit distances from CoR [mm]	9
Nominal size of primary slit opening [mm^2]	0.2 × 10.0
Nominal size of secondary slit opening [mm]	0.2
Projected instrument GV [mm^3]	0.21 × 10.1 (h) × 0.21

5. NUMERICAL SIMULATION: DETERMINATION OF CALIBRATION COEFFICIENTS

As mentioned before, numerical simulation needs to be used to obtain the calibration coefficients that relate the relieved strains to the residual stresses present in the material and which are to be determined. Nine elastic constants (E_x, E_y, E_z, ν_{xy}, ν_{xz}, ν_{yz}, G_{xy}, G_{xz}, G_{yz}) are required to relate the stresses and strains in an anisotropic and layered material. For obtaining the whole $[C]_{ij}^{kl}$ matrix, the effects of σ_x, σ_y and τ_{xy} on ε are considered separately. It can be shown that all matrix values can be determined considering three different stress states. The first column of $[C]_{ij}$ can be determined by considering the uniaxial stress state $\boldsymbol{\sigma_x = 1, \sigma_y = \tau_{xy} = 0}$, the second column considering $\boldsymbol{\sigma_y = 1, \sigma_x = \tau_{xy} = 0}$, and the last column considering a pure shear stress state $\boldsymbol{\tau_{xy} = 1, \sigma_x = \sigma_y = 0}$. The unit loads are converted into the cylindrical coordinate system by Equation (5.1) [45], and σ_r and $\tau_{r\theta}$ are applied at the hole boundary within each depth increment for calculating the coefficients in the finite element model. More information on the calculation of the calibration coefficients by FEM in anisotropic materials can be found in [8,14, 34, 2].

$$\begin{bmatrix} \sigma_r \\ \tau_{r\theta} \end{bmatrix} = \begin{bmatrix} \cos^2\theta & \sin^2\theta & \sin 2\theta \\ -0.5 \cdot \sin 2\theta & 0.5 \cdot \sin 2\theta & \cos 2\theta \end{bmatrix} \cdot \begin{bmatrix} \sigma_x \\ \sigma_y \\ \tau_{xy} \end{bmatrix} \tag{5.1}$$

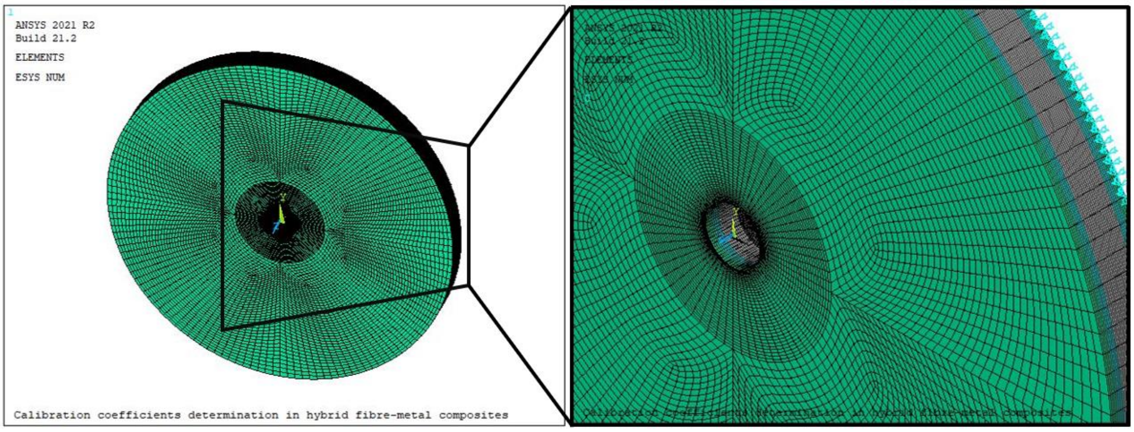

Figure 5.1. ANSYS finite element analysis mesh used for calculation of coefficients in orthotropicand layered materials (left) and an amplified view showing different layers of the material (GFRP $\mathbf{0}$°/GFRP $\mathbf{90}$°/Steel)$_s$ used in the present study (right).

In the present work, the finite element model, created from ANSYS engineering simulation software, whose its mesh is visible in Figure 5.1, is a cylindrical model with a hole diameter of 1.8 mm, the outer diameter equal to 5 times the average radius of the strain gauge rosette used (to avoid edge effects) and a total height of 1.88 mm, corresponding to the samples thicknesses (see chapter 4). Only the bottom edge at outer diameter is fixed, with the purpose of no interference in the behaviour of the material during the simulation, since the thickness of the specimen can be considered a sensitive parameter (thickness much smaller compared to its length). Two different types of elements were used to create the model. SOLID186 higher order 3-D 20-node solid element that exhibits quadratic displacement behaviour, was used to modelling the different material layers. The element is defined by 20 nodes having three degrees of freedom per node: translations in the nodal x, y, and z directions. This element was used with two ANSYS available key options: layered structural solid to model layered thick shells or solids, which allow modelling the different glass fibre plies and homogeneous structural solid to modelling the metallic (steel) layers. In addition, SURF154 3-D structural surface effect element, which is used for various load and surface effect applications in 3-D structural analyses. In this case, this element was used to apply stresses at surface for each incremental hole depth. The FEM model is composed by, approximately, three hundred thousand elements and one million and thirteen thousand nodes.

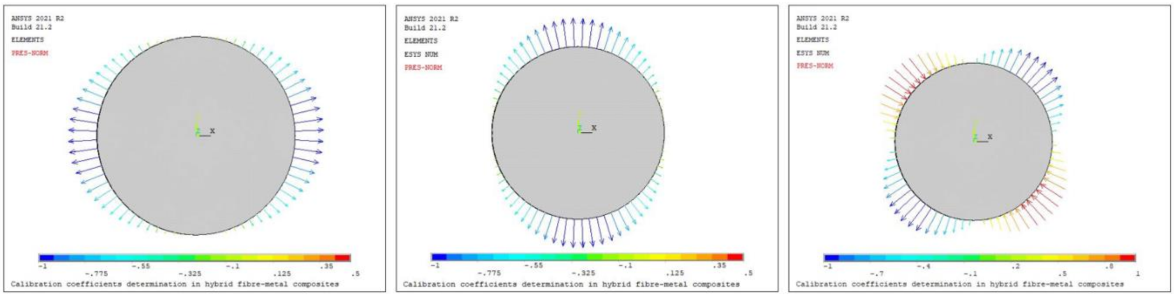

$\sigma_x = 1$ $\sigma_y = \tau_{xy} = 0$ (a)

$\sigma_y = 1$ $\sigma_x = \tau_{xy} = 0$ (b)

$\tau_{xy} = 1$ $\sigma_x = \sigma_y = 0$ (c)

Figure 5.2. Basic stress conditions that were applied to the FEM model: (a) $\boldsymbol{\sigma_x = 1, \sigma_y = \tau_{xy} = 0}$; (b) $\boldsymbol{\sigma_y = 1, \sigma_x = \tau_{xy} = 0}$; (c) $\boldsymbol{\tau_{xy} = 1, \sigma_x = \sigma_y = 0}$.

The IHD was simulated using the “birth and death of elements” ANSYS code features. For each hole depth (hole-volume removed), the load cases (a), (b) and (c) presented in Figure 5.2, and already converted into σ_r and $\tau_{r\theta}$ by Equation (5.1), were successively applied to the hole wall for each depth increment (from $j = 1$ to i). The load cases were applied to simulate the IHD procedure, as they take the role of residual stresses. After applying stress in each depth increment, the relieved strain values, in the region of each strain gauge, were obtained and Equation (2.10) was solved by inverse problem to obtain each calibration matrix element. By carrying out this process repeatedly, it was possible to determine all calibration coefficients of the whole matrix $[C]_{ij}^{kl}$ presented in Equation (3.6). As mentioned above, for calculation of the first column of equation presented in Figure 2.18, where the coefficients C_{ij}^{11}, C_{ij}^{21} and C_{ij}^{31} are part of, a stress σ_x (load case (a)) should be applied at the hole wall of each depth-increment. In other words, these three coefficients are the effects of the stress σ_x on the measured strains along the strain gauge 1, 3 and 2, respectively. The same method is applied for the second (σ_y applied) and third (τ_{xy} applied) columns (see Figure 5.3).

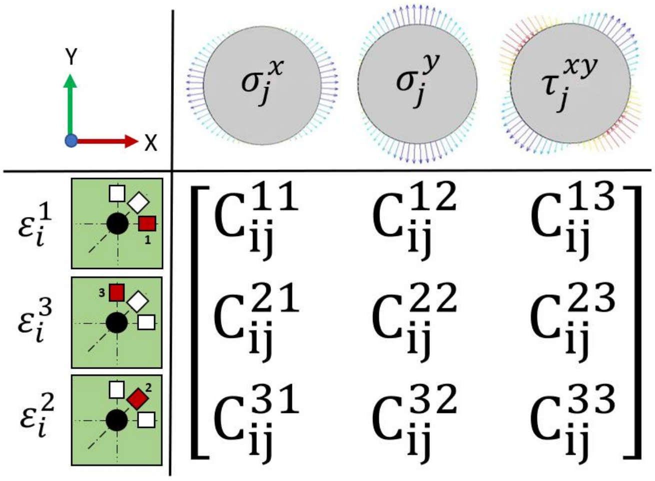

Figure 5.3. Meaning of the calibration coefficients C_{ij} in each sub-matrix (adapted from article [34]).

It is relevant to note that, in all sub-matrices, the first and second coefficients of the third column (C_{ij}^{13} and C_{ij}^{23}) are equal to zero. These coefficients are the effects of the shear residual stresses on the measured strain gauges 1 (0° direction) and 3 (90° direction), and because of the absence of shear residual stresses in them, these coefficients are equal to zero [58].

The relieved strains are obtained by a simulated rosette (Figure 5.4.a)). This rosette, used for FEM model, is identical to the 6-element strain gauge rosette RY61M from HBM (Figure 5.4.b)). Note that the three diametrically opposite strain gauges were not considered as they exist to avoid possible eccentricity effects during experimental procedure. In the end, only three strain gauge values are used.

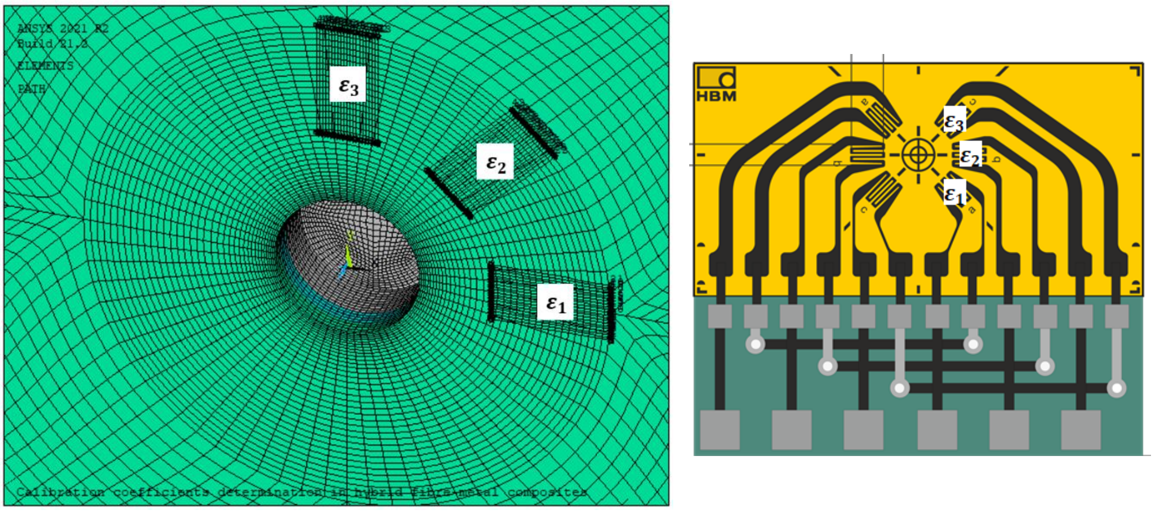

(a) (b)

Figure 5.4. (a) ANSYS finite element mesh with the location of three strain gauges representing the HBM rosette; (b) HBM rosette (RY61M) [66].

To obtain the relieved strain values caused by the three loads referred above, displacement data were used. Practical strain gauges measure strain over a finite area that corresponds to the region where they are located. When measured strains with displacements, the strain can be obtained by single integration of the displacement field along the X_1 and X_2 edges of the strain gauge area [62] – see Figure 5.5.

With (X_1, Y_1) and (X_2, Y_2) being the corner coordinates of grid line, and using the mean value theorem, the integration can be closely approximated by [62]:

$$\varepsilon^* \approx \frac{\sum_{m=1}^{n} \left(U\left(X_2, Y_{(m)}\right) - U\left(X_1, Y_{(m)}\right) \right)}{n(X_2 - X_1)} \tag{5.2}$$

Through the Equation (5.2), it is possible to observe that the relieved strain ε^* depends solely on the relative displacements along the X_1 and X_2 boundaries, and not at all on the distribution of the displacements or strains in the area between. To the case of a strain gauge oriented in any arbitrary direction, knowing that (X, Y) axes are associated with direction of the grid lines of the strain gauge and considered (x, y) axes associated with the geometry of the specimen, where ϕ is the angle between (X, Y) axes and (x, y) axes; for cartesian (x, y) coordinate system, U (displacement) is [62]:

$$U(X, Y) = u(x, y) \cos \phi + v(x, y) \sin \phi \tag{5.3}$$

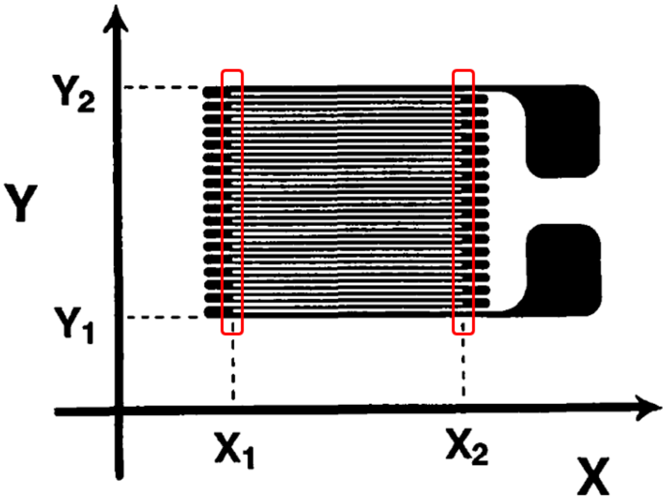

Figure 5.5. Strain gauge grid area and, marked in red, the corner coordinates of grid lines where displacements are read.

ANNEX C shows the radial and tangential strain field around the hole, obtained by the FEM simulation, for the load case (a), (b) and (c) corresponding to the first and last increment (18th increment), when the hole attained its maximum simulated depth (around 1 mm depth). The 9 sub-matrices $[C]^{kl}$ determined by numerical simulation, corresponding to the samples studied in this thesis, are presented in ANNEX B.

6. EXPERIMENTAL RESULTS AND DISCUSSION

In this chapter, all the results obtained experimentally and computationally are presented. These include the relieved strains determined by experimental IHD technique and the residual stresses calculated by the software developed. Also included for further comparison are the residual stresses obtained by the partners from Wits University, using Tikhonov regularization and those obtained by the neutron diffraction method. In addition, a numerical simulation performed in this work, where external uniform stresses were applied to a model sample, is presented. The relieved strains presented through the depth model were determined, and used, collectively with the calibration coefficients earlier obtained, so as to determine the applied stress in the model.

6.1. Relieved Strains

Several experimental tests (described in section 4.2) were carried out on identical specimens (Figure 4.2) with known properties (Table 4.1). Three tests that were performed with a diameter of the hole approximately equal to 1.80 mm will be following presented and analysed. The values of the relaxed strain, measured as a function of depth and obtained in the present work in the three tests performed, are presented in Figure 6.1, Figure 6.2 and Figure 6.3.

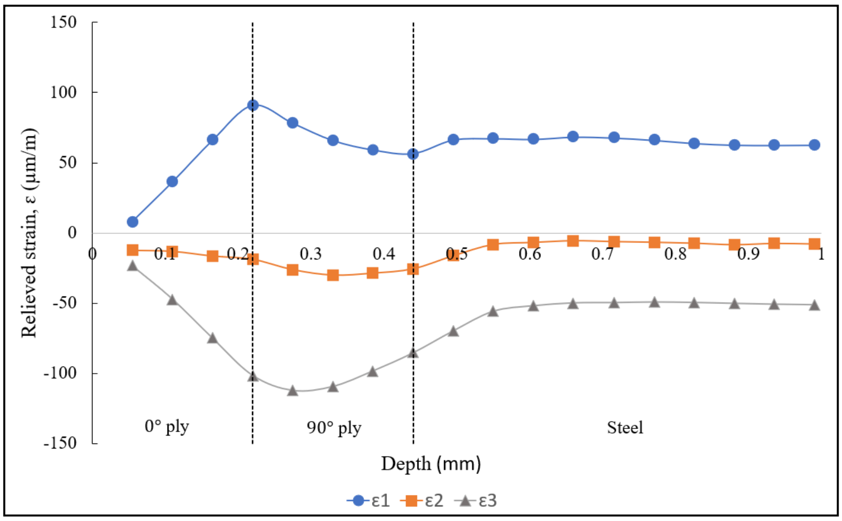

Figure 6.1. Sample 1 - Graph evolution of relieved strains ε_1, ε_2 and ε_3 along depth.

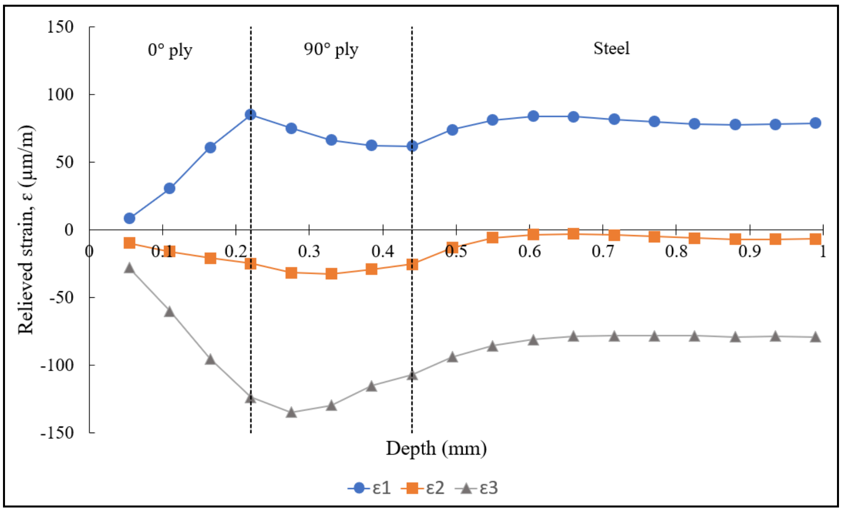

Figure 6.2. Sample 2 - Graph evolution of relieved strains $\boldsymbol{\varepsilon_1}$, $\boldsymbol{\varepsilon_2}$ and $\boldsymbol{\varepsilon_3}$ along depth.

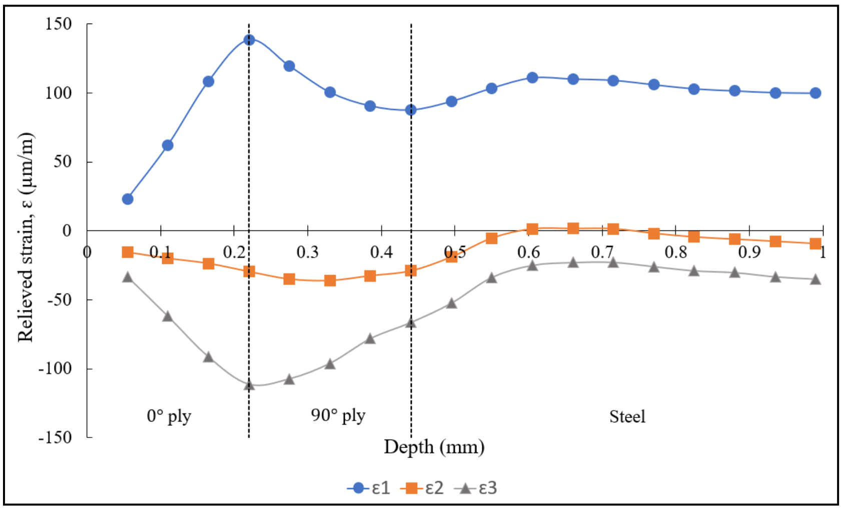

Figure 6.3. Sample 3 - Graph evolution of relieved strains $\boldsymbol{\varepsilon_1}$, $\boldsymbol{\varepsilon_2}$ and $\boldsymbol{\varepsilon_3}$ along depth.

All three samples present similar behaviour in evolution of the three relieved strains in depth and the range of values for all samples is roughly the same. While relieved strains data read by strain gauge with direction of x axis (ε_1) have positive values, relieved strains obtained by strain gauges with direction of y axis (ε_3) and direction of 45° (ε_2) present negative values. The values of strain gauge ε_2 are very close to zero. Finally, it is possible to identify a visible inversion in the slope of the strain relaxation curves, which clearly indicates the discontinuity induced at layers interface (different properties).

6.2. Residual Stresses

The residual stresses were determined by the iterative calculation method described in chapter 3, using the software developed. For each sample, it was possible to obtain three graphics corresponding to the in-plane residual stress (σ_x, σ_y and τ_{xy}) presented in the material. All the obtained residual stresses for the three samples are shown in Figure 6.4 to Figure 6.12, where the residual stresses are in function of depth, and presented at the centre of each depth increment. The trend line of each dot group is displayed with the same colour as the dots. The graphics corresponding to the same type of residual stress are presented in groups so that the results of the various samples can be compared.

Starting by comparing the graphics corresponding to the same type of residual stress but obtained in different samples, it is possible to verify a certain similarity on the residual stress distribution observed for the three samples, especially for the cases of longitudinal (x) and transverse (y) residual stress – according to Figure 4.3. While within each layer the residual stress follows a certain behaviour, it can be observed (in all graphics) a clear discontinuity at layers interface of the material. Thus, it is feasible to make an easy distinction between the 0° oriented ply, 90° oriented ply and steel alloy by the observed points. For the case of longitudinal residual stress, the first layer presents compressive stress, while the second layer mostly presents tensile stress. In the steel layer there are both compressive and tensile stresses as the values are more vertically spread compared to the other layers. For the graphics corresponding to transverse residual stress, the 0° ply has tensile stress, while 90° ply presents compressive stress. The behaviour in the steel ply is similar to the one observed for the case of longitudinal residual stress. Finally, in the case of shear residual stress, there is a greater observed difference between samples but the stress values are much lower for this specific case. It is important to note that for transverse fibres, i.e., oriented at 90°, the resistance is low, so high values of residual stress for this orientation can mean higher values than the real ones. This can occur if there is a delamination during IHD tests. Also, the transverse residual stress in fibres reach values above 50 MPa in tension which, combining with stress concentration around the hole, can lead to transverse cracking.

Residual longitudinal stress (σ_x) as a function of depth for all samples:

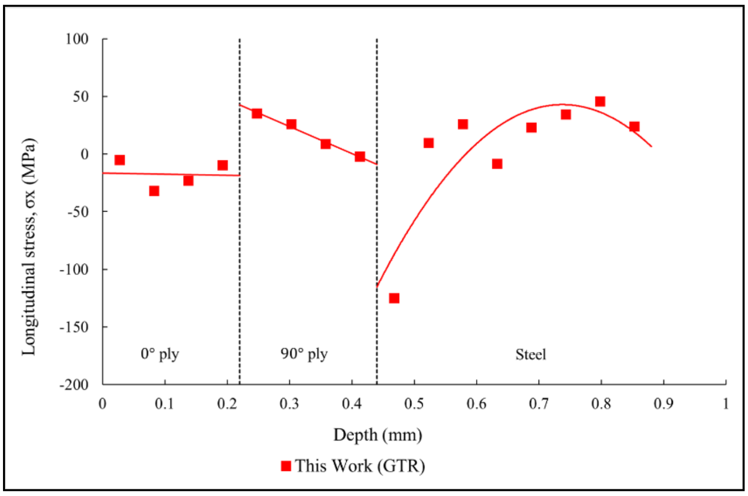

Figure 6.4. Sample 1 - Residual longitudinal stress (σ_x) as a function of depth.

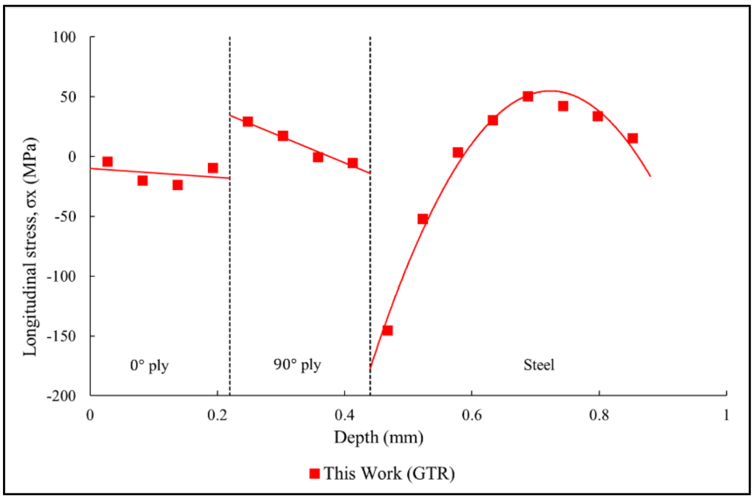

Figure 6.5. Sample 2 - Residual longitudinal stress (σ_x) as a function of depth.

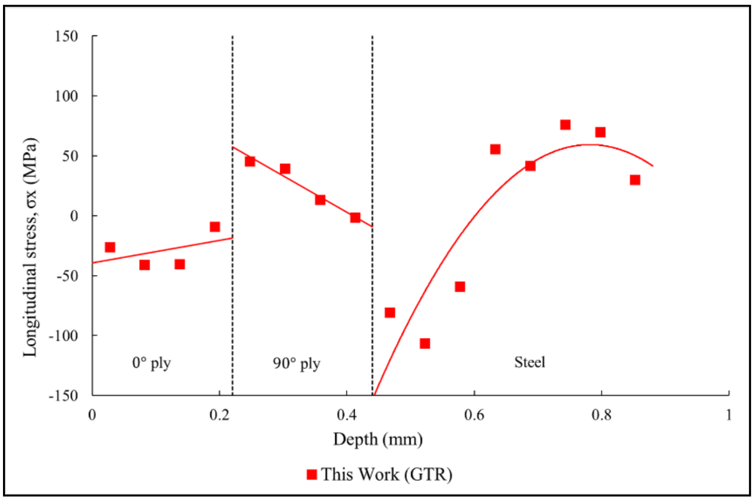

Figure 6.6. Sample 3 - Residual longitudinal stress (σ_x) as a function of depth.

Residual transverse stress (σ_y) as a function of depth for all samples:

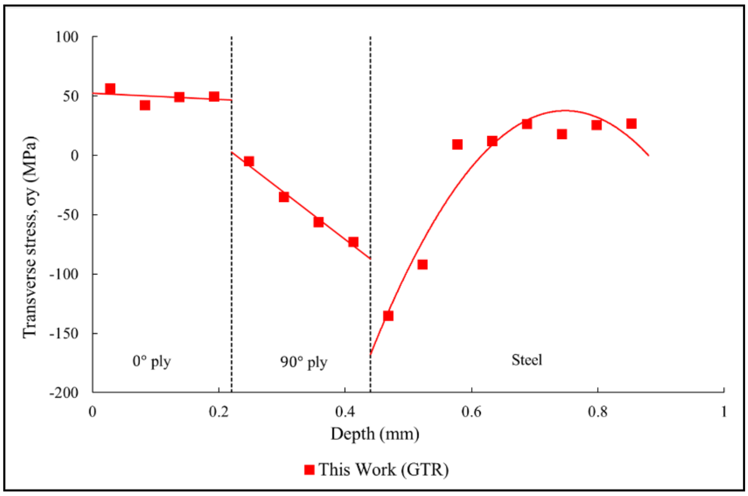

Figure 6.7. Sample 1 - Residual transverse stress (σ_y) as a function of depth.

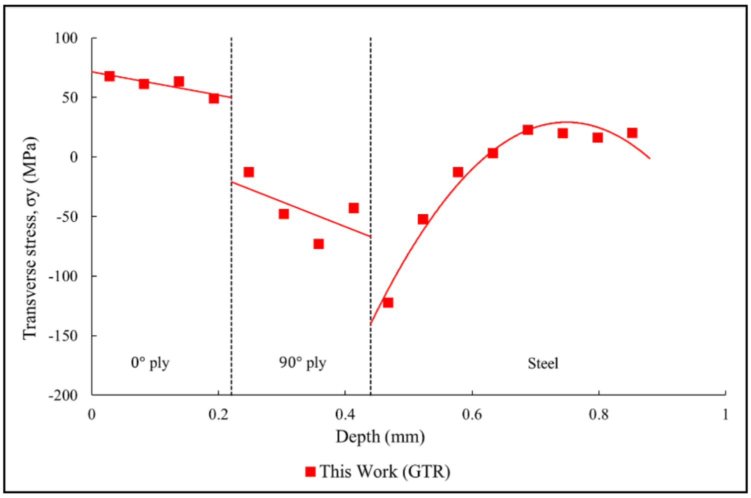

Figure 6.8. Sample 2 - Residual transverse stress (σ_y) as a function of depth.

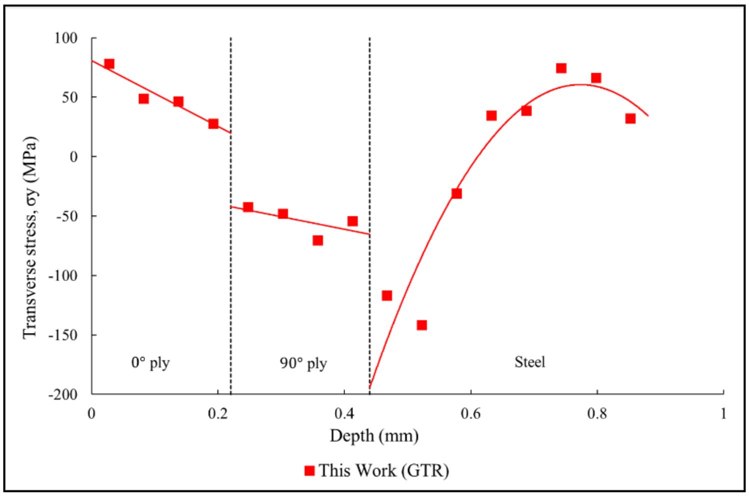

Figure 6.9. Sample 3 - Residual transverse stress (σ_y) as a function of depth.

Residual shear stress (τ_{xy}) as a function of depth for all samples:

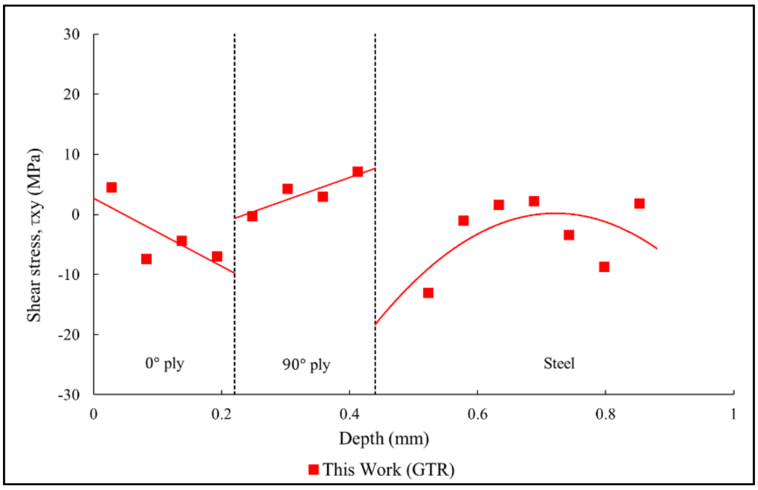

Figure 6.10. Sample 1 - Residual shear stress (τ_{xy}) as a function of depth.

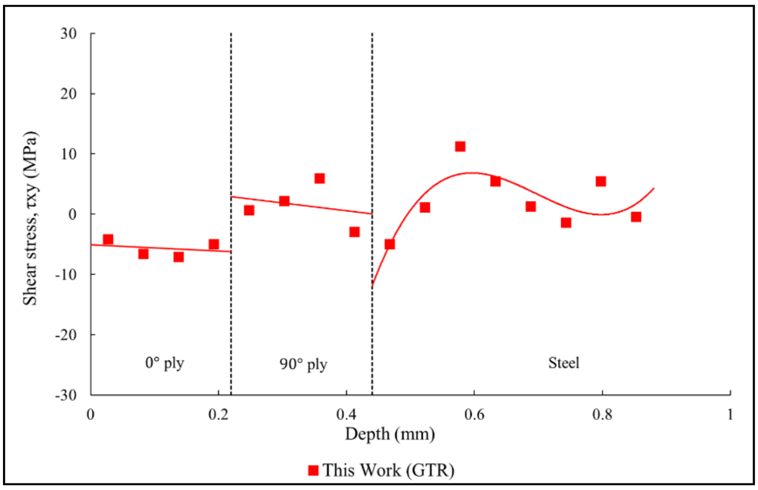

Figure 6.11. Sample 2 - Residual shear stress (τ_{xy}) as a function of depth.

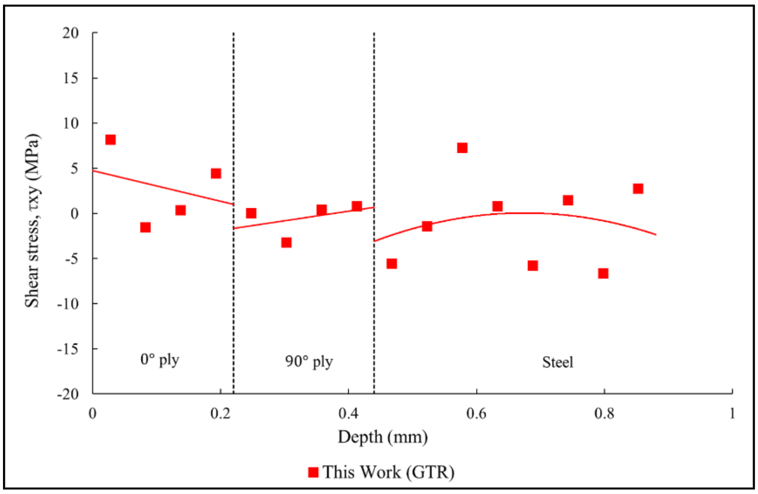

Figure 6.12. Sample 3 - Residual shear stress (τ_{xy}) as a function of depth.

6.3. Discussion

The residual stress values obtained in this work were compared with the work carried out by a South African partner (Wits University), who used NASTRAN code (FEM) to achieve calibration coefficients and the integral method using Tikhonov regularization to calculate residual stress values. The results were also compared with the neutron diffraction method, but only for steel layer since this method cannot be used to determine stresses in FRP due to lack of crystallinity in them. Figure 6.13 to Figure 6.21 compare the results obtained in this work with the results obtained by Wits University (Tikhonov regularization) and by NECSA (neutron diffraction method).

There is a good agreement between the values obtained in this work and those obtained by the partners in the first two layers. However, as expected, it is noted that as the depth increment increases, it is possible to observe some scattering in the steel alloy ply and, therefore, a slight difference between the results. Overall, by comparing the results obtained in this study with the partner values, there is a good agreement between them (especially in fibre layers). Comparing the results with neutron diffraction, regarding the longitudinal and transverse residual stress, there still is a good agreement, even though, unfortunately, neutron diffraction is not able to provide residual stresses near the GFRP/steel interface. The residual stress obtained refers to half the thickness of the samples. Since we are working with symmetrical samples, the existence of symmetry in the values of residual stresses along thickness is expected.

Residual stress (σ_x, σ_y, τ_{xy}) as a function of depth for sample 1:

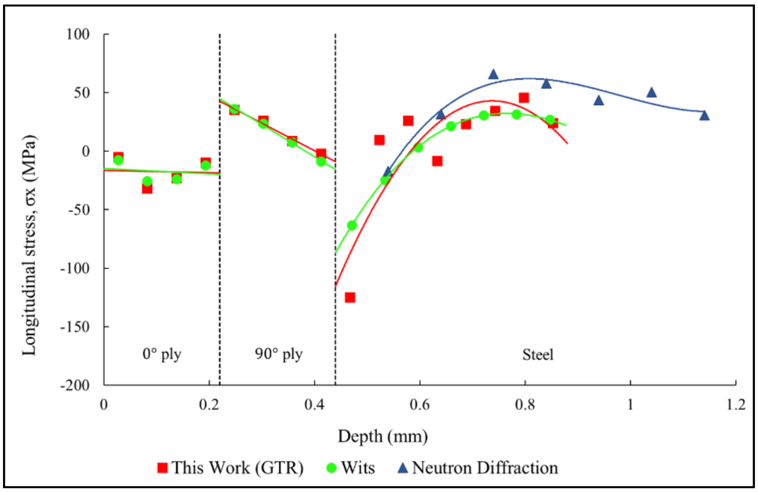

Figure 6.13. Sample 1 - Residual longitudinal stress ($\boldsymbol{\sigma_x}$) as a function of depth.

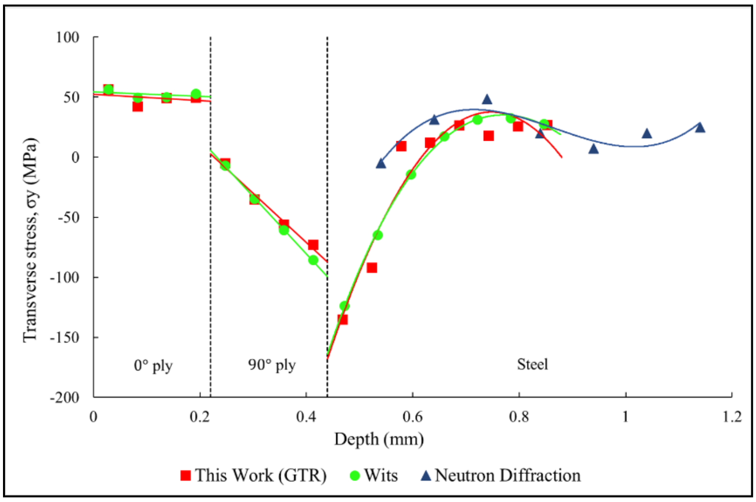

Figure 6.14. Sample 1 - Residual transverse stress ($\boldsymbol{\sigma_y}$) as a function of depth.

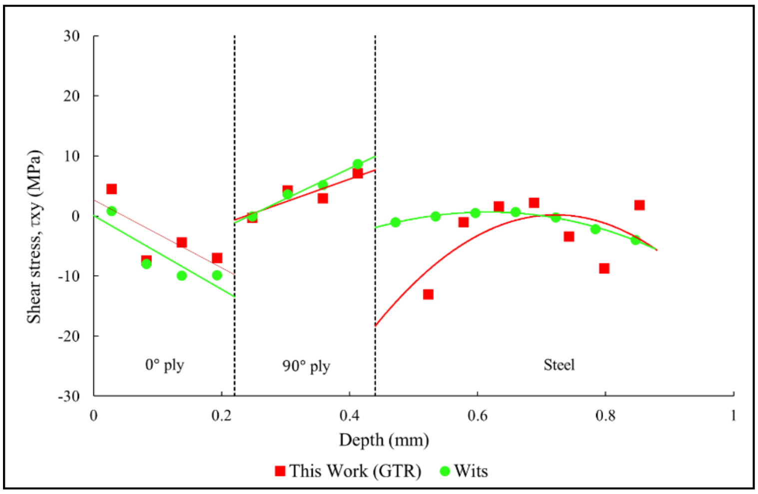

Figure 6.15. Sample 1 - Residual shear stress ($\boldsymbol{\tau_{xy}}$) as a function of depth.

Residual stress (σ_x, σ_y, τ_{xy}) as a function of depth for sample 2:

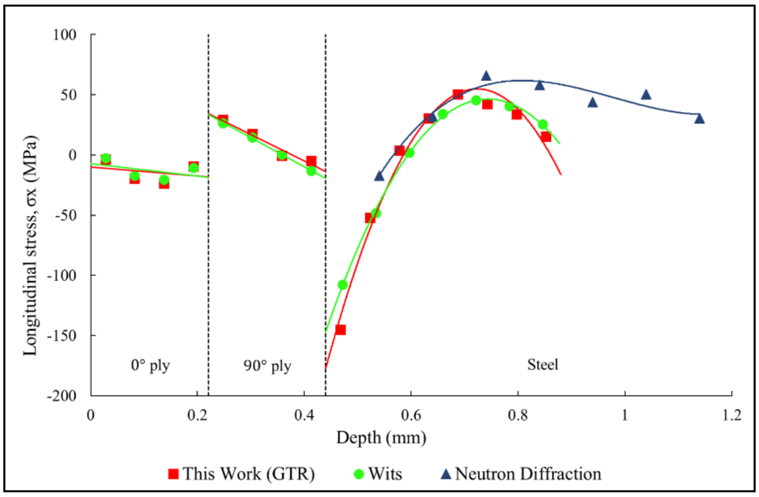

Figure 6.16. Sample 2 - Residual longitudinal stress (σ_x) as a function of depth.

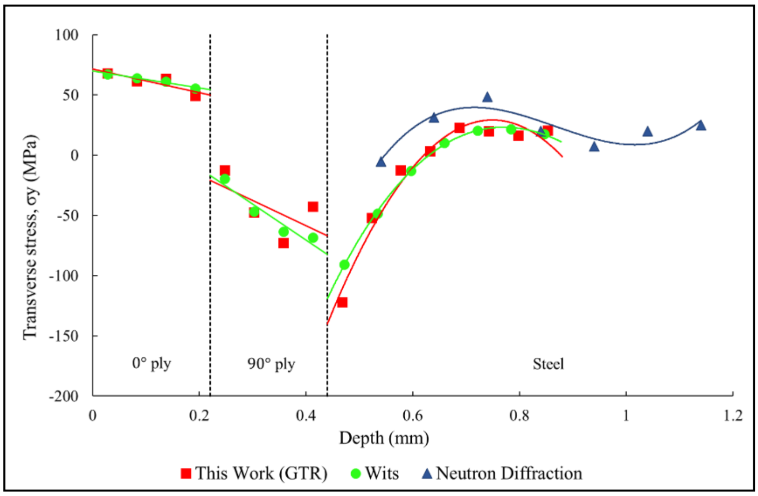

Figure 6.17. Sample 2 - Residual transverse stress (σ_y) as a function of depth.

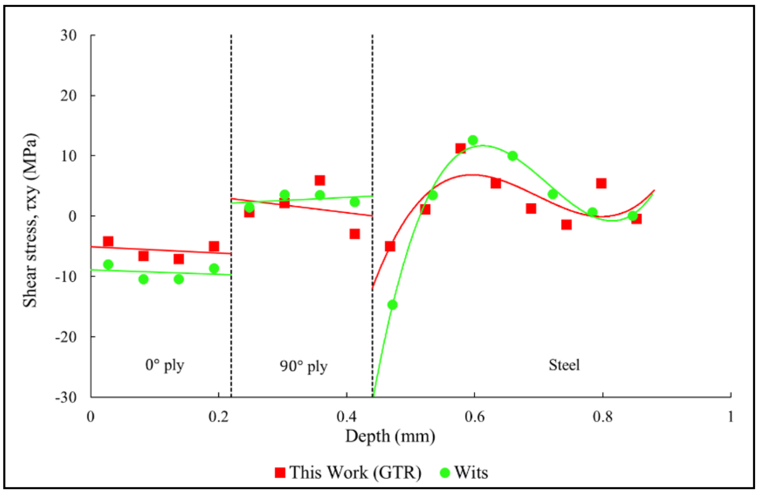

Figure 6.18. Sample 2 - Residual shear stress (τ_{xy}) as a function of depth.

Residual stress (σ_x, σ_y, τ_{xy}) as a function of depth for sample 3:

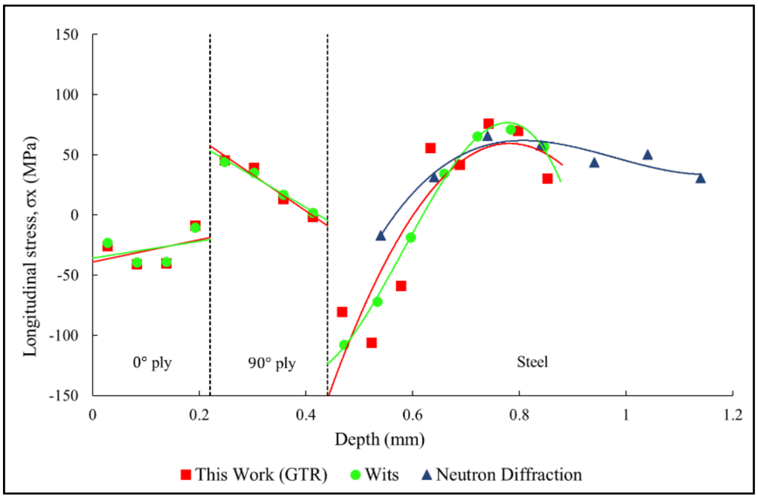

Figure 6.19. Sample 3 - Residual longitudinal stress ($\boldsymbol{\sigma_x}$) as a function of depth.

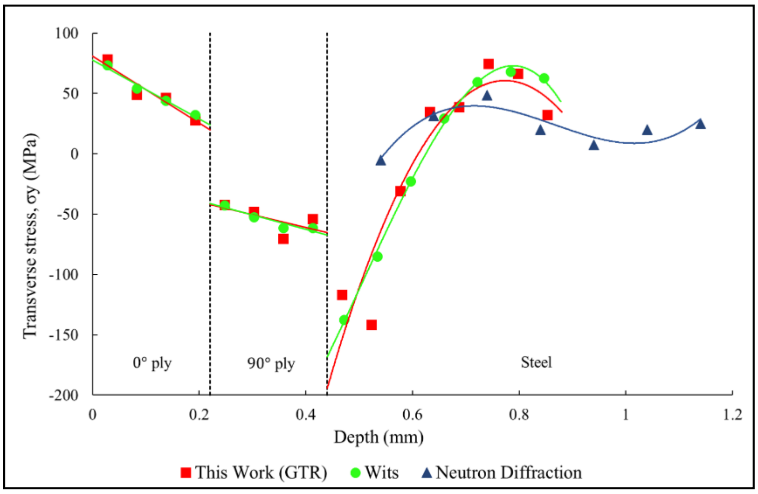

Figure 6.20. Sample 3 - Residual transverse stress ($\boldsymbol{\sigma_y}$) as a function of depth.

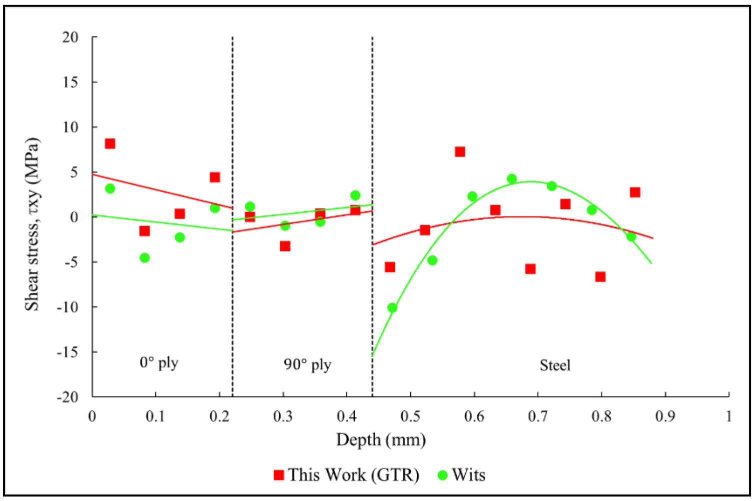

Figure 6.21. Sample 3 - Residual shear stress ($\boldsymbol{\tau_{xy}}$) as a function of depth.

6.3.1. Numerical Simulation of an Externally Applied Uniform Stress

For a better assessment of the determination of residual stresses using IHD in FMLs, an additional FEM simulation in ANSYS was performed. An axial and uniform stress of 15 MPa, corresponding to a 700 N tensile load, was externally applied to the sample (simulating a tensile test). While the model was subjected to this uniform axial external stress, the simulation of the IHD method was carried out, to determine the curves of strain relaxation vs. hole depth. These curves were then used with the integral method developed in this thesis to verify the ability of the method to determine a well-known externally applied uniform stress. Figure 6.22 shows the finite element model created in ANSYS. Note that the ASTM rosettes used for this simulation are of type A (Figure 2.14) and, therefore, the grids in the Figure 6.22 are not superimposed since the 2nd strain gauge is physically at 135º of the strain gauge 1. However, since the FML sample and the stacking ply configuration enable symmetry, a quarter model was used instead and, therefore, strain relaxation corresponding to the strain gauge 2 was determined in the first quadrant as well.

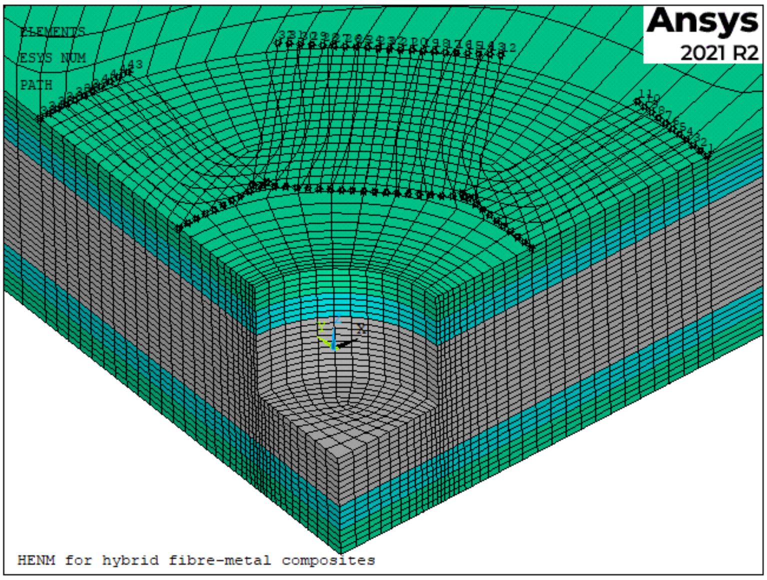

Figure 6.22. ANSYS FEM mesh for simulation of tensile calibration tests.

The stresses determined by the method developed in this thesis are shown in Figure 6.23 as well as the externally applied uniform stress of 15 MPa (continuous black line). It can be seen a stress redistribution in each layer since the material properties through thickness are not the same. The stress redistribution can be analytically determined using the classical theory of laminates (CLT) [70]. This work is underway at moment and was not possible to present the results in this thesis. However, it is possible to observe that the stresses in the GFRP are linear, as expected, but much lower than the external average stress of 15 MPa applied, in particular for the fibres at 90º. In the steel layer, the stresses approach 20.9 MPa (average value) and present a slight variation through this layer. Without be a definitive conclusion, since it is yet necessary to calculate the redistribution of stresses by each layer, the results shown in Figure 6.23 seem to also indicate that the integral method developed in this thesis can be used to determine residual stresses using the incremental hole drilling technique.

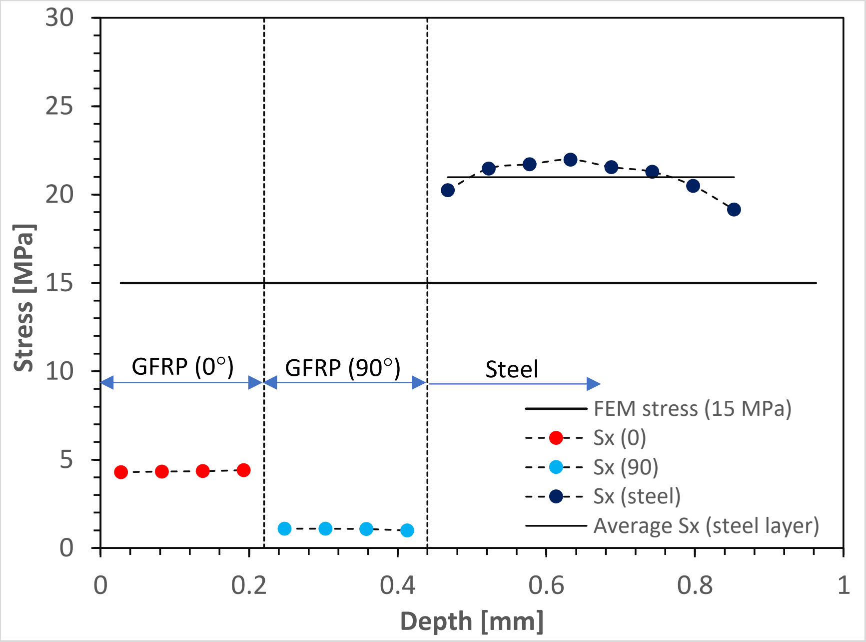

Figure 6.23. Longitudinal stress (σ_x) redistribution through the FML layers due to an externally simulated uniform stress of 15 MPa.

7. CONCLUSIONS AND RECOMMENDATION FOR FUTURE WORK

The main objective of this work was to determine residual stresses in GFRP/Steel samples by the incremental hole-drilling technique (IHD) and verify the validity of the results obtained, contributing to the development of the IHD method. IHD has been developed for anisotropic and layered materials during the past two decades, due to the complexity of the mechanical behaviour of this kind of materials and the inverse problem usually involved for the determination of residual stresses using mechanical methods, such as IHD.

In this work, a methodology for the determination of residual stresses in anisotropic and layered materials was developed using IHD integral method, based on numerical simulation and calculations performed using Python. The results obtained allowed to conclude that the IHD technique can be used for measuring non-uniform residual stresses in FMLs. The residual stress determined from the method used agrees well with the results obtained by other techniques and methods. There was some visible scattering in the residual stress results in the deeper layers, but it does not compromise the reliability of the results. It was possible to observe a discontinuity of the residual stress results at layers' interfaces. Thus, there is a clear identification of the interface layers between the fibres and fibres/metal due the change in behaviour (singularities) of the determined residual stress. There are almost no published studies showing this behaviour in FML composites.

For a future work, since the results obtained presented a slight scattering in deeper layers (steel layers) and once the Tikhonov regularization is a recognized method for having the effect of smoothing the stress results, it would be a good alternative to implement this method in the future, to further contribute to the development of the IHD and its application to FMLs and composite laminates in general. Also, since it is possible to analytically determine the stress redistribution in the FML material, a good idea for a future work would be to perform experimental tensile tests, applying a well-known external uniform stress (calibration stress) during IHD, once the calculation of stress redistribution through the composite laminate plies can be evaluated using the CLT. In this way, a better assessment of the residual stresses determined by IHD in FML samples could be carried out, complementing the started study presented in section 6.3.1. These experimental tests can also allow to analyse other possible error source, such as those related with the thermomechanical effects of the cutting procedure during the drilling operation.

BIBLIOGRAPHY

[1] Z. Ding, H. Wang, J. Luo, N. Li, A review on forming technologies of fibre metal laminates, Int. J. Light. Mater. Manuf. 4 (2021) 110–126. https://doi.org/10.1016/J.IJLMM.2020.06.006.

[2] A. Vlot, Glare: History of the Development of a New Aircraft Material, 2001. https://doi.org/10.1007/0-306-48398-X.

[3] A.P. Mouritz, ed., Metal matrix, fibre–metal and ceramic matrix composites for aerospace applications, in: Introd. to Aerosp. Mater., Woodhead Publishing, 2012: pp. 394–410. https://doi.org/10.1533/9780857095152.394.

[4] V. V. Vasiliev, E. V. Morozov, eds., Mechanics of Laminates, in: Adv. Mech. Compos. Mater. Struct., 4th ed., Elsevier, 2018: pp. 191–242. https://doi.org/10.1016/B978-0-08-102209-2.00003-7.

[5] A. Asundi, A.Y.N. Choi, Fiber metal laminates: An advanced material for future aircraft, J. Mater. Process. Technol. 63 (1997) 384–394. https://doi.org/10.1016/S0924-0136(96)02652-0.

[6] The Guardian, https://www.theguardian.com/international, K. West, Midair collisions to metal fatigue: tragedies that changed air travel (2019), accessed on 14/04/2021.

[7] W. He, L. Wang, H. Liu, C. Wang, L. Yao, Q. Li, G. Sun, On impact behavior of fiber metal laminate (FML) structures: A state-of-the-art review, Thin-Walled Struct. 167 (2021) 108026. https://doi.org/10.1016/j.tws.2021.108026.

[8] A.C. Long, M.J. Clifford, Composite Forming Mechanisms and Materials Characterisation, in: A.C. Long (Ed.), Compos. Form. Technol., 2007: pp. 1–21. https://doi.org/10.1533/9781845692537.1.

[9] E. Armentani, R. Citarella, R. Sepe, FML full scale aeronautic panel under multiaxial fatigue: Experimental test and DBEM Simulation, Eng. Fract. Mech. 78 (2011) 1717–1728. https://doi.org/10.1016/j.engfracmech.2011.02.020.

[10] G.S. Langdon, Z. Guan, W.J. Cantwell, Blast Protection for Polymer Composite

Materials in Structures Subjected to Air-Blast Loading, in: P.W.R. Beaumont, C.H. Zweben (Eds.), Compr. Compos. Mater. II, Elsevier, 2018: pp. 332–350. https://doi.org/10.1016/B978-0-12-803581-8.10067-0.

[11] C.T. Lin, P.W. Kao, F.S. Yang, Fatigue behaviour of carbon fibre-reinforced aluminium laminates, Composites. 22 (1991) 135–141. https://doi.org/10.1016/0010-4361(91)90672-4.

[12] K. Blohowiak, R. Anderson, W. Grace, J. Grob, D. Fry, Development of New Thin Adhesive Systems and Test Methods for TiGr Laminates, in: Sampe J., Long Beach, USA, 2008.

[13] A. Brot, Development of Fatigue Life Regulations Based on Lessons, in: Proc. 46th Isr. Annu. Conf. Aerosp. Sci., 2006.

[14] AIRBUS, https://www.airbus.com/en, acessed on 21/04/2021.

[15] M. Gude, Accelerating electric transport Vehicles of the future, Int. Innov. (2014) 83–85.

[16] P. Jakubczak, B. Surowska, J. Bieniaś, Evaluation of force-time changes during impact of hybrid laminates made of titanium and fibrous composite, Arch. Metall. Mater. 61 (2016) 689–693. https://doi.org/10.1515/amm-2016-0117.

[17] D.K. Rajak, D.D. Pagar, P.L. Menezes, E. Linul, Fiber-reinforced polymer composites: Manufacturing, properties, and applications, Polymers (Basel). 11 (2019). https://doi.org/10.3390/polym11101667.

[18] A.R.A. Talib, I. Mohammed, Synthetic/natural fiber properties of fire-designated zone of an aircraft engine: A structural health monitoring approach, in: M. Jawaid, M. Thariq, N. Saba (Eds.), Struct. Heal. Monit. Biocomposites, Fibre-Reinforced Compos. Hybrid Compos., Woodhead Publishing, 2019: pp. 153–190. https://doi.org/10.1016/B978-0-08-102291-7.00009-5.

[19] A. Salve, R. Kulkarni, A. Mache, A Review: Fiber Metal Laminates (FML's) - Manufacturing, Test methods and Numerical modeling, Int. J. Eng. Technol. Sci. 3 (2016) 71–84. https://doi.org/10.15282/ijets.6.2016.1.10.1060.

[20] T. Sinmazçelik, E. Avcu, M.Ö. Bora, O. Çoban, A review: Fibre metal laminates, background, bonding types and applied test methods, Mater. Des. 32 (2011) 3671–3685. https://doi.org/10.1016/j.matdes.2011.03.011.

[21] P.J. Withers, H.K.D.H. Bhadeshia, Residual stress part 1 - Measurement techniques,

Mater. Sci. Technol. 17 (2001) 355–365. https://doi.org/10.1179/026708301101509980.

[22] A. Magnier, B. Scholtes, T. Niendorf, On the reliability of residual stress measurements in polycarbonate samples by the hole drilling method, Polym. Test. 71 (2018) 329–334. https://doi.org/10.1016/j.polymertesting.2018.09.024.

[23] J. Hausmann, P. Naghipour, K. Schulze, Analytical and Numerical Residual Stress Models for Fiber Metal Laminates – Comparison and Application, Procedia Mater. Sci. 2 (2013) 68–73. https://doi.org/10.1016/j.mspro.2013.02.009.

[24] T. Wu, S.R. Tinkloh, T. Tröster, W. Zinn, T. Niendorf, Determination and Validation of Residual Stresses in CFRP/Metal Hybrid Components Using the Incremental Hole Drilling Method, J. Compos. Sci. 4 (2020) 143. https://doi.org/10.3390/jcs4030143.

[25] D. Walker, Residual stress measurement techniques, Adv. Mater. Process. 159 (2001) 30–33.

[26] A. Tircuit, B. Belkhouche, Object-oriented behavioral testing through trace generation, Proc. Annu. Southeast Conf. 2 (2005) 2306–2310. https://doi.org/10.1145/1167253.1167320.

[27] M.J. Park, H.N. Yang, D.Y. Jang, J.S. Kim, T.E. Jin, Residual stress measurement on welded specimen by neutron diffraction, J. Mater. Process. Technol. 155–156 (2004) 1171–1177. https://doi.org/10.1016/j.jmatprotec.2004.04.393.

[28] ASTM E837-20, Standard Test Method for Determining Residual Stresses by the Hole-Drilling Strain-Gage Method, in: ASTM International, West Conshohocken, PA, 2020. https://doi.org/10.1520/E0837-20.

[29] M. Scafidi, M. Beghini, L. Bertoni, C. Santus, The hole-drilling strain gauge method for the measurement of uniform or non-uniform residual stresses, (2016).

[30] M. Bijak-Zochowski, A Semidestructive Method of Measuring Residual Stresses, in: Exp. Stress Anal., VDI-Berichte, 1978: pp. 469–476.

[31] SINT Technology, https://www.residualstressmeasurement.com/, accessed on: 06/05/2021.

[32] R.S. Fundamentals, H. Method, Measurement of Residual Stresses by the Hole-Drilling Strain Gage Method, (2010).

[33] Vishay Precision Group, Milling Guide for Residual Stress Measurements, Micro-

Measurements. (2011) 62–64.

[34] X. Liu, X. Wang, Z. Guan, T. Jiang, K. Geng, Z. Li, Improvement and validation of residual stress measurement in composite laminates using the incremental hole-drilling method, Mech. Mater. 154 (2021) 103715. https://doi.org/10.1016/j.mechmat.2020.103715.

[35] G.. Schajer, Stress Calculation Error Analysis for Incremental Hole-Drilling Residual Stress Measurements, in: Eng. Mater. Technol., 1996: pp. 120–126.

[36] J.P. Nobre, C. Polese, S.N. van Staden, Incremental Hole Drilling Residual Stress Measurement in Thin Aluminum Alloy Plates Subjected to Laser Shock Peening, Exp. Mech. 60 (2020) 553–564. https://doi.org/10.1007/s11340-020-00586-5.

[37] G.S. Schajer, L. Yang, Residual-stress measurement in orthotropic materials using the hole-drilling method, Exp. Mech. 34 (1994) 324–333. https://doi.org/10.1007/BF02325147.

[38] G.S. Schajer, P.S. Whitehead, Hole-Drilling Method for Measuring Residual Stresses, Synth. SEM Lect. Exp. Mech. (2018) 186. https://doi.org/10.2200/S00818ED1V01Y201712SEM001.

[39] S. for E. Mechanics, Handbook of Measurement of Residual Stresses, in: J. Lu (Ed.), Bethel, 1996: pp. 5-34 / 71-131.

[40] J. Mathar, Determination of initial stresses by measuring the deformation around drilled holes, Trans. ASME. 56 (1934) 249–254.

[41] W. Soete, R. Van Crombrugge, An industrial method for the determination of residual stresses, in: Proc. SESA, XVIII (1), 1950: pp. 17–28.

[42] K.P. Milbradt, Ring-method determination of residual stresses, in: Proc. SESA Spring Meet., Cleveland, 1951: pp. 63–74.

[43] R. Gunnert, Method for Measuring tri-axial residual stresses, in: Doc. IIW X-184-57-OE. Comm. X Int. Inst. Weld., 1958.

[44] R.A. Kelsey, Measuring Non-uniform Residual Stresses by the Hole-drilling Method, in: Proc. SESA XIV, 1956: pp. 181–194.

[45] A. Magnier, T. Wu, S.R. Tinkloh, T. Tröster, B. Scholtes, T. Niendorf, On the reliability of residual stress measurements in unidirectional carbon fibre reinforced epoxy composites, Polym. Test. 97 (2021). https://doi.org/10.1016/j.polymertesting.2021.107146.

[46] E.M. Beaney, E. Procter, A Critical evaluation of the centre hole technique for the measurement of residual stresses, 10 (1974) 7–14. https://doi.org/10.1111/j.1475-1305.1974.tb00074.x.

[47] G.S. Schajer, Application of Finite Element Calculations to Residual Stress Measurements, ASME J. Eng. Mater. Technol. 103 (1981) 157–163.

[48] M.T. Flaman, Brief investigation of induced drilling stresses in the center-hole method of residual-stress measurement, Exp. Mech. 22 (1982) 26–30. https://doi.org/10.1007/BF02325700.

[49] W. Zhu, D. Smith, Development of the Incremental Hole Drilling Method for Measuring Residual Stresses in Components with Curved Surfaces, (1994).

[50] M. Tootoonian, G.S. Schajer, Enhanced sensitivity residual-stress measurements using taper-hole drilling, Exp. Mech. 35 (1995) 124–129. https://doi.org/10.1007/BF02326469.

[51] O. Sicot, X.L. Gong, A. Cherouat, J. Lu, Determination of residual stress in composite laminates using the incremental hole-drilling method, J. Compos. Mater. 37 (2003) 831–844. https://doi.org/10.1177/002199803031057.

[52] O. Sicot, X.L. Gong, A. Cherouat, J. Lu, Influence of experimental parameters on determination of residual stress using the incremental hole-drilling method, Compos. Sci. Technol. 64 (2004) 171–180. https://doi.org/10.1016/S0266-3538(03)00278-1.

[53] P. Pagliaro, B. Zuccarello, Residual stress analysis of orthotropic materials by the through-hole drilling method, Exp. Mech. 47 (2007) 217–236. https://doi.org/10.1007/s11340-006-9019-3.

[54] J.P. Nobre, J.-H. Stiffel, A. Nau, J.C. Outeiro, A. Castanhola Batista, W. Van Paepegem, B. Scholtes, Induced drilling strains in glass fibre reinforced epoxy composites, CIRP Ann. - Manuf. Technol. 62 (2013) 87–90. https://doi.org/10.1016/j.cirp.2013.03.089.

[55] T.C. Smit, R.G. Reid, Residual Stress Measurement in Composite Laminates Using Incremental Hole-Drilling with Power Series, Exp. Mech. 58 (2018) 1221–1235. https://doi.org/10.1007/s11340-018-0403-6.

[56] T.C. Smit, R.G. Reid, Tikhonov regularization with Incremental Hole-Drilling and the Integral Method in Cross-Ply Composite Laminates, Exp. Mech. 60 (2020)

1135–1148. https://doi.org/10.1007/s11340-020-00629-x.

[57] M.M. Shokrieh, A.R. Ghasemi K., Determination of calibration factors of the hole drilling method for orthotropic composites using an exact solution, J. Compos. Mater. 41 (2007) 2293–2311. https://doi.org/10.1177/0021998307075443.

[58] A.R. Ghasemi, M.M. Mohammadi, Residual stress measurement of fiber metal laminates using incremental hole-drilling technique in consideration of the integral method, Int. J. Mech. Sci. 114 (2016) 246–256. https://doi.org/10.1016/j.ijmecsci.2016.05.025.

[59] ASTM E837-13a, Standard Test Method for Determining Residual Stresses by the Hole-Drilling Strain-Gage Method, Stand. Test Method E837-13a. i (2013) 1–16. https://doi.org/10.1520/E0837-13A.2.

[60] G.S. Schajer, Hole-drilling residual stress profiling with automated smoothing, J. Eng. Mater. Technol. Trans. ASME. 129 (2007) 440–445. https://doi.org/10.1115/1.2744416.

[61] G.S. Schajer, Measurement of non-uniform residual stresses using the hole drilling method - part I: Stress calculation procedure, Am. Soc. Mech. Eng. Mater. Div. MD. 7 (1988) 85–91.

[62] G.S. Schajer, Use of displacement data to calculate strain gauge response in non-uniform strain fields, Strain. 29 (1993) 9–13. https://doi.org/10.1111/j.1475-1305.1993.tb00820.x.

[63] S. Akbari, F. Taheri-Behrooz, M.M. Shokrieh, Characterization of residual stresses in a thin-walled filament wound carbon/epoxy ring using incremental hole drilling method, Compos. Sci. Technol. 94 (2014) 8–15. https://doi.org/10.1016/j.compscitech.2014.01.008.

[64] G.S. Schajer, M.B. Prime, Use of inverse solutions for residual stress measurements, J. Eng. Mater. Technol. Trans. ASME. 128 (2006) 375–382. https://doi.org/10.1115/1.2204952.

[65] A.N. Tikhonov, A. V. Goncharsky, V. V. Stepanov, A.G. Yagola, Numerical Methods for the Solution of Ill-Posed Problems, Mathematics and Its Applications, 1995.

[66] HBM, https://www.hbm.com/pt/, accessed on: 07/06/2021.

[67] P. V Grant, J.D. Lord, P. Whitehead, The Measurement of Residual Stresses by the

Incremental Hole Drilling Technique, Meas. Good Pract. Guid. No. 53 - Issue 2. (2006) 63.

[68] M. T. Hutchings, Measurement of residual and applied stress using neutron diffraction, Springer Science & Business Media, 1992.

[69] A.M. Venter, P.R. Van Heerden, D. Marais, J.C. Raaths, Physica B : Condensed Matter MPISI : The neutron strain scanner materials probe for internal strain investigations at the SAFARI-1 research reactor, Phys. B Phys. Condens. Matter. 551 (2018) 417–421. https://doi.org/10.1016/j.physb.2017.12.011.

[70] A.T. Nettles, Basic Mechanics of Laminated Composite Plates, NASA Ref. Publ. 1351. (1994).

ANNEX A – PYTHON SCRIPT DEVELOPED

The script below was developed in order to solve the system of matrix equations presented by the integral method – see Chapter 3.

```
import numpy as np


def read_matrix_in_line(file_path):
    with open (file_path, 'r') as file:
        #Read all lines of the file (arrays)
        #Assume the file has only one matrix and its inline
        matrix = file.readlines()[0]

        #Transforms a string with an array into an array whose rows are numpy arrays
        new_mat = [np.array([float(b) for b in a.replace(']', '').split(',')]) for a in matrix.replace('[', '').split('], ')]

    return new_mat


#Cij matrices must be written in format, for example: [[-4.8902, 0, 0], [-5.0561, -5.2645, 0], [-5.0564, -5.2566, -5.1801]]
#Denote that in this case there are 3 increments, resulting in a 3x3 matrix
#Put the matrices in separate files, named C11, C12, C13, etc.
#Need to indicate de Path File

c11 = read_matrix_in_line('C:\Users\Utilizador\Desktop\CoefFinais\C11.txt')
c12 = read_matrix_in_line('C:\Users\Utilizador\Desktop\CoefFinais\C12.txt')
c13 = read_matrix_in_line('C:\Users\Utilizador\Desktop\CoefFinais\C13.txt')
c21 = read_matrix_in_line('C:\Users\Utilizador\Desktop\CoefFinais\C21.txt')
```

```
c22 = read_matrix_in_line('C:\Users\Utilizador\Desktop\CoefFinais\C22.txt')
c23 = read_matrix_in_line('C:\Users\Utilizador\Desktop\CoefFinais\C23.txt')
c31 = read_matrix_in_line('C:\Users\Utilizador\Desktop\CoefFinais\C31.txt')
c32 = read_matrix_in_line('C:\Users\Utilizador\Desktop\CoefFinais\C32.txt')
c33 = read_matrix_in_line('C:\Users\Utilizador\Desktop\CoefFinais\C33.txt')

A = [[c11, c12, c13], [c21, c22,c23], [c31, c32, c33]]

#In Excel (strain relaxation values), you cannot write in the first line as this is for column labels
#Need to indicate de Path File

with open('/Users/Utilizador/Desktop/CoefFinais/Deformation_Values.csv', 'r') as file:
    #Read the file
    #Skip teh first row ([1:]) because the first row has the column labels
    lines = file.readlines()[1: ]
    #Form the lines, create the vector of vectors
    strain = [np.array([float(value) for value in line.split(";")]) for line in lines]
    print(strain)

def build_new_A(A):
    new_A = []
    row_A = []
    matrix = []
    row = []
    dim = len(A[0][0])
    for c in range (dim):
        for d in range(dim):
            for a in range(3): #build a matrix
                for b in range(3): #build a line
                    row.append(A[a][b][c][d])
```

```
                matrix.append(row)
                row = []
            row_A.append(np.array(matrix))
            matrix = []
        new_A.append(row_A)
        row_A = []
    return new_A

def print_new_A(new_A):
    for i in range(len(new_A)):
        for e in range (len(new_A[0])):
            for j in range(3):
                print(new_A[i][e][j])
            print("-----------------------")
        print("###################")

#Strain = [np.array([x,xy,y]step1), np.array([x,xy,y]step2), np.array([x,xy,y]step3), np.array([x,xy,y]step4)]

def iterative_method(new_A, strain):
    stresses_dim = []
    dim = len(new_A)

    for i in range(dim):
        b = strain[i]
        if i > 0:
            for j in range(i):
                b = b - np.dot(new_A[i][j], stresses_dim[j])
        print(new_A[i][i])
        a = np.linalg.inv(new_A[i][i])
        result = np.dot(a, b)
        stresses_dim.append(result)
```

```
    return stresses_dim

new_A = build_new_A(A)
print_new_A(new_A)
stresses = iterative_method(new_A, strain)
print(stresses)
```

ANNEX B – SUB-MATRICES OF CALIBRATION COEFFICIENTS

The nine matrices (Equation (3.6)), obtained by FEM when simulating the IHD technique in ANSYS, are presented in the Tables below. All values were multiplied by 10^6.

Table 0.1. First 9 columns of matrix $\boldsymbol{C}^{11}$ obtained using the FEM (ANSYS).

	1	2	3	4	5	6	7	8	9
1	-0.61339	0.00000	0.00000	0.00000	0.00000	0.00000	0.00000	0.00000	0.00000
2	-0.76664	-0.66968	0.00000	0.00000	0.00000	0.00000	0.00000	0.00000	0.00000
3	-0.89150	-0.82282	-0.68784	0.00000	0.00000	0.00000	0.00000	0.00000	0.00000
4	-1.01105	-0.95288	-0.86307	-0.70803	0.00000	0.00000	0.00000	0.00000	0.00000
5	-1.06585	-1.00893	-0.92550	-0.80306	-0.57721	0.00000	0.00000	0.00000	0.00000
6	-1.10305	-1.04662	-0.96637	-0.85364	-0.68012	-0.44352	0.00000	0.00000	0.00000
7	-1.12828	-1.07220	-0.99362	-0.88582	-0.72578	-0.53713	-0.31986	0.00000	0.00000
8	-1.14184	-1.08580	-1.00783	-0.90194	-0.74686	-0.56851	-0.38647	-0.18647	0.00000
9	-1.15025	-1.09424	-1.01642	-0.91096	-0.75679	-0.58033	-0.40148	-0.21076	-0.09032
10	-1.15959	-1.10357	-1.02585	-0.92072	-0.76723	-0.59216	-0.41553	-0.22882	-0.11162
11	-1.16832	-1.11228	-1.03462	-0.92970	-0.77663	-0.60247	-0.42721	-0.24281	-0.12693
12	-1.17602	-1.11996	-1.04233	-0.93755	-0.78474	-0.61115	-0.43679	-0.25372	-0.13880
13	-1.18258	-1.12651	-1.04890	-0.94421	-0.79156	-0.61835	-0.44457	-0.26237	0.14809
14	-1.18800	-1.13194	-1.05436	-0.94974	-0.79718	-0.62422	-0.45083	-0.26921	-0.15537
15	-1.19237	-1.13634	-1.05878	-0.95421	-0.80172	-0.62892	-0.45579	-0.27456	-0.16105
16	-1.19581	-1.13981	-1.06229	-0.95777	-0.80532	-0.63263	-0.45968	-0.27871	-0.16544
17	-1.19846	-1.14250	-1.06501	-0.96054	-0.80813	-0.63551	-0.46268	-0.28187	-0.16878
18	-1.20046	-1.14454	-1.06709	-0.96266	-0.81028	-0.63770	-0.46495	-0.28426	-0.17129

Table 0.2. Last 9 columns of matrix $\boldsymbol{C}^{11}$ obtained using the FEM (ANSYS).

	10	**11**	**12**	**13**	**14**	**15**	**16**	**17**	**18**
1	0.00000	0.00000	0.00000	0.00000	0.00000	0.00000	0.00000	0.00000	0.00000
2	0.00000	0.00000	0.00000	0.00000	0.00000	0.00000	0.00000	0.00000	0.00000
3	0.00000	0.00000	0.00000	0.00000	0.00000	0.00000	0.00000	0.00000	0.00000
4	0.00000	0.00000	0.00000	0.00000	0.00000	0.00000	0.00000	0.00000	0.00000
5	0.00000	0.00000	0.00000	0.00000	0.00000	0.00000	0.00000	0.00000	0.00000
6	0.00000	0.00000	0.00000	0.00000	0.00000	0.00000	0.00000	0.00000	0.00000
7	0.00000	0.00000	0.00000	0.00000	0.00000	0.00000	0.00000	0.00000	0.00000
8	0.00000	0.00000	0.00000	0.00000	0.00000	0.00000	0.00000	0.00000	0.00000
9	0.00000	0.00000	0.00000	0.00000	0.00000	0.00000	0.00000	0.00000	0.00000
10	-0.08783	0.00000	0.00000	0.00000	0.00000	0.00000	0.00000	0.00000	0.00000
11	-0.10526	-0.08313	0.00000	0.00000	0.00000	0.00000	0.00000	0.00000	0.00000
12	-0.11745	-0.09818	-0.07727	0.00000	0.00000	0.00000	0.00000	0.00000	0.00000
13	-0.12690	-0.10830	-0.09041	-0.07070	0.00000	0.00000	0.00000	0.00000	0.00000
14	-0.13427	-0.11599	-0.09892	-0.08216	-0.06374	0.00000	0.00000	0.00000	0.00000
15	-0.14003	-0.12192	-0.10525	-0.08934	-0.07368	-0.05656	0.00000	0.00000	0.00000
16	-0.14449	-0.12649	-0.11004	-0.09456	-0.07972	-0.06512	-0.04929	0.00000	0.00000
17	-0.14791	-0.13000	-0.11369	-0.09844	-0.08403	-0.07019	-0.05660	-0.04201	0.00000
18	-0.15050	-0.13266	-0.11644	-0.10135	-0.08716	-0.07372	-0.06081	-0.04818	-0.03476

Table 0.3. First 9 columns of matrix $\boldsymbol{C}^{12}$ obtained using the FEM (ANSYS).

	1	2	3	4	5	6	7	8	9
1	0.09023	0.00000	0.00000	0.00000	0.00000	0.00000	0.00000	0.00000	0.00000
2	0.12177	0.10505	0.00000	0.00000	0.00000	0.00000	0.00000	0.00000	0.00000
3	0.15029	0.14022	0.10908	0.00000	0.00000	0.00000	0.00000	0.00000	0.00000
4	0.17868	0.17013	0.14578	0.09979	0.00000	0.00000	0.00000	0.00000	0.00000
5	0.19274	0.18600	0.16397	0.12382	0.07538	0.00000	0.00000	0.00000	0.00000
6	0.20190	0.19640	0.17560	0.13695	0.09237	0.06204	0.00000	0.00000	0.00000
7	0.20724	0.20259	0.18252	0.14455	0.10071	0.07460	0.04629	0.00000	0.00000
8	0.20893	0.20479	0.18509	0.14737	0.10376	0.07839	0.05306	0.02491	0.00000
9	0.20844	0.20439	0.18474	0.14698	0.10324	0.07786	0.05251	0.02450	0.00932
10	0.20776	0.20385	0.18427	0.14650	0.10265	0.07727	0.05196	0.02402	0.00952
11	0.20722	0.20345	0.18395	0.14617	0.10225	0.07690	0.05164	0.02378	0.00964
12	0.20693	0.20329	0.18387	0.14610	0.10214	0.07683	0.05162	0.02385	0.00993
13	0.20694	0.20342	0.18407	0.14631	0.10233	0.07707	0.05192	0.02421	0.01044
14	0.20725	0.20383	0.18454	0.14679	0.10281	0.07759	0.05249	0.02483	0.01118
15	0.20781	0.20447	0.18524	0.14751	0.10353	0.07836	0.05330	0.02567	0.01210
16	0.20857	0.20530	0.18611	0.14840	0.10444	0.07930	0.05428	0.02668	0.01316
17	0.20946	0.20625	0.18709	0.14941	0.10547	0.08037	0.05537	0.02779	0.01431
18	0.21041	0.20725	0.18813	0.15047	0.10656	0.08149	0.05652	0.02894	0.01549

Table 0.4. Last 9 columns of matrix $\boldsymbol{C}^{12}$ obtained using the FEM (ANSYS).

	10	11	12	13	14	15	16	17	18
1	0.00000	0.00000	0.00000	0.00000	0.00000	0.00000	0.00000	0.00000	0.00000
2	0.00000	0.00000	0.00000	0.00000	0.00000	0.00000	0.00000	0.00000	0.00000
3	0.00000	0.00000	0.00000	0.00000	0.00000	0.00000	0.00000	0.00000	0.00000
4	0.00000	0.00000	0.00000	0.00000	0.00000	0.00000	0.00000	0.00000	0.00000
5	0.00000	0.00000	0.00000	0.00000	0.00000	0.00000	0.00000	0.00000	0.00000
6	0.00000	0.00000	0.00000	0.00000	0.00000	0.00000	0.00000	0.00000	0.00000
7	0.00000	0.00000	0.00000	0.00000	0.00000	0.00000	0.00000	0.00000	0.00000
8	0.00000	0.00000	0.00000	0.00000	0.00000	0.00000	0.00000	0.00000	0.00000
9	0.00000	0.00000	0.00000	0.00000	0.00000	0.00000	0.00000	0.00000	0.00000
10	0.00977	0.00000	0.00000	0.00000	0.00000	0.00000	0.00000	0.00000	0.00000
11	0.01051	0.01022	0.00000	0.00000	0.00000	0.00000	0.00000	0.00000	0.00000
12	0.01113	0.01142	0.01074	0.00000	0.00000	0.00000	0.00000	0.00000	0.00000
13	0.01188	0.01243	0.01234	0.01134	0.00000	0.00000	0.00000	0.00000	0.00000
14	0.01277	0.01351	0.01366	0.01328	0.01201	0.00000	0.00000	0.00000	0.00000
15	0.01381	0.01467	0.01498	0.01484	0.01423	0.01274	0.00000	0.00000	0.00000
16	0.01496	0.01591	0.01632	0.01633	0.01597	0.01518	0.01352	0.00000	0.00000
17	0.01618	0.01719	0.01767	0.01778	0.01757	0.01704	0.01613	0.01436	0.00000
18	0.01741	0.01847	0.01901	0.01919	0.01907	0.01870	0.01807	0.01709	0.01527

Table 0.5. First 9 columns of matrix $\boldsymbol{C^{13}}$ obtained using the FEM (ANSYS).

	1	**2**	**3**	**4**	**5**	**6**	**7**	**8**	**9**
1	0.02510	0.00000	0.00000	0.00000	0.00000	0.00000	0.00000	0.00000	0.00000
2	0.03643	0.03162	0.00000	0.00000	0.00000	0.00000	0.00000	0.00000	0.00000
3	0.04716	0.04439	0.03659	0.00000	0.00000	0.00000	0.00000	0.00000	0.00000
4	0.05923	0.05746	0.05346	0.04330	0.00000	0.00000	0.00000	0.00000	0.00000
5	0.06488	0.06331	0.05993	0.05276	0.03286	0.00000	0.00000	0.00000	0.00000
6	0.06872	0.06727	0.06422	0.05792	0.04299	0.02085	0.00000	0.00000	0.00000
7	0.07133	0.06999	0.06712	0.06129	0.04762	0.03014	0.00998	0.00000	0.00000
8	0.07269	0.07139	0.06860	0.06296	0.04976	0.03329	0.01655	-0.00207	0.00000
9	0.07222	0.07094	0.06816	0.06251	0.04931	0.03288	0.01621	-0.00209	-0.01265
10	0.07185	0.07058	0.06780	0.06216	0.04896	0.03256	0.01593	-0.00227	-0.01280
11	0.07152	0.07026	0.06749	0.06185	0.04865	0.03226	0.01566	-0.00248	-0.01301
12	0.07122	0.06998	0.06721	0.06158	0.04837	0.03198	0.01539	-0.00273	-0.01323
13	0.07094	0.06972	0.06696	0.06133	0.04811	0.03172	0.01513	-0.00297	-0.01345
14	0.07068	0.06948	0.06673	0.06110	0.04787	0.03147	0.01489	-0.00322	-0.01368
15	0.07044	0.06925	0.06651	0.06089	0.04765	0.03124	0.01465	-0.00346	-0.01391
16	0.07021	0.06903	0.06630	0.06068	0.04744	0.03102	0.01442	-0.00370	-0.01414
17	0.06998	0.06882	0.06610	0.06049	0.04724	0.03081	0.01419	-0.00394	-0.01438
18	0.06977	0.06862	0.06591	0.06030	0.04705	0.03060	0.01398	-0.00418	-0.01461

Table 0.6. Last 9 columns of matrix $\boldsymbol{C}^{13}$ obtained using the FEM (ANSYS).

	10	**11**	**12**	**13**	**14**	**15**	**16**	**17**	**18**
1	0.00000	0.00000	0.00000	0.00000	0.00000	0.00000	0.00000	0.00000	0.00000
2	0.00000	0.00000	0.00000	0.00000	0.00000	0.00000	0.00000	0.00000	0.00000
3	0.00000	0.00000	0.00000	0.00000	0.00000	0.00000	0.00000	0.00000	0.00000
4	0.00000	0.00000	0.00000	0.00000	0.00000	0.00000	0.00000	0.00000	0.00000
5	0.00000	0.00000	0.00000	0.00000	0.00000	0.00000	0.00000	0.00000	0.00000
6	0.00000	0.00000	0.00000	0.00000	0.00000	0.00000	0.00000	0.00000	0.00000
7	0.00000	0.00000	0.00000	0.00000	0.00000	0.00000	0.00000	0.00000	0.00000
8	0.00000	0.00000	0.00000	0.00000	0.00000	0.00000	0.00000	0.00000	0.00000
9	0.00000	0.00000	0.00000	0.00000	0.00000	0.00000	0.00000	0.00000	0.00000
10	-0.01254	0.00000	0.00000	0.00000	0.00000	0.00000	0.00000	0.00000	0.00000
11	-0.01273	-0.01231	0.00000	0.00000	0.00000	0.00000	0.00000	0.00000	0.00000
12	-0.01296	-0.01247	-0.01204	0.00000	0.00000	0.00000	0.00000	0.00000	0.00000
13	-0.01318	-0.01269	-0.01216	-0.01176	0.00000	0.00000	0.00000	0.00000	0.00000
14	-0.01341	-0.01292	-0.01237	-0.01184	-0.01145	0.00000	0.00000	0.00000	0.00000
15	-0.01363	-0.01314	-0.01259	-0.01204	-0.01152	-0.01114	0.00000	0.00000	0.00000
16	-0.01385	-0.01336	-0.01281	-0.01226	-0.01171	-0.01119	-0.01082	0.00000	0.00000
17	-0.01407	-0.01358	-0.01303	-0.01248	-0.01192	-0.01138	-0.01086	-0.01047	0.00000
18	-0.01430	-0.01380	-0.01326	-0.01270	-0.01215	-0.01160	-0.01106	-0.01052	0.01011

Table 0.7. First 9 columns of matrix $\boldsymbol{C}^{21}$ obtained using the FEM (ANSYS).

	1	**2**	**3**	**4**	**5**	**6**	**7**	**8**	**9**
1	0.04082	0.00000	0.00000	0.00000	0.00000	0.00000	0.00000	0.00000	0.00000
2	0.05270	0.04914	0.00000	0.00000	0.00000	0.00000	0.00000	0.00000	0.00000
3	0.06243	0.06212	0.05552	0.00000	0.00000	0.00000	0.00000	0.00000	0.00000
4	0.07112	0.07259	0.07004	0.06273	0.00000	0.00000	0.00000	0.00000	0.00000
5	0.07924	0.08185	0.08086	0.07795	0.06741	0.00000	0.00000	0.00000	0.00000
6	0.08571	0.08934	0.08954	0.08868	0.08528	0.06320	0.00000	0.00000	0.00000
7	0.09009	0.09449	0.09549	0.09588	0.09523	0.07872	0.04976	0.00000	0.00000
8	0.09182	0.09664	0.09805	0.09896	0.09929	0.08386	0.05799	0.02474	0.00000
9	0.09054	0.09551	0.09707	0.09814	0.09870	0.08330	0.05723	0.02335	0.00584
10	0.08914	0.09433	0.09607	0.09734	0.09817	0.08281	0.05659	0.02231	0.00495
11	0.08800	0.09339	0.09532	0.09678	0.09787	0.08258	0.05628	0.02174	0.00438
12	0.08725	0.09283	0.09492	0.09656	0.09788	0.08267	0.05633	0.02160	0.00423
13	0.08695	0.09268	0.09492	0.09671	0.09822	0.08308	0.05672	0.02187	0.00450
14	0.08708	0.09294	0.09529	0.09721	0.09887	0.08380	0.05743	0.02250	0.00513
15	0.08760	0.09356	0.09600	0.09801	0.09980	0.08477	0.05840	0.02342	0.00608
16	0.08843	0.09447	0.09697	0.09906	0.10093	0.08594	0.05957	0.02456	0.00725
17	0.08948	0.09557	0.09813	0.10027	0.10220	0.08724	0.06088	0.02586	0.00858
18	0.09066	0.09680	0.09939	0.10157	0.10354	0.08859	0.06224	0.02722	0.00998

Table 0.8. Last 9 columns of matrix $\boldsymbol{C}^{21}$ obtained using the FEM (ANSYS).

	10	**11**	**12**	**13**	**14**	**15**	**16**	**17**	**18**
1	0.00000	0.00000	0.00000	0.00000	0.00000	0.00000	0.00000	0.00000	0.00000
2	0.00000	0.00000	0.00000	0.00000	0.00000	0.00000	0.00000	0.00000	0.00000
3	0.00000	0.00000	0.00000	0.00000	0.00000	0.00000	0.00000	0.00000	0.00000
4	0.00000	0.00000	0.00000	0.00000	0.00000	0.00000	0.00000	0.00000	0.00000
5	0.00000	0.00000	0.00000	0.00000	0.00000	0.00000	0.00000	0.00000	0.00000
6	0.00000	0.00000	0.00000	0.00000	0.00000	0.00000	0.00000	0.00000	0.00000
7	0.00000	0.00000	0.00000	0.00000	0.00000	0.00000	0.00000	0.00000	0.00000
8	0.00000	0.00000	0.00000	0.00000	0.00000	0.00000	0.00000	0.00000	0.00000
9	0.00000	0.00000	0.00000	0.00000	0.00000	0.00000	0.00000	0.00000	0.00000
10	0.00697	0.00000	0.00000	0.00000	0.00000	0.00000	0.00000	0.00000	0.00000
11	0.00702	0.00806	0.00000	0.00000	0.00000	0.00000	0.00000	0.00000	0.00000
12	0.00724	0.00885	0.00919	0.00000	0.00000	0.00000	0.00000	0.00000	0.00000
13	0.00776	0.00968	0.01063	0.01040	0.00000	0.00000	0.00000	0.00000	0.00000
14	0.00859	0.01071	0.01193	0.01237	0.01166	0.00000	0.00000	0.00000	0.00000
15	0.00967	0.01193	0.01334	0.01405	0.01408	0.01297	0.00000	0.00000	0.00000
16	0.01095	0.01332	0.01484	0.01573	0.01604	0.01574	0.01431	0.00000	0.00000
17	0.01236	0.01480	0.01641	0.01741	0.01790	0.01791	0.01737	0.01571	0.00000
18	0.01383	0.01633	0.01801	0.01909	0.01969	0.01989	0.01968	0.01899	0.01718

Table 0.9. First 9 columns of matrix $\boldsymbol{C}^{22}$ obtained using the FEM (ANSYS).

	1	**2**	**3**	**4**	**5**	**6**	**7**	**8**	**9**
1	-0.40875	0.00000	0.00000	0.00000	0.00000	0.00000	0.00000	0.00000	0.00000
2	-0.48169	-0.42187	0.00000	0.00000	0.00000	0.00000	0.00000	0.00000	0.00000
3	-0.53541	-0.49072	-0.40824	0.00000	0.00000	0.00000	0.00000	0.00000	0.00000
4	-0.57526	-0.53237	-0.46906	-0.36693	0.00000	0.00000	0.00000	0.00000	0.00000
5	-0.63295	-0.59321	-0.53831	-0.46656	-0.36673	0.00000	0.00000	0.00000	0.00000
6	-0.68349	-0.64522	-0.59418	-0.53028	-0.45667	-0.33296	0.00000	0.00000	0.00000
7	-0.71968	-0.68227	-0.63305	-0.57328	-0.50696	-0.41027	-0.26668	0.00000	0.00000
8	-0.73848	-0.70140	-0.65285	-0.59456	-0.53118	-0.43982	-0.31934	-0.17211	0.00000
9	-0.75003	-0.71300	-0.66463	-0.60681	-0.54426	-0.45413	-0.33615	-0.19830	-0.11134
10	-0.76268	-0.72567	-0.67743	-0.61999	-0.55820	-0.46903	-0.35289	-0.21926	-0.13628
11	-0.77437	-0.73739	-0.68923	-0.63210	-0.57091	-0.48242	-0.36747	-0.23611	-0.15446
12	-0.78458	-0.74763	-0.69955	-0.64266	-0.58195	-0.49394	-0.37976	-0.24963	-0.16876
13	-0.79318	-0.75628	-0.70828	-0.65159	-0.59125	-0.50359	-0.38992	-0.26052	-0.18008
14	-0.80022	-0.76339	-0.71546	-0.65894	-0.59889	-0.51150	-0.39817	-0.26922	-0.18905
15	-0.80584	-0.76908	-0.72124	-0.66485	-0.60504	-0.51785	-0.40476	-0.27609	-0.19609
16	-0.81020	-0.77353	-0.72577	-0.66950	-0.60989	-0.52285	-0.40992	-0.28143	-0.20156
17	-0.81351	-0.77693	-0.72924	-0.67308	-0.61361	-0.52670	-0.41389	-0.28552	-0.20574
18	-0.81597	-0.77946	-0.73185	-0.67578	-0.61643	-0.52962	-0.41690	-0.28860	-0.20890

Table 0.10. Last 9 columns of matrix $\boldsymbol{C}^{22}$ obtained using the FEM (ANSYS).

	10	**11**	**12**	**13**	**14**	**15**	**16**	**17**	**18**
1	0.00000	0.00000	0.00000	0.00000	0.00000	0.00000	0.00000	0.00000	0.00000
2	0.00000	0.00000	0.00000	0.00000	0.00000	0.00000	0.00000	0.00000	0.00000
3	0.00000	0.00000	0.00000	0.00000	0.00000	0.00000	0.00000	0.00000	0.00000
4	0.00000	0.00000	0.00000	0.00000	0.00000	0.00000	0.00000	0.00000	0.00000
5	0.00000	0.00000	0.00000	0.00000	0.00000	0.00000	0.00000	0.00000	0.00000
6	0.00000	0.00000	0.00000	0.00000	0.00000	0.00000	0.00000	0.00000	0.00000
7	0.00000	0.00000	0.00000	0.00000	0.00000	0.00000	0.00000	0.00000	0.00000
8	0.00000	0.00000	0.00000	0.00000	0.00000	0.00000	0.00000	0.00000	0.00000
9	0.00000	0.00000	0.00000	0.00000	0.00000	0.00000	0.00000	0.00000	0.00000
10	-0.10887	0.00000	0.00000	0.00000	0.00000	0.00000	0.00000	0.00000	0.00000
11	-0.12978	-0.10361	0.00000	0.00000	0.00000	0.00000	0.00000	0.00000	0.00000
12	-0.14457	-0.12193	-0.09680	0.00000	0.00000	0.00000	0.00000	0.00000	0.00000
13	-0.15613	-0.13435	-0.11293	-0.08898	0.00000	0.00000	0.00000	0.00000	0.00000
14	-0.16521	-0.14386	-0.12347	-0.10314	-0.08052	0.00000	0.00000	0.00000	0.00000
15	-0.17236	-0.15121	-0.13134	-0.11208	-0.09288	-0.07168	0.00000	0.00000	0.00000
16	-0.17792	-0.15692	-0.13732	-0.11860	-0.10044	-0.08237	-0.06263	0.00000	0.00000
17	-0.18219	-0.16131	-0.14188	-0.12347	-0.10583	-0.08872	-0.07179	-0.05349	0.00000
18	-0.18543	-0.16464	-0.14534	-0.12711	-0.10977	-0.09315	-0.07706	-0.06122	-0.04431

Table 0.11. First 9 columns of matrix $\boldsymbol{C}^{23}$ obtained using the FEM (ANSYS).

	1	2	3	4	5	6	7	8	9
1	-0.00009	0.00000	0.00000	0.00000	0.00000	0.00000	0.00000	0.00000	0.00000
2	-0.00306	-0.00105	0.00000	0.00000	0.00000	0.00000	0.00000	0.00000	0.00000
3	-0.00552	-0.00419	-0.00085	0.00000	0.00000	0.00000	0.00000	0.00000	0.00000
4	-0.00729	-0.00600	-0.00350	0.00095	0.00000	0.00000	0.00000	0.00000	0.00000
5	-0.01141	-0.01037	-0.00845	-0.00587	-0.00263	0.00000	0.00000	0.00000	0.00000
6	-0.01543	-0.01456	-0.01294	-0.01095	-0.00924	-0.00365	0.00000	0.00000	0.00000
7	-0.01844	-0.01768	-0.01624	-0.01460	-0.01343	-0.00950	-0.00148	0.00000	0.00000
8	-0.02000	-0.01930	-0.01795	-0.01645	-0.01552	-0.01194	-0.00548	0.00351	0.00000
9	-0.01987	-0.01919	-0.01785	-0.01638	-0.01546	-0.01186	-0.00539	0.00335	0.00838
10	-0.01982	-0.01916	-0.01784	-0.01639	-0.01551	-0.01189	-0.00542	0.00324	0.00821
11	-0.01977	-0.01914	-0.01783	-0.01641	-0.01556	-0.01194	-0.00546	0.00318	0.00817
12	-0.01971	-0.01909	-0.01780	-0.01641	-0.01559	-0.01196	-0.00547	0.00318	0.00817
13	-0.01962	-0.01903	-0.01775	-0.01638	-0.01559	-0.01195	-0.00545	0.00322	0.00822
14	-0.01951	-0.01894	-0.01768	-0.01633	-0.01556	-0.01191	-0.00540	0.00329	0.00831
15	-0.01939	-0.01883	-0.01758	-0.01625	-0.01549	-0.01185	-0.00532	0.00340	0.00842
16	-0.01924	-0.01870	-0.01747	-0.01615	-0.01541	-0.01175	-0.00521	0.00353	0.00856
17	-0.01909	-0.01856	-0.01734	-0.01603	-0.01529	-0.01163	-0.00507	0.00369	0.00873
18	-0.01893	-0.01841	-0.01719	-0.01589	-0.01516	-0.01149	-0.00492	0.00387	0.00891

Table 0.12. Last 9 columns of matrix $\boldsymbol{C}^{23}$ obtained using the FEM (ANSYS).

	10	**11**	**12**	**13**	**14**	**15**	**16**	**17**	**18**
1	0.00000	0.00000	0.00000	0.00000	0.00000	0.00000	0.00000	0.00000	0.00000
2	0.00000	0.00000	0.00000	0.00000	0.00000	0.00000	0.00000	0.00000	0.00000
3	0.00000	0.00000	0.00000	0.00000	0.00000	0.00000	0.00000	0.00000	0.00000
4	0.00000	0.00000	0.00000	0.00000	0.00000	0.00000	0.00000	0.00000	0.00000
5	0.00000	0.00000	0.00000	0.00000	0.00000	0.00000	0.00000	0.00000	0.00000
6	0.00000	0.00000	0.00000	0.00000	0.00000	0.00000	0.00000	0.00000	0.00000
7	0.00000	0.00000	0.00000	0.00000	0.00000	0.00000	0.00000	0.00000	0.00000
8	0.00000	0.00000	0.00000	0.00000	0.00000	0.00000	0.00000	0.00000	0.00000
9	0.00000	0.00000	0.00000	0.00000	0.00000	0.00000	0.00000	0.00000	0.00000
10	0.00840	0.00000	0.00000	0.00000	0.00000	0.00000	0.00000	0.00000	0.00000
11	0.00828	0.00839	0.00000	0.00000	0.00000	0.00000	0.00000	0.00000	0.00000
12	0.00829	0.00827	0.00838	0.00000	0.00000	0.00000	0.00000	0.00000	0.00000
13	0.00833	0.00830	0.00826	0.00837	0.00000	0.00000	0.00000	0.00000	0.00000
14	0.00840	0.00837	0.00831	0.00826	0.00837	0.00000	0.00000	0.00000	0.00000
15	0.00851	0.00847	0.00840	0.00833	0.00828	0.00837	0.00000	0.00000	0.00000
16	0.00864	0.00860	0.00852	0.00844	0.00836	0.00830	0.00837	0.00000	0.00000
17	0.00879	0.00875	0.00867	0.00858	0.00850	0.00841	0.00832	0.00835	0.00000
18	0.00896	0.00892	0.00884	0.00876	0.00867	0.00857	0.00847	0.00835	0.00832

Table 0.13. First 9 columns of matrix $\boldsymbol{C}^{31}$ obtained using the FEM (ANSYS).

	1	**2**	**3**	**4**	**5**	**6**	**7**	**8**	**9**
1	-0.14417	0.00000	0.00000	0.00000	0.00000	0.00000	0.00000	0.00000	0.00000
2	-0.17776	-0.15615	0.00000	0.00000	0.00000	0.00000	0.00000	0.00000	0.00000
3	-0.20388	-0.18848	-0.16113	0.00000	0.00000	0.00000	0.00000	0.00000	0.00000
4	-0.22733	-0.21334	-0.19527	-0.16455	0.00000	0.00000	0.00000	0.00000	0.00000
5	-0.23983	-0.22597	-0.20947	-0.18675	-0.14685	0.00000	0.00000	0.00000	0.00000
6	-0.24967	-0.23575	-0.22000	-0.19977	-0.17301	-0.12386	0.00000	0.00000	0.00000
7	-0.25705	-0.24307	-0.22769	-0.20880	-0.18577	-0.15064	-0.09592	0.00000	0.00000
8	-0.26146	-0.24738	-0.23212	-0.21379	-0.19231	-0.16046	-0.11739	-0.06096	0.00000
9	-0.26561	-0.25150	-0.23626	-0.21806	-0.19692	-0.16585	-0.12422	-0.07201	-0.03454
10	-0.27042	-0.25624	-0.24097	-0.22286	-0.20196	-0.17152	-0.13094	-0.08075	-0.04480
11	-0.27499	-0.26073	-0.24542	-0.22734	-0.20658	-0.17655	-0.13666	-0.08768	-0.05242
12	-0.27901	-0.26468	-0.24932	-0.23126	-0.21056	-0.18080	-0.14136	-0.09311	-0.05837
13	-0.28235	-0.26796	-0.25257	-0.23450	-0.21383	-0.18424	-0.14511	-0.09735	-0.06296
14	-0.28499	-0.27056	-0.25514	-0.23706	-0.21640	-0.18692	-0.14799	-0.10057	-0.06642
15	-0.28694	-0.27250	-0.25706	-0.23899	-0.21832	-0.18891	-0.15012	-0.10292	-0.06895
16	-0.28830	-0.27385	-0.25841	-0.24034	-0.21968	-0.19030	-0.15160	-0.10455	-0.07072
17	-0.28915	-0.27471	-0.25927	-0.24121	-0.22055	-0.19120	-0.15256	-0.10560	-0.07186
18	-0.28961	-0.27517	-0.25975	-0.24169	-0.22104	-0.19171	-0.15310	-0.10620	-0.07252

Table 0.14. Last 9 columns of matrix $\boldsymbol{C}^{31}$ obtained using the FEM (ANSYS).

	10	**11**	**12**	**13**	**14**	**15**	**16**	**17**	**18**
1	0.00000	0.00000	0.00000	0.00000	0.00000	0.00000	0.00000	0.00000	0.00000
2	0.00000	0.00000	0.00000	0.00000	0.00000	0.00000	0.00000	0.00000	0.00000
3	0.00000	0.00000	0.00000	0.00000	0.00000	0.00000	0.00000	0.00000	0.00000
4	0.00000	0.00000	0.00000	0.00000	0.00000	0.00000	0.00000	0.00000	0.00000
5	0.00000	0.00000	0.00000	0.00000	0.00000	0.00000	0.00000	0.00000	0.00000
6	0.00000	0.00000	0.00000	0.00000	0.00000	0.00000	0.00000	0.00000	0.00000
7	0.00000	0.00000	0.00000	0.00000	0.00000	0.00000	0.00000	0.00000	0.00000
8	0.00000	0.00000	0.00000	0.00000	0.00000	0.00000	0.00000	0.00000	0.00000
9	0.00000	0.00000	0.00000	0.00000	0.00000	0.00000	0.00000	0.00000	0.00000
10	-0.03421	0.00000	0.00000	0.00000	0.00000	0.00000	0.00000	0.00000	0.00000
11	-0.04266	-0.03248	0.00000	0.00000	0.00000	0.00000	0.00000	0.00000	0.00000
12	-0.04865	-0.03972	-0.02983	0.00000	0.00000	0.00000	0.00000	0.00000	0.00000
13	-0.05323	-0.04455	-0.03603	-0.02653	0.00000	0.00000	0.00000	0.00000	0.00000
14	-0.05669	-0.04809	-0.03991	-0.03177	-0.02279	0.00000	0.00000	0.00000	0.00000
15	-0.05922	-0.05066	-0.04263	-0.03486	-0.02714	-0.01875	0.00000	0.00000	0.00000
16	-0.06099	-0.05246	-0.04450	-0.03690	-0.02954	-0.02228	-0.01451	0.00000	0.00000
17	-0.06215	-0.05364	-0.04573	-0.03822	-0.03102	-0.02408	-0.01729	-0.01016	0.00000
18	-0.06283	-0.05435	-0.04647	-0.03900	-0.03189	-0.02509	-0.01857	-0.01224	-0.00573

Table 0.15. First 9 columns of matrix $\boldsymbol{C}^{32}$ obtained using the FEM (ANSYS).

	1	2	3	4	5	6	7	8	9
1	-0.18544	0.00000	0.00000	0.00000	0.00000	0.00000	0.00000	0.00000	0.00000
2	-0.21976	-0.18528	0.00000	0.00000	0.00000	0.00000	0.00000	0.00000	0.00000
3	-0.24408	-0.21733	-0.17182	0.00000	0.00000	0.00000	0.00000	0.00000	0.00000
4	-0.26010	-0.23462	-0.19977	-0.14464	0.00000	0.00000	0.00000	0.00000	0.00000
5	-0.28129	-0.25652	-0.22461	-0.18232	-0.12822	0.00000	0.00000	0.00000	0.00000
6	-0.29771	-0.27304	-0.24220	-0.20248	-0.15757	-0.11054	0.00000	0.00000	0.00000
7	-0.30883	-0.28411	-0.25362	-0.21504	-0.17232	-0.13371	-0.08964	0.00000	0.00000
8	-0.31493	-0.29009	-0.25966	-0.22143	-0.17953	-0.14252	-0.10536	-0.06523	0.00000
9	-0.32053	-0.29566	-0.26528	-0.22722	-0.18567	-0.14919	-0.11311	-0.07668	-0.05277
10	-0.32665	-0.30171	-0.27132	-0.23340	-0.19215	-0.15605	-0.12075	-0.08604	-0.06351
11	-0.33230	-0.30727	-0.27686	-0.23904	-0.19801	-0.16217	-0.12734	-0.09356	-0.07148
12	-0.33717	-0.31207	-0.28163	-0.24387	-0.20302	-0.16734	-0.13281	-0.09953	-0.07770
13	-0.34119	-0.31603	-0.28556	-0.24786	-0.20713	-0.17156	-0.13721	-0.10423	-0.08254
14	-0.34436	-0.31915	-0.28867	-0.25100	-0.21036	-0.17487	-0.14064	-0.10784	-0.08623
15	-0.34675	-0.32152	-0.29103	-0.25339	-0.21282	-0.17737	-0.14323	-0.11055	-0.08897
16	-0.34848	-0.32322	-0.29273	-0.25511	-0.21459	-0.17918	-0.14509	-0.11249	-0.09095
17	-0.34965	-0.32438	-0.29389	-0.25629	-0.21581	-0.18043	-0.14637	-0.11382	-0.09230
18	-0.35039	-0.32512	-0.29462	-0.25704	-0.21658	-0.18122	-0.14719	-0.11468	-0.09318

Table 0.16. Last 9 columns of matrix $\boldsymbol{C}^{32}$ obtained using the FEM (ANSYS).

	10	11	12	13	14	15	16	17	18
1	0.00000	0.00000	0.00000	0.00000	0.00000	0.00000	0.00000	0.00000	0.00000
2	0.00000	0.00000	0.00000	0.00000	0.00000	0.00000	0.00000	0.00000	0.00000
3	0.00000	0.00000	0.00000	0.00000	0.00000	0.00000	0.00000	0.00000	0.00000
4	0.00000	0.00000	0.00000	0.00000	0.00000	0.00000	0.00000	0.00000	0.00000
5	0.00000	0.00000	0.00000	0.00000	0.00000	0.00000	0.00000	0.00000	0.00000
6	0.00000	0.00000	0.00000	0.00000	0.00000	0.00000	0.00000	0.00000	0.00000
7	0.00000	0.00000	0.00000	0.00000	0.00000	0.00000	0.00000	0.00000	0.00000
8	0.00000	0.00000	0.00000	0.00000	0.00000	0.00000	0.00000	0.00000	0.00000
9	0.00000	0.00000	0.00000	0.00000	0.00000	0.00000	0.00000	0.00000	0.00000
10	-0.05169	0.00000	0.00000	0.00000	0.00000	0.00000	0.00000	0.00000	0.00000
11	-0.06053	-0.04915	0.00000	0.00000	0.00000	0.00000	0.00000	0.00000	0.00000
12	-0.06684	-0.05664	-0.04574	0.00000	0.00000	0.00000	0.00000	0.00000	0.00000
13	-0.07167	-0.06171	-0.05206	-0.04177	0.00000	0.00000	0.00000	0.00000	0.00000
14	-0.07533	-0.06547	-0.05613	-0.04701	-0.03742	0.00000	0.00000	0.00000	0.00000
15	-0.07806	-0.06823	-0.05902	-0.05024	-0.04169	-0.03283	0.00000	0.00000	0.00000
16	-0.08002	-0.07021	-0.06107	-0.05244	-0.04420	-0.03622	-0.02808	0.00000	0.00000
17	-0.08137	-0.07157	-0.06248	-0.05392	-0.04583	-0.03811	-0.03069	-0.02323	0.00000
18	-0.08225	-0.07246	-0.06340	-0.05489	-0.04687	-0.03928	-0.03205	-0.02513	-0.01831

Table 0.17. First 9 columns of matrix $\boldsymbol{C}^{33}$ obtained using the FEM (ANSYS).

	1	**2**	**3**	**4**	**5**	**6**	**7**	**8**	**9**
1	-0.57169	0.00000	0.00000	0.00000	0.00000	0.00000	0.00000	0.00000	0.00000
2	-0.67388	-0.59859	0.00000	0.00000	0.00000	0.00000	0.00000	0.00000	0.00000
3	-0.75211	-0.69903	-0.59003	0.00000	0.00000	0.00000	0.00000	0.00000	0.00000
4	-0.81609	-0.76864	-0.68991	-0.55273	0.00000	0.00000	0.00000	0.00000	0.00000
5	-0.86946	-0.82526	-0.75478	-0.65127	-0.49182	0.00000	0.00000	0.00000	0.00000
6	-0.91040	-0.86810	-0.80190	-0.70767	-0.58549	-0.41247	0.00000	0.00000	0.00000
7	-0.93851	-0.89747	-0.83353	-0.74411	-0.63221	-0.49472	-0.31407	0.00000	0.00000
8	-0.95273	-0.91226	-0.84922	-0.76161	-0.65360	-0.52335	-0.37001	-0.19126	0.00000
9	-0.96140	-0.92110	-0.85834	-0.77123	-0.66414	-0.53545	-0.38476	-0.21433	-0.10970
10	-0.97099	-0.93087	-0.86837	-0.78170	-0.67540	-0.54790	-0.39913	-0.23235	-0.13142
11	-0.98009	-0.94014	-0.87785	-0.79153	-0.68582	-0.55919	-0.41165	-0.24694	-0.14744
12	-0.98835	-0.94856	-0.88645	-0.80039	-0.69514	-0.56912	-0.42241	-0.25889	-0.16035
13	-0.99567	-0.95603	-0.89407	-0.80823	-0.70332	-0.57775	-0.43161	-0.26888	-0.17097
14	-1.00206	-0.96257	-0.90074	-0.81506	-0.71043	-0.58519	-0.43946	-0.27726	-0.17980
15	-1.00757	-0.96821	-0.90650	-0.82097	-0.71655	-0.59156	-0.44612	-0.28428	-0.18717
16	-1.01226	-0.97303	-0.91143	-0.82602	-0.72177	-0.59697	-0.45176	-0.29017	-0.19332
17	-1.01623	-0.97711	-0.91561	-0.83030	-0.72619	-0.60155	-0.45649	-0.29510	-0.19845
18	-1.01955	-0.98054	-0.91912	-0.83390	-0.72991	-0.60539	-0.46045	-0.29920	-0.20272

Table 0.18. Last 9 columns of matrix $\boldsymbol{C}^{33}$ obtained using the FEM (ANSYS).

	10	**11**	**12**	**13**	**14**	**15**	**16**	**17**	**18**
1	0.00000	0.00000	0.00000	0.00000	0.00000	0.00000	0.00000	0.00000	0.00000
2	0.00000	0.00000	0.00000	0.00000	0.00000	0.00000	0.00000	0.00000	0.00000
3	0.00000	0.00000	0.00000	0.00000	0.00000	0.00000	0.00000	0.00000	0.00000
4	0.00000	0.00000	0.00000	0.00000	0.00000	0.00000	0.00000	0.00000	0.00000
5	0.00000	0.00000	0.00000	0.00000	0.00000	0.00000	0.00000	0.00000	0.00000
6	0.00000	0.00000	0.00000	0.00000	0.00000	0.00000	0.00000	0.00000	0.00000
7	0.00000	0.00000	0.00000	0.00000	0.00000	0.00000	0.00000	0.00000	0.00000
8	0.00000	0.00000	0.00000	0.00000	0.00000	0.00000	0.00000	0.00000	0.00000
9	0.00000	0.00000	0.00000	0.00000	0.00000	0.00000	0.00000	0.00000	0.00000
10	-0.10898	0.00000	0.00000	0.00000	0.00000	0.00000	0.00000	0.00000	0.00000
11	-0.12794	-0.10543	0.00000	0.00000	0.00000	0.00000	0.00000	0.00000	0.00000
12	-0.14162	-0.12276	-0.10037	0.00000	0.00000	0.00000	0.00000	0.00000	0.00000
13	-0.15267	-0.13488	-0.11635	-0.09437	0.00000	0.00000	0.00000	0.00000	0.00000
14	-0.16178	-0.14455	-0.12720	-0.10908	-0.08778	0.00000	0.00000	0.00000	0.00000
15	-0.16938	-0.15246	-0.13575	-0.11884	-0.10128	-0.08086	0.00000	0.00000	0.00000
16	-0.17572	-0.15903	-0.14268	-0.12642	-0.11007	-0.09320	-0.07377	0.00000	0.00000
17	-0.18101	-0.16450	-0.14839	-0.13251	-0.11680	-0.10108	-0.08499	-0.06664	0.00000
18	-0.18542	-0.16905	-0.15311	-0.13749	-0.12215	-0.10705	-0.09204	-0.07678	-0.05957

ANNEX C - STRAIN FIELD FIGURES

Radial and tangential strain field around the hole for different caseloads ((a), (b) and (c) – see Figure 5.2) are shown in figures below, corresponding to the first and last increment (18th increment) when the hole attained its maximum simulated depth (around 1 mm depth).

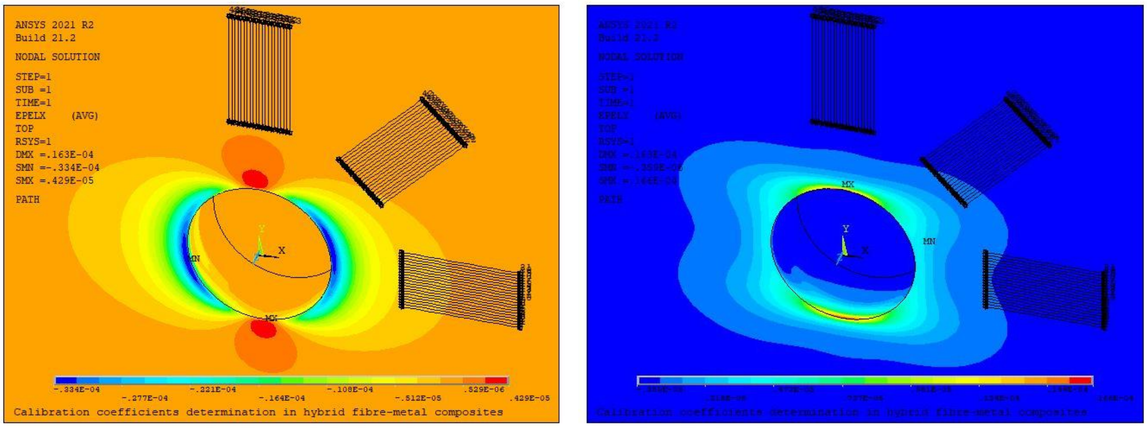

(a) (b)

Figure 0.1. Strain field around the hole (a) radial and (b) tangential, when applying $\boldsymbol{\sigma}_{\mathbf{x}} = \mathbf{1}, \boldsymbol{\sigma}_{\mathbf{y}} = \boldsymbol{\tau}_{xy} = \mathbf{0}$ to the 1st depth increment of the hole with maximum depth (around 1 mm depth).

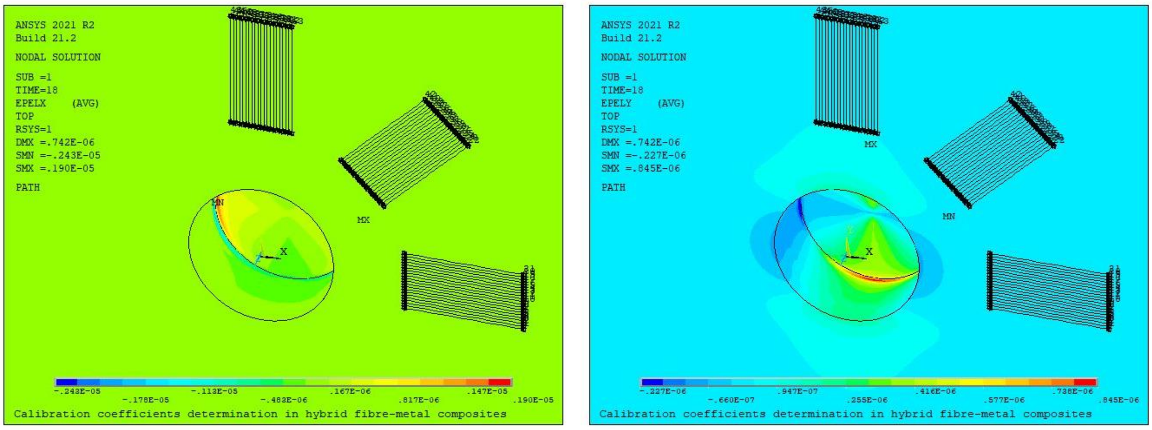

(a) (b)

Figure 0.2. Strain field around the hole (a) radial and (b) tangential, when applying $\boldsymbol{\sigma}_{\mathbf{x}} = \mathbf{1}, \boldsymbol{\sigma}_{\mathbf{y}} = \boldsymbol{\tau}_{xy} = \mathbf{0}$ to the last depth increment (18th) of the hole with maximum depth (around 1 mm depth).

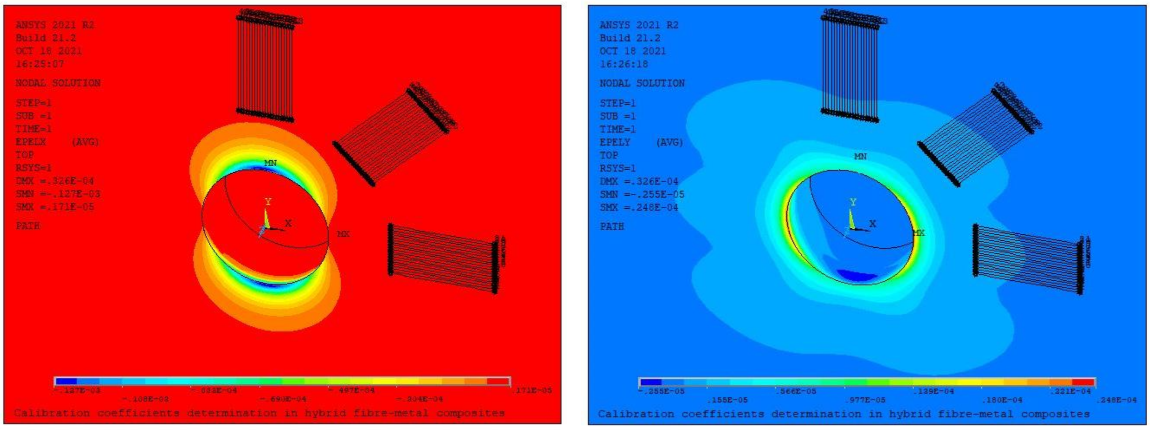

(a)

(b)

Figure 0.3. Strain field around the hole (a) radial and (b) tangential, when applying $\boldsymbol{\sigma_y = 1, \sigma_x = \tau_{xy} = 0}$ to the 1st depth increment of the hole with maximum depth (around 1 mm depth).

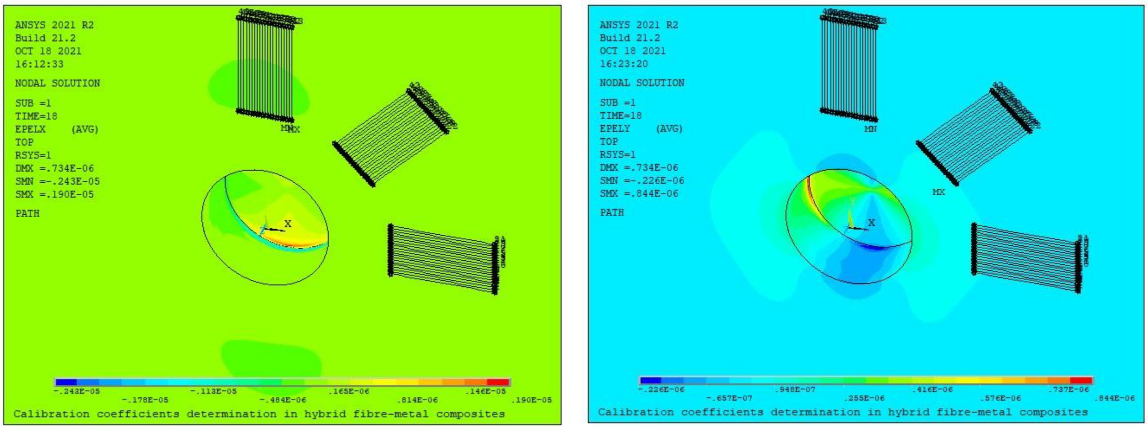

(a)

(b)

Figure 0.4. Strain field around the hole (a) radial and (b) tangential, when applying $\boldsymbol{\sigma_y = 1, \sigma_x = \tau_{xy} = 0}$ to the last depth increment (18th) of the hole with maximum depth (around 1 mm depth).

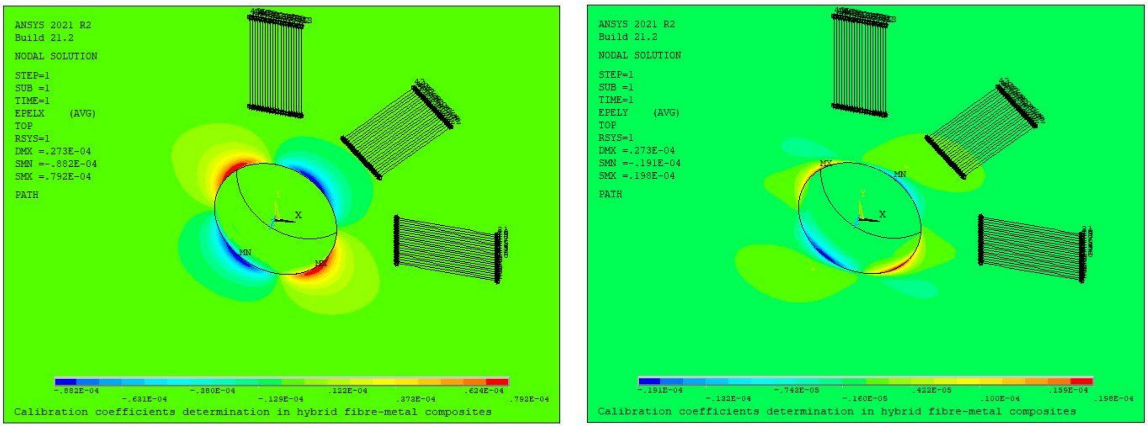

(a) (b)

Figure 0.5. Strain field around the hole (a) radial and (b) tangential, when applying $\boldsymbol{\tau_{xy}} = \mathbf{1}, \boldsymbol{\sigma_x} = \boldsymbol{\sigma_y} = \mathbf{0}$ to the 1st depth increment of the hole with maximum depth (around 1 mm depth).

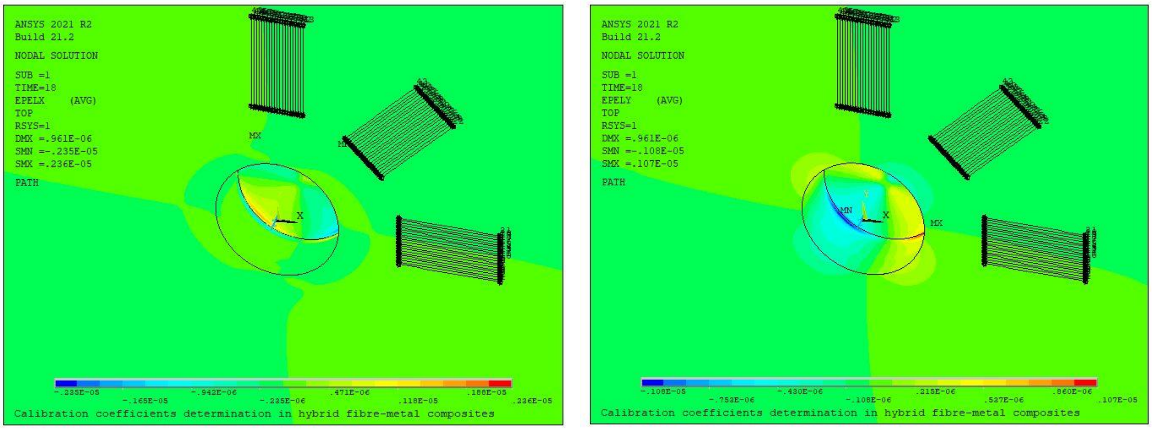

(a) (b)

Figure 0.6. Strain field around the hole (a) radial and (b) tangential, when applying $\boldsymbol{\tau_{xy}} = \mathbf{1}, \boldsymbol{\sigma_x} = \boldsymbol{\sigma_y} = \mathbf{0}$ to the last depth increment (18th) of the hole with maximum depth (around 1 mm depth).